Dupl.

A STUDY OF THE $^{90}Zr(n,d)^{89}Y$ REACTION

by

Ahmed Cassim Bawa

Submitted in partial fulfilment of the requirements for the Degree of Master of Science in the Department of Physics in the Faculty of Science at the University of Durban-Westville.

Supervisor : Professor K Bharuth-Ram

Co-Supervisor : Dr W R McMurray

Date submitted: December 1986

ACKNOWLEDGEMENTS

I would like to thank the following:

my supervisors, Professor K Bharuth-Ram and Dr WR McMurray for their guidance and advice during the period of this research

Dr AA Cowley and Mr J Pilcher of the National Accelerator Centre for assistance with the computer code DWUCK 4

my colleagues in the Physics department for the many hours of discussion

Mrs Muriel Moodley for her support and for typing the thesis in its final form

the University of Durban-Westville and the CSIR for their financial support, without which this study would have been impossible

Finally, I would especially like to thank my wife Rookaya and my parents without whose support none of this would have been possible.

ABSTRACT

A study has been made of the $^{90}Zr(n,d)^{89}Y$ reaction at an incident neutron energy of 22 MeV. The experimental aspect of the study was performed at the Van der Graaf facility at the National Accelerator Centre, using a particle spectrometer developed by K Bharuth-Ram and W R McMurray for the study of neutron-induced charged-particle emissions. The spectrometer, which consists of a telescope of three multiwire proportional counters and a curved plastic scintillator, permits the simultaneous accumulation of data over an angular range of 80°. Solid-angle-calculations have been performed to correct for the effect of the geometry of the system on the angular distribution of the cross-sections. A review has been made of the shell model of the nucleus, the optical potential model and the distorted waves method (or DWBA) for the analysis of direct nuclear reactions. A distorted-waves method analysis of the reaction is performed with the code DWUCK 4 and the resulting angular distribution of the various cross-sections are compared with the experimentally obtained data. This comparison produces spectroscopic factors which are used to perform some analysis of the nuclear structure of the ^{90}Zr nucleus.

CONTENTS

Chapter One

Introduction

This study investigates the $^{90}Zr(n,d)^{89}Y$ reaction which proceeds via a direct pick-up reaction. In this type of reaction there exists a finite probability that an incident nucleon(s) can interact strongly with the nucleons in the surface region of the target nucleus. Such reactions, thus, proceed directly from initial to final nuclear states without the creation of an intermediate compound nuclear system, and have interaction times of the order of the period of an orbit of a nucleon within a nucleus.

The simplicity of these reactions makes them very important as sources of information on nuclear structure. This depends on the fact that these single-step processes produce cross-sections which depend in a relatively simple way on the overlap between the initial and final states of the sample nuclei. This produces information on the similarity between these states. In the case of the (n,d) reaction investigated it is the similarity between the residual ^{89}Y nucleus and the target ^{90}Zr nucleus ($=^{89}Y$ nucleus + one proton in the $2p_{1/2}$ single particle orbit in the shell model of the nucleus). The so-called spectroscopic factor is a measure of this similarity. It is feasible to employ the pick-up reaction as a tool to investigate the validity of the nuclear shell model.

Pick-up reactions (like other direct reactions) have a high degree of selectivity in the choices that they make to final states. The conservation of total angular momentum and the conservation of parity ensure that the final states of the nuclei are clearly identifiable quantum states. This is examined in terms of the reaction under consideration. We assume a shell model picture of ^{90}Zr, and therefore start by making a summary of the Shell Model of the nucleus in Section 1.1.

1.1 Summary of the Shell Model of the Nucleus

Consider a nucleus of A nucleons (Z protons and N=A-Z neutrons), built-up with a single particle potential, U(i) where U(i) is a function of the spatial, spin and isospin coordinates of the i-th particle. In addition, the nucleons experience a two-body residual interaction $\mu(i,j)$ where $\mu(i,j)$ is a function of the spatial, spin and isospin coordinates of both the i-th and j-th nucleons. The $\mu(i,j)$ are weak enough to be employed as the first order perturbations to the U(i) in the evaluation of the energies of the different shell-model levels. The shell-model Hamiltonian may then be written as

$$H_{SM} = H_o + \tfrac{1}{2} \Sigma_{i \neq j} \mu(i,j)$$
$$H_o = \Sigma_i \left(-\hbar^2 / 2u \nabla_i^2 + U(i)\right)$$

Spatial symmetry of H_o gives rise to degeneracy in H_o with respect to the m-states of any single-particle level. In addition, H_o is charge independent and this gives rise to similar neutron and proton states.

The first order perturbation corrections require the diagonalization of the perturbation within the subspace of the degenerate states of H_o. Consider eigenstates $\phi_\alpha(i)$ of H_o, that is

$$H_o \phi_\alpha(i) = \epsilon_\alpha \phi_\alpha(i)$$

where $\alpha = (n_\alpha \ell_\alpha j_\alpha m_\alpha)$. Due to the spherical symmetry of H_o the configuration $(n_\alpha \ell_\alpha j_\alpha)$ has $(2j_\alpha+1)$ - fold degeneracy. Similarly, the two-particle configuration $(n_\alpha \ell_\alpha j_\alpha, n_\beta \ell_\beta j_\beta)$ has zeroth-order energy $\epsilon_\alpha+\epsilon_\beta$ and is $(2j_\alpha+1)(2j_\beta+1)$ - fold degenerate. A suitable choice of eigenfunctions for a two particle-configuration is the m-scheme set [2][3]

$$\phi(m_\alpha, m_\beta) = 1/\sqrt{2} \begin{vmatrix} \phi_\alpha(1) & \phi_\alpha(2) \\ \phi_\beta(1) & \phi_\beta(2) \end{vmatrix}$$

The two-body residual interaction $\mu(i,j)$ commutes with J_z so that

$$(\phi(m_\alpha,m_\beta) \,|\mu(1,2)\, \phi(m'_\alpha, m'_\beta)) = 0 \quad \text{if } m_\alpha + m_\beta \neq m'_\alpha + m'_\beta$$

There are $(2j_\alpha+1)(2j_\beta+1)$ eigenfunctions $\phi(m_\alpha,m_\beta)$. Transforming to the J-scheme the following set of $(2j_\alpha+1)(2j_\beta+1)$ degenerate states of H_o corresponding to the eigenvalue $\epsilon_\alpha+\epsilon_\beta$ are obtained.

$$|j_\alpha j_\beta\, JM\rangle \equiv \sum_{m_\alpha\, m_\beta} (j_\alpha m_\alpha j_\beta m_\beta \,|JM)\, \phi_\alpha(m_\alpha, m_\beta) \qquad (1.1)$$

where $J = |j_\alpha - j_\beta|, |j_\alpha - j_\beta|+1, \ldots, j_\alpha + j_\beta$.

Now $\langle j_\alpha j_\beta JM|\mu(1,2)|j_\alpha j_\beta J'M'\rangle = 0$ if $J \neq J'$ and $M \neq M'$.

Then for a two-particle system j_α, j_β there is only one value for J and M. Therefore the matrix elements of $\mu(1,2)$ with the wavefunctions in (1.1) above are diagonal and give the first-order perturbation energy, that is

$$\Delta E(j_\alpha j_\beta JM) = \langle (j_\alpha j_\beta JM \mid \mu(1,2) \mid j_\alpha j_\beta JM \rangle \qquad (1.2)$$

This expression holds only for simple two-particle systems. Equation (1.2) above is invariant under rotations so that with the Wigner-Eckart theorem the expression for E reduces to

$$\Delta E(j_\alpha j_\beta JM) = (2J+1)^{-\frac{1}{2}} (j_\alpha j_\beta J || \mu(1,2) || j_\alpha j_\beta J)$$

where the reduced matrix element is independent of M. This demonstrates the (2J+1) - fold degeneracy that exists within a state with total angular momentum quantum number J. However, $\mu(1,2)$ does lift some of the degeneracy since it shifts states with different J's differently. This remaining degeneracy is due to the spherical symmetry of H_o.

For the residual interaction $\mu(1,2)$, a δ-potential is often chosen[2], so that

$$\mu(1,2) = -V_o \, \delta(\underline{r}_1 - \underline{r}_2)$$

where V_o has units of (energy x volume). Then

$$\Delta E_\delta(j_\alpha j_\beta J) = V_o \langle j_\alpha j_\beta JM \mid -\delta(\underline{r}_1 - \underline{r}_2) \mid j_\alpha j_\beta JM \rangle$$

$$= V_o \, F_o(n_\alpha \ell_\alpha n_\beta \ell_\beta) \, A(j_\alpha j_\beta JM)$$

where F_o represents the overlap of the radial parts of the wavefunctions of the particles 1 and 2.

Hence it is a function only of r. A is a function of J, so that

$$\Delta E(J) \;/\; \Delta E(J') \;=\; A(j_\alpha j_\beta J) \;/\; A(j_\alpha j_\beta J')$$

The coefficients $A(j_\alpha j_\beta JM)$ have the following form

$$A(j_\alpha j_\beta JM) = \begin{cases} 1/4\pi(2j_\alpha+1)(2j_\beta+1) \begin{pmatrix} j_\alpha & j_\beta & J^2 \\ \tfrac{1}{2} & -\tfrac{1}{2} & 0 \end{pmatrix} & \text{(if } \ell_\alpha+\ell_\beta-J \text{ is even)} \\ 0 & \text{(if } \ell_\alpha+\ell_\beta-J \text{ is odd).} \end{cases}$$

------ (1.3)

It can be seen from equation (1.3) that if the configuration $(j_\alpha j_\beta)$ has even parity (that is, $\ell_\alpha+\ell_\beta$ is even) then only states with even J are affected by the δ-potential. While for odd parity, only odd J states are affected by the δ-potential. What this indicates is that the even or odd J-value together with the parity combine to determine whether the probability of finding two particles close together in energy vanishes or not.

Up to this point only two-particle configurations have been considered. Consider a nucleus with level j filled with $n=(2j+1)$ nucleons and level j' with $1<n<2j'+1$ nucleons. The j-level is fully defined with definite quantum numbers; the total angular momentum being zero and its parity positive. If it is assumed that the $j'^{n'}$ configuration is defined by the set of quantum numbers $(\alpha J^\pi M)$ then the $j^{2j+1}\ j'^{n'}$ configuration has the same set of quantum numbers $(\alpha J^\pi M)$ since the j^{2j+1} configuration has $J^\pi=0^+$ and $M=0$.

The required condition of antisymmetrization does not alter this result. In addition to the above, the energy spacings between the levels in the $j^{2j+1}j'^{n}$ configuration are identical to those in the j'^{n} configuration.

The introduction of the isospin formalism ensures the treatment of a neutron-proton system as if these particles are different states of the nucleon. This involves writing equation (1) as

$$|j_\alpha j_\beta JMTM_T> = \sum_{m_\alpha m_\beta m_{t\alpha} m_{t\beta}} (j_\alpha m_\alpha j_\beta m_\beta | JM)\ (\tfrac{1}{2}\ m_{t\alpha}\ \tfrac{1}{2}\ m_{t\beta}\ |\ T\ M_T)$$

$$\times \phi(m_\alpha m_{t\alpha},\ m_\beta m_{t\beta})$$

where $m_{t\alpha}$, $m_{t\beta}$ = ½ (for proton) and -½ (for neutron). Now, as nuclei increase in A-number the symmetry between protons and neutrons begins to break down. A neutron excess builds-up so that protons and neutrons fill different major shells.

Nuclear properties undergo sharp changes at certain values of N and Z. This has been known experimentally for many years. These numbers are called "magic numbers" and their values become most apparent in the discontinuity of the average binding energy per nucleon that occurs for most nuclei at those N and Z values. A sudden decrease in the binding energies of protons and neutrons is observed at N and Z = 8, 20, 28, 50, 82 and 126. McCarthy[5], quoting Elsasser[6], also lists 6 and 14 as less-pronounced magic numbers. In addition, McCarthy shows how values for these magic numbers may be obtained theoretically, using an infinite square-well potential for the interaction between a nucleon and the nucleus to which it is bound. He performs the calculation for the harmonic oscillator potential as well, although results for both these potential proved unsatisfactory.

in that they did not match experimentally observed values. The infinite square-well potential, for instance, produced the following magic numbers: 2, 8, 20, 34, 40, 58, 92, 132 and 138. The inclusion of a spin-orbit potential to the interaction then produced the correct sequence of magic numbers. Figure (1.1), reproduced from Aŕya[7], shows both the level scheme and magic numbers produced by the square-well and harmonic oscillator potentials, as well as that produced by an average of the square-well and harmonic oscillator potentials with spin-orbit potential.

^{90}Zr is a member of the highest group of nuclides that may be described by valence protons and neutrons that fill different shell-model orbitals[1]. The outermost neutrons occupy the $1\,g_{9/2}$ level while the outermost protons fill the $2\,p_{1/2}$ level. For reasons of expediency we treat the neutron and proton as distinguishable particles.

The outermost nucleons in the ^{90}Zr nucleus are ten neutrons that occupy and fill the $1\,g_{9/2}$ neutron subshell and two protons, that lie outside the semi-closed $2\,p_{3/2}$ proton subshell, shared between the $2\,p_{1/2}$ and the $1\,g_{9/2}$ levels. Thus, this nucleus is characterized by two valence protons outside the closed inert core of ^{88}Sr (see figure (1.2)). The protons can occupy the following configurations : $(2\,p_{1/2})_2$,$(1\,g_{9/2})_2$, and $(2\,p_{1/2},\ 1\,g_{9/2})$. The $2\,p_{1/2}$ configuration can only produce $J^\pi=0^+$ since $\ell_\alpha+\ell_\beta=2$ and so J must be even. In the $(1\,g_{9/2})_2$ configuration $\ell_\alpha+\ell_\beta=8$ and so J must be even. This gives rise to the following J^π values : 0^+, 2^+, 4^+, 6^+ and 8^+. Finally, the $(2\,p_{1/2},\ 1\,g_{9/2})$ configuration has $\ell_\alpha+\ell_\beta=5$ so that $J^\pi = 4^-$ and 5^-. Figure 1.3 demonstrates these calculated levels[4] and the experimentally observed levels together with their respective

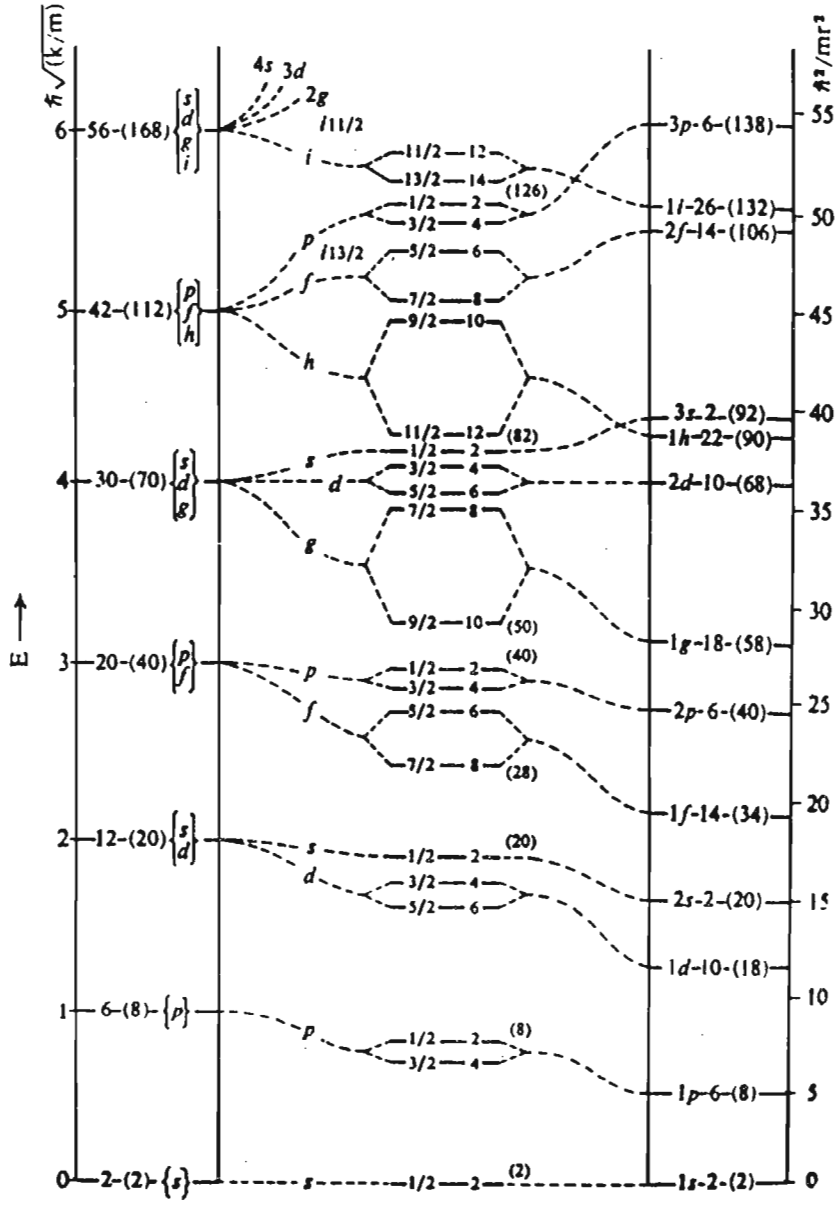

Fig. 1.1 The sequence of energy levels of a nucleon according to the shell model.

energies.

The proton pick-up reaction on ^{90}Zr provides an efficient mechanism for determining the proton-occupancy of the $2p_{1/2}$ level and the $1g_{9/2}$ level, on condition that the energy resolution of the emerging particles and the angular resolution of the cross-sections are sufficiently high to allow the comparison of the experimental results with distorted waves method calculations. In addition, such an experiment allows an examination of the ground and excited states of the residual nucleus, ^{89}Y.

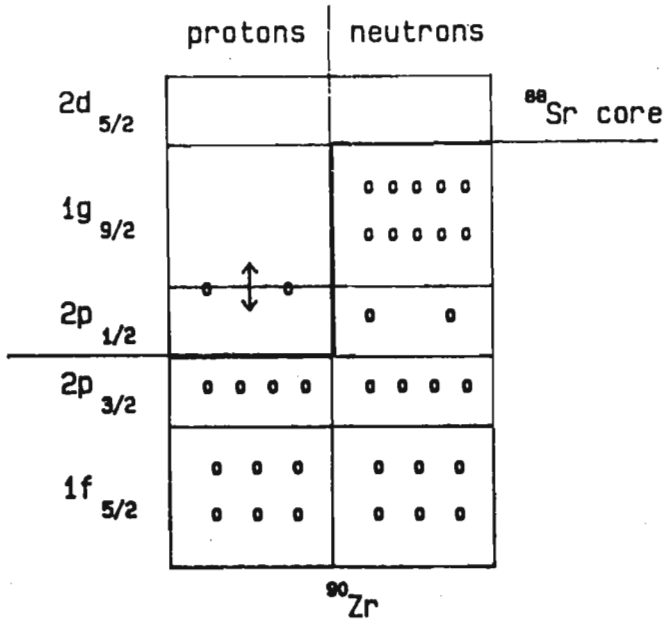

Fig. 1.2 Nucleon occupancy of shell model orbitals in ^{90}Zr.

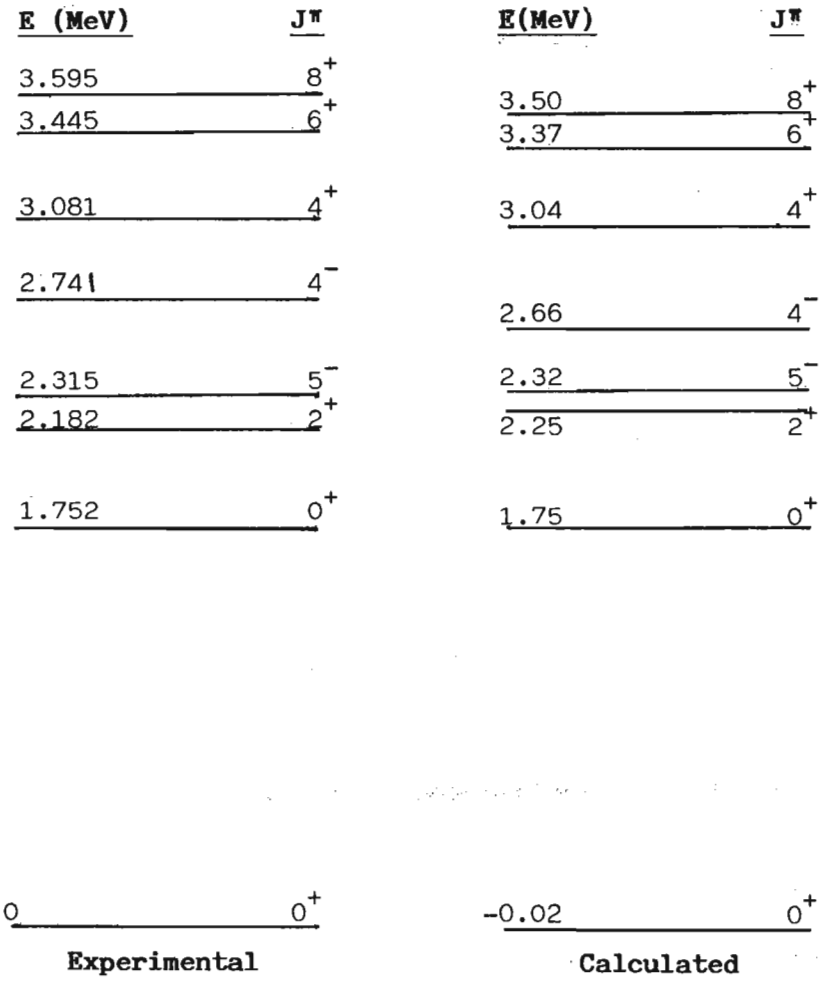

Fig. 1.3 Experimental and Calculated Energy levels of ^{90}Zr. (from Ref.4)

REFERENCES:

(1) D. H. Gloeckner, Nucl. Phys. A253 (1975) 301.

(2) A. de Shalit and H.Feshbach, Theoretical Nuclear Physics. Volume 1: Nuclear Structure, (John Wiley and Sons, Inc., 1974).

(3) P. E. Nemirovskii, Nuclear Models, (E. and F. N. Spon Limited, 1960).

(4) N. Auerbach and I. Talmi, Nucl. Phys. 64 (1965) 458.

(5) I. E. McCarthy, Introduction to Nuclear Theory, (Wiley New York, 1968).

(6) W. M. Elsasser, J. Phys. et Radium 5 (1934) 389,685.

(7) A. P. Arya, Fundamentals of Nuclear Physics, (Allyn and Bacon, Inc., 1966).

Chapter Two

The distorted-waves method

2.1 The optical model

The introduction and utilization of the optical model in the understanding of nuclear reactions became necessary when it was realized that direct reactions were not purely surface phenomena - that although the formation of a compound system did not occur some absorption did take place within the target. The optical model has since become an intrinsic element in the description of direct nuclear reactions. Its importance to the distorted-waves method is two-fold. Firstly, it produces an interpretation of the phenomenon of elastic scattering - of which the transfer reaction is treated as a first-order perturbation. Secondly, its use leads to the necessary wave-functions for the relative motion of the nuclei involved in the reaction collision. These "distorted waves" are essential ingredients in the distorted-waves method.

The effective interaction between two colliding nuclei is very complicated. According to Satchler[1] it is complex, nonlocal (or momentum-dependent), energy-dependent, has quasi-bound states which give rise to resonances and finally, it is dependent on the model space that is chosen. The optical model is a model of this interaction and it reduces the complexity of the interaction by restricting the model to that of a two-particle interaction, using a potential.

This is possible within a model space that involves just one or a few open channels. The optical model potential parameters are related to fundamental quantities such as the nucleon-nucleon interaction and other quantities related to nuclear structure. However, ambiguities do remain and there is no guarantee that optical models are not just a parametrization of experimental data points[1].

In a fashion that is analogous to the nuclear shell model, it is assumed that two nuclei interact with each other as if all the nucleons of one nucleus interact in an average manner with the nucleons of the other nucleus. The optical model potential necessary for this is a function of the distance between the nuclei in some channel α, say. This potential $U = U(r_\alpha)$ is selected on the basis that it provides the best possible description of elastic scattering in the α channel. The direct reactions are then considered to be perturbations on elastic scattering (which is feasible since elastic scattering cross-sections are much larger than inelastic or transfer reaction cross-sections).

2.1.1 Properties of the optical model potential

In the case of a transfer reaction the model space has at least a few inelastic channels. The potentials that link these channels and the elastic channel must be complex (since, even if the bombarding energy is below the threshold for the opening of inelastic channels flux absorption into compound-elastic scattering does occur). Glendenning[2] has shown analytically that if flux absorption does occur then the optical model potential must be complex.

The imaginary part of the potential must be chosen so as to ensure that the flux absorbed is not greater than the flux that is incident.

The effective interaction is explicitly dependent on the bombarding energy, E. The optical model potential must mimic this and this is indeed the case. The potential parameters that give a good fit for elastic scattering data at some bombarding energy will not necessarily produce good fits for the same colliding nuclei at a different bombarding energy.

The effective interaction B is a nonlocal operator, that is

$$B\ \phi(\underline{r}) = \int B(\underline{r},\underline{r}')\ \ \phi(r')\ \ dr'.$$

The effective interaction permits an incident nucleon to escape from the elastic channel at $\underline{r}$, to traverse part of the nucleus in an inelastic channel and then to reenter the elastic channel at $\underline{r}'$. Another source of nonlocality is due to antisymmetrization between the projectile and the target nucleons. This nonlocal interaction can be modelled by a local but energy-dependent potential. Several approximations have been used in distorted-wave method computer codes to minimize this discrepancy, an example being the local energy approximation (LEA)[1][3].

For a local potential the Schrodinger equation may be written as

$$(H_\alpha + T_\alpha + U_\alpha - E)\ \phi(\underline{r}) = 0$$

where H_α operates on the internal coordinates of the particles in the α channel, T_α is the kinetic energy of the relative

motion of the particles in the α channel. However, for a nonlocal potential the Schrodinger equation must be written as

$$(H_\alpha + T_\alpha - E)\,\phi(\underline{r}) + U(\underline{r},\underline{r}')\,\phi(\underline{r}')\,d\underline{r}' = 0$$

If the nonlocality range is small, that is $(\underline{r}-\underline{r}')$is small, $\phi(\underline{r}')$ may be expanded as a Taylor series about $\underline{r}$, that is

$$\phi(\underline{r}') = \phi(\underline{r}) + (\underline{r}'-\underline{r}).\,\nabla\phi(\underline{r}) + 1/2\,(\underline{r}'-\underline{r})^2.\,\nabla^2.\,\phi(r) + \ldots$$

where $\nabla = \underline{p}/i\hbar$ and the ∇^2 term is an energy term. The integral in equation (1) above therefore demonstrates the energy-dependence of such an optical model potential.

The optical model potentials are spin-dependent since nucleon-nucleon interactions are spin-dependent. The introduction of a spin-dependent part to the potential improved the fits to the elastic scattering data. The potential may depend on the spin of the projectile and/or target and L-S coupling is assumed for nucleons involved in the reaction. However, for larger projectiles, for example, deuteron, second rank tensor couplings are assumed.

2.1.2 The form of the potentials

The spherically-symmetric optical potential $U(r_\alpha)$ has a real part which is flat and attractive (i.e. negative). The short range nuclear force is mimicked by this real part which rises rapidly and monotonically to zero at the surface of the nucleus. The most commonly used analytic form for the real part of the central potential is the Woods-Saxon[4] "volume" form.

It is given by

$$\text{Re } U(r) = -V_R \, f(x_R) \quad \text{where } f(x_i) = (e^x - 1)^{-1}$$
$$\text{and } x_i = (r - R_i)/a_i$$

where V_R is the well depth. R_R is the radius and a_R the surface diffuseness. Then as $x_R \to -\infty$, Re U(r) $\to$ -V and as $x_R \to +\infty$, Re U(r) $\to$ 0.

The "volume" part of the potential was assumed to have both real and imaginary parts when it became clear that flux absorption occurs in direct reactions. The imaginary part has the same form as Re U(r):

$$\text{Im } U(r) = -W \, f(x_w) \quad \text{where } x_w = (r - R_w)/a_w.$$

The complex part of the potential is usually assumed to have a "volume" and a "surface" term. The "surface" term is proportional to the first derivative of f(x) and has the form

$$\text{Im } U(r) = 4W_D \, df(x_D)/dx_D$$
$$= -4W_D \exp(x_D)/((\exp(x_D) + 1)^2$$

where $x_D = (r - R_D)/a_D$. The factor of 4 is inserted because this surface potential peaks at $r = R_D$. The Woods-Saxon and Woods-Saxon derivative optical potential shapes for a nucleon impinging on an A~100 nucleus are shown in figure (2.1).

(Fig. 2.1 on page 17).

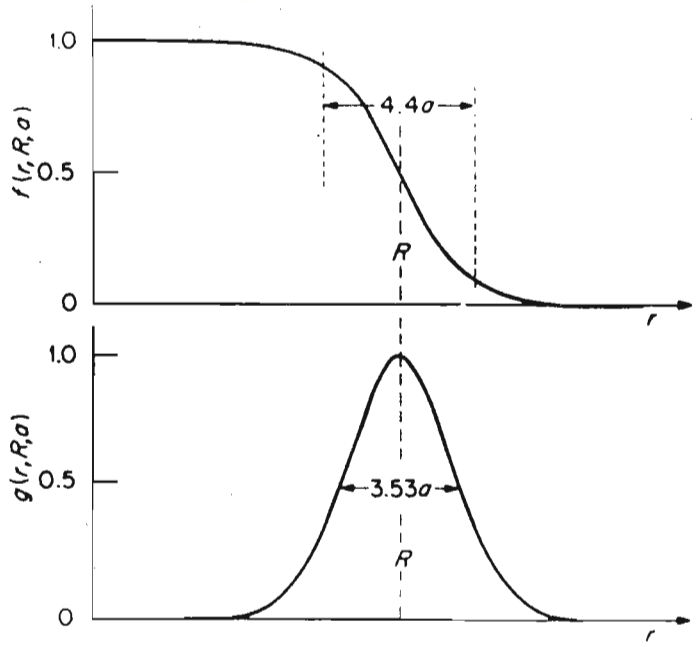

Fig. 2.1 Woods-Saxon optical potential shape f(x) and the Woods-Saxon first derivative optical potential shape g(x). Reproduced from ref. (1).

Spin-orbit coupling has become a necessary addition to the family of optical model potentials, although several examples of global optical potential sets (see Hodgeson[5][6]) leave out the spin-orbit part. In the type of reaction considered in this study the spin-orbit interaction is restricted to the surface region of the nucleus and the phenomenologically accepted form of a potential for such an interaction is

$$U_{so} = V_{so} (\hbar/m_{\pi}c)^2 \; r^{-1} \; df(x_{so})/dr \; \underline{L}.\underline{S}$$

where $x_{so} = (r-R_{so})/a_{so}$. To be able to express V_{so} in MeV $(\hbar/m_{\pi}c)^2$ must be set to be 2.00 fm^2. If the bombarding energy is more than 100 MeV, then it is necessary for V_{so} to be complex.

When charged particles are involved in a reaction it is necessary to bring in to play the Coulomb potential. This potential has a slow 1/r drop off so that it has a presence within and without the nucleus. The form of this potential depends on the mathematical picture adopted for the charge distributions involved. If a point-charge form is assumed for the projectile (charge $Z_a e$) and the target nucleus (charge $Z_A e$, radius R_{CH}) then

$$U_c(r) \begin{cases} = (Z_a\ Z_A\ e^2)/r & r \geq R_{CH} \\ = (Z_a\ Z_A\ e^2)/2R_{CH} \times [3 - r^2/R^2_{CH}] & \text{for } r \leq R_{CH} \end{cases}$$

A more precise formulation of this Coulomb potential involves the use of the single-folded expression for the target nucleus

$$U_c(r) = e\int [\theta_{CH}(r') / |\underline{r} - \underline{r}'|]\, d\underline{r}'.$$

θ_{CH} is the spherically-symmetric charge distribution for the target nucleus. If compound projectiles are involved in the reaction then a double-folded potential has to be used. The co-ordinate scheme for the single and double-folded Coulomb potential are shown in figure (2.2).

All of these potentials have as one of their parameters potential radii. The nuclear radius is generally taken as being proportional to $A^{1/3}$. These potential radii are then given as

$R_i = r_i\ A^{1/3}$ where i = R, W, D, SO, and r_i is a radius parameter independent of A.

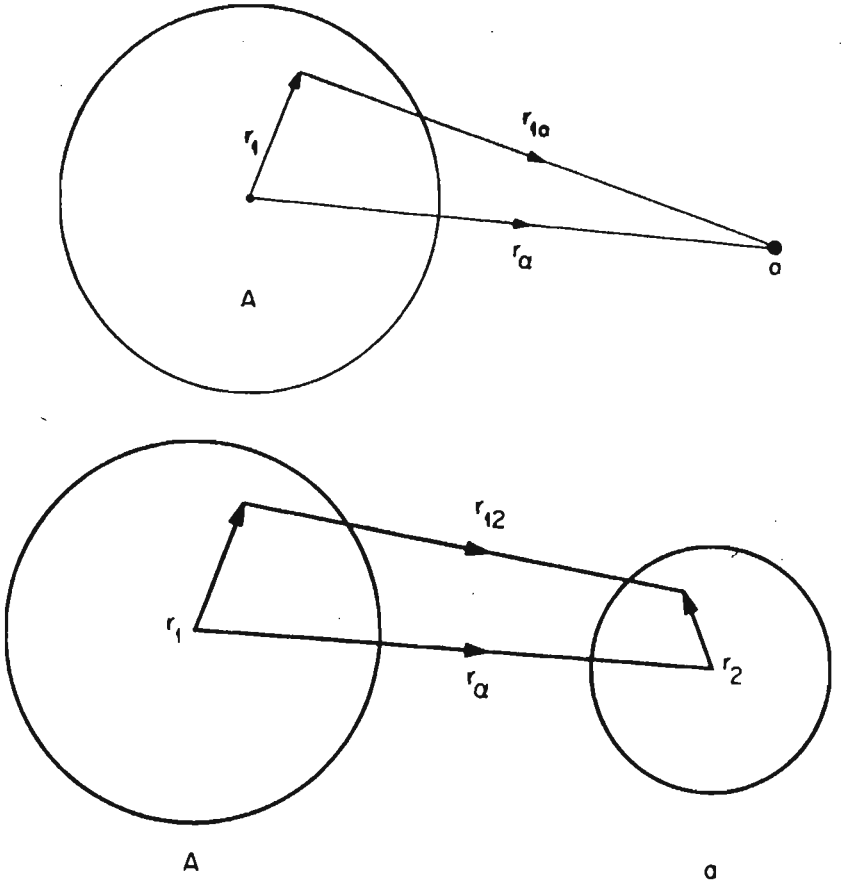

Fig. 2.2 Coordinates used for (a) simple-folding and (b) double-folding of the Coulomb potential. Reproduced from ref. (2).

The optical potential parameters have a smooth dependence on energy and on changing A. (See figure (2.3) from reference (2)). If they have an erratic dependence on mass number then this may be traced to underlying changes in nuclear structure. |W| increases with energy [7],[8] since more channels become available to drain flux from the incident (or elastic) channel. On the other hand, |V| decreases as the incident energy increases [7],[8] and this is attributed to the nucleon-nucleon interaction[2].

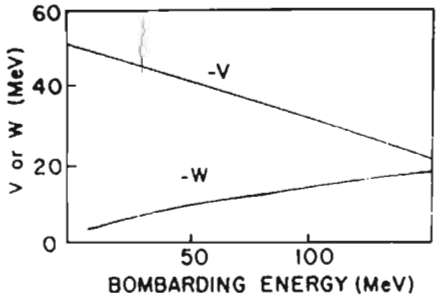

Fig. 2.3 The smooth dependence of V and W with respect to energy. Reproduced from ref. (2).

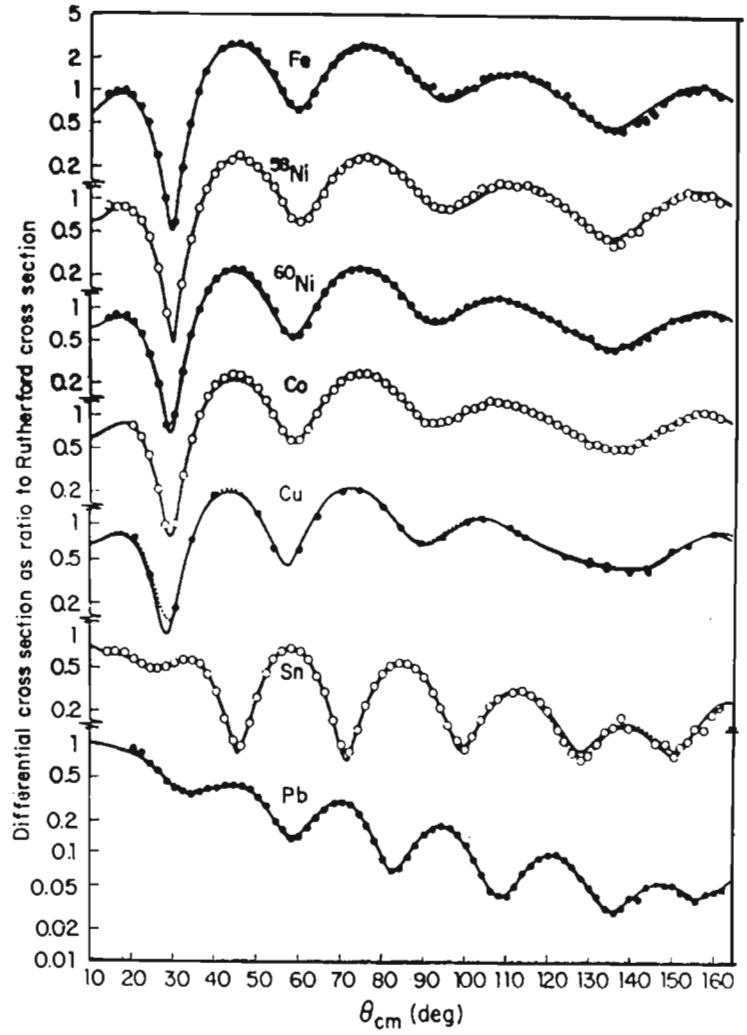

Fig. 2.4 Elastic scattering cross-sections for 30 MeV protons and optical model calculations. Reproduced from ref. (2).

The use of optical model potentials to produce fits for elastic scattering data has been very successful. (See figure 2.4[1]). However, ambiguities do persist both in the interpretation of the potential and in the use of the potentials.

2.2 The distorted-waves method

The underlying premise in the distorted wave theories of direct nuclear reactions is that the dominant aspect of a two-particle collision is the elastic scattering part of the reaction. The aim of the theories then is to solve the eleastic scattering exactly and then to treat the other parts of the reaction as perturbations. This treatment requires the development of the distorted wavefunctions that describe the elastic scattering "exactly". These distorted waves are generated by using optical model potentials whose parameters are chosen so as to obtain the best possible fits to elastic scattering data at the appropriate energy.

In the plane-wave Born approximation (PWBA) treatment of direct reactions, momentum and angular momentum conservation are easily visible. The transition amplitude in the PWBA formulation (for the reaction A(a,b)B) has the form

$$T_{BA} \propto \int j_\ell (Qr)\, f_\ell(r)\, r^2\, dr$$

where ℓ is the transferred orbital angular momentum. Stripping or pick-up reactions are very selective in their choice of partial waves so that the angular distribution of the cross-section of a reaction is oscillatory with a particular ℓ-Bessel function. However, in the distorted-wave theories the transition amplitudes of these direct reactions cannot be expressed simply in terms of Bessel functions or other simple mathematical forms. But it is still possible to make unambiguous assignments of ℓ-values in distorted-wave reaction studies by comparing

distorted-wave cross section calculations with experimentally observed cross-sections. (See figures (2.5) and (2.6)).

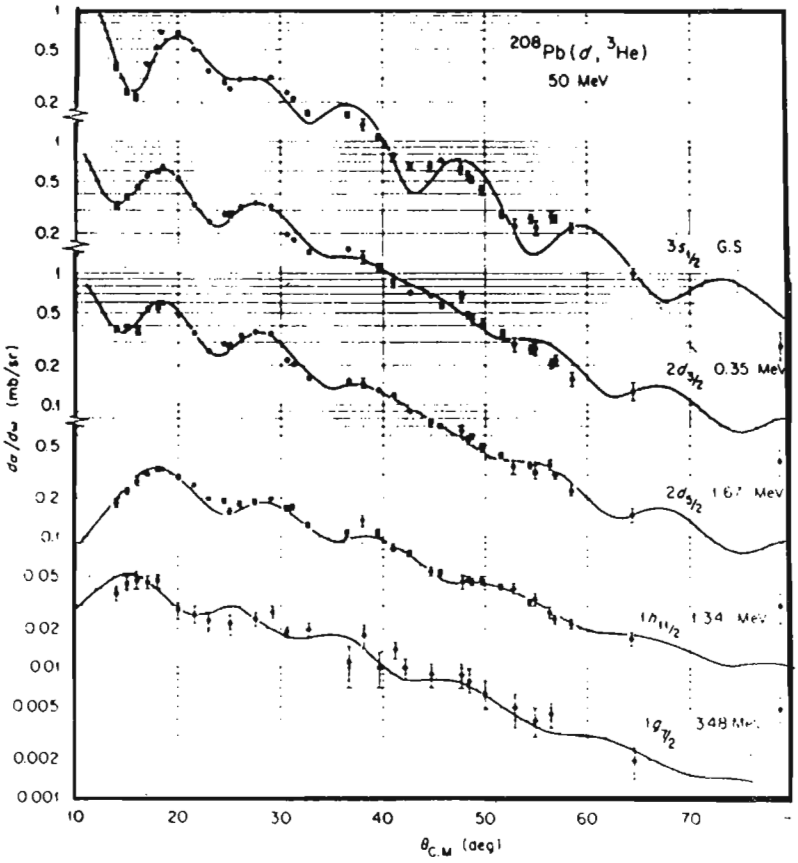

Fig. 2.5 DWBA fits to proton pick-up reaction cross-sections. Reproduced from W. Parkinson et al, Phys.Rev. 178 (1969) 1976.

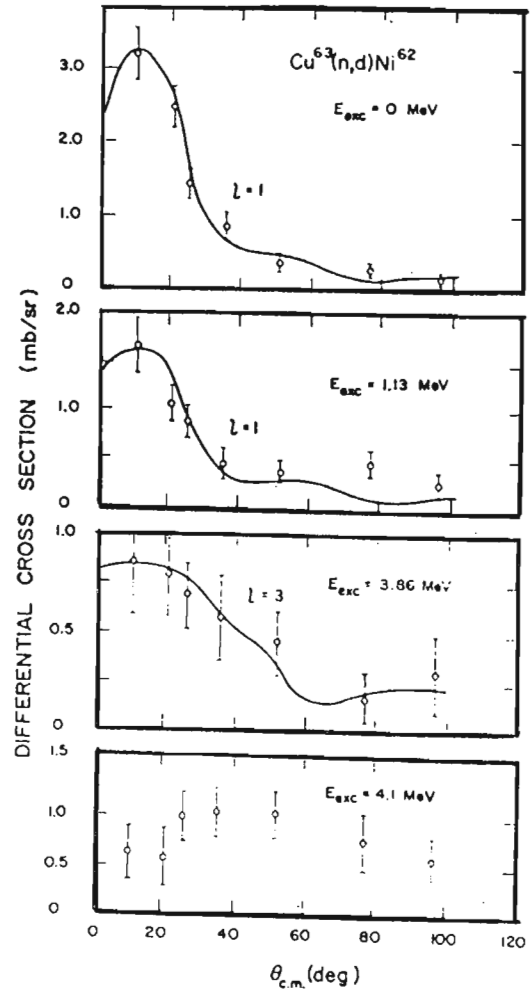

Fig. 2.6 DWBA fits to (n,d) reaction cross-sections. Reproduced from W. N. Wang and E. J. Winhold, Phy.Rev.B140 (1965)882.

Consider an interaction between two nuclei a and A in the α channel (which is the incident channel). This interaction is

described by

$$V_\alpha \equiv V_\alpha(x_\alpha, r_\alpha)$$

where x_α is the set of internal coordinates in the α channel and $\underline{r}_\alpha$ is the vector that joins the centres-of-mass of a and A in the α channel. The Hamiltonian for the system then is

$$H = H_\alpha + T_\alpha + V_\alpha \qquad \text{-----} \qquad (2.2)$$

where T_α is the kinetic energy of the relative motion of a and A in the incident channel and H_α is the sum of the internal Hamiltonians of a and A. If it is assumed that the total wave-function for this system is Π, then it must satisy the Schrodinger equation

$$(E - H)\ \Pi = 0.$$

Π may be expressed [1),(2),(9)] as the sum of a complete set of internal states μ_α where

$$\mu_\alpha(x_\alpha) \equiv \mu_a(x_a).\ \mu_A(x_A)$$

as

$$\Pi = \Sigma_\alpha\ \phi_\alpha(\underline{r}_\alpha).\ \mu_\alpha(x_\alpha)\ , \qquad \text{-----} \qquad (2.3)$$

the sum being over all available internal states of partition α. $\phi_\alpha(\underline{r}_\alpha)$ describes the relative motion of the nuclei in the α channel. Equation (2.3) may be inverted to get

$$\phi_\alpha(\underline{r}_\alpha) = (\mu_\alpha \mid \Pi)$$
$$= \int (\mu_\alpha^*(x_\alpha)\ \Pi\ dx_\alpha \qquad \text{-----} \qquad (2.4)$$

Π will be described fully only if the necessary boundary conditions are applied to it.

Consider some bombarding energy E, at which several channels which contain outgoing spherical waves are open. Then, if the incident relative momentum is $\underline{k}_\alpha$ the incident wave may be expanded in terms of the states of some partition β as follows

$$\Pi_\alpha^{(+)} = \Sigma_\beta \; \phi_\beta(\underline{r}_\beta) \cdot \mu_\beta(x_\beta) \qquad \text{-----} \qquad (2.5)$$

In a fashion analogous to equation (2.4) above

$$\phi_\beta(\underline{r}_\beta) = (\mu_\beta \mid \Pi_\alpha^{(+)})$$

and, following reference (1), this function has the following asymptotic form

$$\phi_\beta(\underline{r}_\beta) \approx \exp(i\underline{k}_\alpha \cdot \underline{r}_\alpha) \; \delta_{\alpha\beta} + f_{\beta\alpha}(\underline{r}_\beta, k_\alpha) \; r_\beta^{-1} \exp(ik_\beta r_\beta) \qquad \text{-----} \qquad (2.6)$$

as $r_\beta \to \infty$. $\underline{r}_\beta$ is a unit vector. $f_{\beta\alpha}$ is a scattering amplitude of the outgoing wave in channel β induced by a plane wave in the incident channel.

The differential cross-section for the reaction is given by

$$d\sigma_{\beta\alpha}/d\Omega = (v_\beta/v_\alpha) \; |f_{\beta\alpha}(\underline{k}_\beta, \underline{k}_\alpha)|^2 \qquad \text{-----} \qquad (2.7)$$

The factor (v_β/v_α) enters into this expression because $f_{\beta\alpha}$ is a scattering amplitude while the differential cross-section involves fluxes. The transition amplitude in terms of $f_{\beta\alpha}$ is given by

$$T_{\beta\alpha} = - (2\pi\hbar^2/\mu_\beta) \; f_{\beta\alpha} \qquad \text{-----} \qquad (2.8)$$

and equation (2.6) may then be written in terms of $T_{\beta\alpha}$ as

$$d\sigma_{\beta\alpha}/d\Omega = (\mu_\alpha\mu_\beta/4\pi^2\hbar^4)\ (k_\beta/k_\alpha)\ |T_{\beta\alpha}(\underline{k}_\beta,\underline{k}_\alpha)|^2 \qquad \text{-----} \qquad (2.9)$$

To obtain a functional form for equation (2.9) it is necessary to solve the Schrodinger equation with a suitable Hamiltonian. The Hamiltonian described in equation (2.2) above does not cater for the use of perturbation theory and this is corrected by introducing into it the optical model potential. The Schrodinger equation associated with this Hamiltonian (2.2) is just

$$(E - H_\beta - K_\beta)\ \Pi_\alpha^{(+)} = V_\beta\ \Pi_\alpha^{(+)} \qquad \text{-----} \qquad (2.10)$$

where $H_\alpha + K_\alpha + V_\alpha = H_\beta + K_\beta + V_\beta =$ ..... for each possible partition. The optical potential $U(r_\alpha)$ may be subtracted from both sides of equation (2.10) giving

$$[E - H_\beta - K_\beta - U_\beta(r_\beta)]\ \Pi_\alpha^{(+)} = [V_\beta - U_\beta(r_\beta)]\ \Pi_\alpha^{(+)} \qquad \text{-----} \qquad (2.11)$$

and

$$[E - K_\beta - U_\beta(r_\beta)]\ \phi_\beta(\underline{r}_\beta) = (\mu_\beta\ |\ W_\beta\ |\ \Pi_\alpha^{(+)}) \qquad \text{-----} \qquad (2.12)$$

where $W_\beta = V_\beta - U_\beta(r_\beta)$ is the residual interation. If $U_\beta(r_\beta)$ includes a major part of V_β then W_β is small enough to be treated as a perturbation. $U_\beta(r_\beta)$ is the selected optical model potential that provides the best interpretation of the elastic scattering part of the reaction. This minimizes W_β.

The formal solution of equation (2.12) is given[1] in

terms of the solutions of the homogeneous equation

$$[E_\beta - K_\beta - U_\beta(r_\beta)] \quad \epsilon_\beta^{(+)} (\underline{k}_\beta, \underline{r}_\beta) = 0 \text{ -----} \qquad (2.13)$$

The (+) sign signifies the composition of the $\epsilon_\beta^{(+)}$. It has the asymptotic form of an incident plane wave and outgoing spherical waves. These wavefunctions are the distorted waves which describe the elastic scattering of b and B mediated by $U_\beta(r_\beta)$ itself. These distorted waves are an integral aspect of the distorted-waves method. The transition amplitude in this formalism requires explicit functional forms for these waves which have to be obtained from a solution of equation (2.13) with the imposition of boundary conditions.

To obtain more information on the transition amplitude it is necessary to apply Green's function techniques to equation (2.12). Austern[9] shows that a formal solution of equation 2.12 is

$$\phi_\beta = \epsilon_\alpha^{(+)} \delta_{\alpha\beta} + [E - e_\beta - K_\beta - U_\beta + ie']^{-1} (\mu_\beta \, |W_\beta| \, \Pi_\alpha^{(+)})$$

where the $+ie'$ is introduced to ensure that there is no division by zero. The full Schrodinger equation (equation (2.11)) may then be rewritten (choosing $\beta = \alpha$) as

$$\Pi_\alpha^{(+)} = \epsilon_\alpha^{(+)} \mu_\alpha + [E - H_\alpha - K_\alpha - U_\alpha + ie']^{-1} \times (V_\alpha - U_\alpha) \, \epsilon_\alpha^{(+)} \mu_\alpha$$

$$= [1 + G^{(+)} (V_\alpha - W_\alpha)] \, \epsilon_\alpha^{(+)} \mu_\alpha \text{ -----} \qquad (2.14)$$

where $G^{(+)}$ is $[E - H + ie']^{-1}$. Information on scattering by the optical potential $U_\alpha(r_\alpha)$ is carried in the distorted wave

$\varepsilon_\alpha^{(+)}$ while the remainder of the scattering is due to the residual interaction, $(V_\alpha - U_\alpha(r_\alpha))$.

The operator relation $B = A + (B - A)$, assuming non-commutivity, can be written as

$$A^{-1} = B^{-1} + B^{-1} (B - A) A^{-1} \qquad \text{-----} \qquad (2.15)$$

by dividing from the left by B and from the right by A. Iteration of equation (2.15) gives

$$A^{-1} = B^{-1} + B^{-1} (B - A) A^{-1} + B^{-1} (B - A) B^{-1} (B - A) B^{-1} + \text{.....} \qquad \text{-----} \qquad (2.16)$$

In the full Schrodinger equation (equation (2.14)), let

$A = [E - H_\alpha - K_\alpha - V_\alpha + ie']$ and

$B = [E - H_\alpha - K_\alpha - U_\alpha + ie']$ so that

$B - A = V_\alpha - U_\alpha(r_\alpha) = W_\alpha$

These may be substituted into equation (2.16) giving

$$A^{-1} = G^{(+)} = [1 + G_\alpha^{(+)\prime} W_\alpha + G_\alpha^{(+)\prime} W_\alpha G_\alpha^{(+)\prime} W_\alpha + \text{....}] \, G_\alpha^{(+)\prime} \qquad \text{---} \qquad (2.17)$$

where $G_\alpha^{(+)\prime} = [E - H_\alpha - K_\alpha - U_\alpha + ie']^{-1}$ is the distorted-waves propagator for the optical potential $U_\alpha(r_\alpha)$.

Substituting (2.17) in (2.14) gives

$$\Pi_\alpha^{(+)} = [1 + G_\alpha^{(+)\prime} W_\alpha + G_\alpha^{(+)\prime} W_\alpha G_\alpha^{(+)\prime} W_\alpha + \text{....}] \varepsilon_\alpha^{(+)} \mu_\alpha \qquad \text{-----} \qquad (2.18)$$

In the distorted-waves formalism, the expression that emerges for the transition amplitude[1] is

$$T_{\beta\alpha}(\underline{K}_\beta,\underline{k}_\alpha) = T_\beta^{(o)}(\underline{k}_\beta,\underline{k}_\alpha)\ \delta_{\beta\alpha} + \langle \varepsilon_\beta^{(-)}(\underline{k}_\beta).\ \mu_\beta\ |W_\beta|\ \Pi_\alpha^{(+)}(\underline{k}_\alpha)\rangle$$

$$= T_\beta^{(o)} + T_{\beta\alpha}'$$

where $T_\beta^{(o)}$ is the transition amplitude for the elastic reaction. Then the expression for the transition amplitude for the rest of the reaction, for example the single-nucleon transfer reaction, using equation (2.18) is

$$T_{\beta\alpha}' = \langle \varepsilon_\beta^{(-)}\mu_\beta\ |W_\beta + W_\beta G_\alpha^{(+)\prime} W_\alpha + W_\beta G_\alpha^{(+)\prime} W_\alpha G_\alpha^{(+)\prime} W_\alpha + \ldots.$$

$$| \varepsilon_\alpha^{(+)}\mu_\alpha\rangle \quad \text{---- (2.19)}$$

Then finally, the transition amplitude for the distorted wave Born approximation (DWBA) is

$$T^{DWBA} = \langle \varepsilon_\beta^{(-)}\ \mu_\beta |\ W_\beta\ |\varepsilon_\alpha^{(+)}\ \mu_\alpha\rangle . \qquad \text{----- (2.20)}$$

In general, the distorted-wave series in (2.19) does not converge[1][10]. It is for this reason that some authors[1] do not refer to this formalism as the distorted wave Born approximation (DWBA) method but as the distorted-waves method.

The transition amplitude in equation (2.20) may be written explicitly as

$$T_{\beta\alpha} = \iint d\underline{r}_\beta d\underline{r}_\alpha\ \varepsilon_\beta^{(-)}(\underline{k}_\beta,\underline{r}_\beta)^*\ (\mu_\beta|W|u_\alpha)\ \varepsilon_\alpha^{(+)}(\underline{k}_\alpha,\underline{r}_\alpha)$$

$$\text{----- (2.21)}$$

Equation (2.21) demonstrates that the nuclear matrix element has become separated from the distorted waves.

The round brackets round the matrix element means that the integration is over the internal coordinates of the nuclei in the α and β channels. The separation means that the elastic part of the reaction (distorted waves) is separated from the non-elastic parts of the reaction. The nuclear matrix element

$$I_{\beta\alpha} = (\mu_\beta \mid W \mid \mu_\alpha)$$

contains information on the nuclear structure, on angular momentum and parity selection rules, and on the type of nuclear reaction that is occurring. It is interesting to note than an evaluation of the nuclear matrix amplitude in equation (2.21) leaves the transition amplitude as a six-dimensional integral. To make this manageable for computing purposes it may be reduced to a two-dimensional integral by making multipole and partial-wave expansions.

The nuclear matrix element $I_{\beta\alpha}$ is a function of the internal coordinates of the nuclei a, A, b, and B.

$$\begin{aligned} I_{\beta\alpha} &= I_\beta I_B M_B,\ I_b M_b,\ \alpha I_A M_A,\ I_a M_a (\underline{r}_\beta, \underline{r}_\alpha) \\ &= J_{\beta\alpha} \int d\theta_\beta\ \mu_{I_B M_B}(x_B)^*\ \mu_{\underline{r}_b M_b}(x_b)^* \\ &\qquad \times W\ \mu_{I_A M_A}(x_A)\ u_{I_a M_a}(x_a) \quad \text{-----} \end{aligned} \tag{2.22}$$

where the I_B, I_b, I_A, and I_a are the total angular momenta of the nuclei B,b,A and a respectively while the M's refer to the z- projections of the total angular momenta. $J_{\beta\alpha}$ is a Jacobian to cater for the transformation of the internal coordinates.

The multipole expansion of the $I_{\beta\alpha}$ leads to a separation of the nuclear matrix element into terms that correspond to angular momentum transfers between the different parts of the colliding system. To perform this expansion formally it is necessary to define the angular momentum transfers that are involved. Let

$$\underline{J}_{BA} \equiv \underline{I}_B - \underline{I}_A$$

$$\underline{J}_{ba} \equiv \underline{I}_b - \underline{I}_a \qquad \text{-----} \qquad (2.23)$$

$$\text{and} \quad \ell \equiv \underline{J}_{BA} + \underline{J}_{ba}$$

where ℓ is the orbital angular momentum transferred. Equations (2.23) allow the expression $\mu_{IM}^* \mu_{IM}$ in the nuclear matrix element to be expressed as a sum of vector-coupled terms.

$$\mu_{I_BM_B}(x_B)^* \mu_{I_AM_A}(x_A)$$

$$= \Sigma_{J_{BA}} \langle I_B I_A M_B, -M_A \mid J_{BA} M_{BA} \rangle \times (-)^{I_A - M_A} \oint^{M_{BA}}_{I_B I_A J_{BA}} (x_B, x_A)^*$$

where $M_{BA} = M_B - M_A$. A similar treatment is possible for

$$\mu_{I_b M_b}(x_b)^* \mu_{I_a M_a}(x_a)$$

being a sum of terms through J_{ba}. These expansions are possible only if the μ_{IM} behave as $(-)^{I-M} \mu_{I,-M}$ and vice versa, under rotation of the coordinates.

These sets of terms may be combined in accordance with the third equation of (2.23).

$$\Phi^{M_{BA}}_{I_B I_A J_{BA}}(x_B, x_A)^* \; \Phi^{M_{ba}}_{I_b I_a J_{ba}}(x_b, x_a)^*$$

$$= \sum_{\ell} \langle J_{BA}\, J_{ba}\, M_{BA}, M_{ba} \mid \ell\, m \rangle$$

$$\times \Phi^{J}_{(I_b I_a) J_{ba}\,(I_B I_A) J_{BA}, \ell}(x_\beta, x_\alpha) \qquad \text{--------} \quad (2.24)$$

where $m = M_{BA} + M_{ba}$.

The multipole expansion of the $I_{\beta\alpha}$ may then be written as[1][2][3]

$$I_{\beta I_B M_B} \cdot I_{b M_b} \cdot {}_{\alpha} I_{A M_A} \cdot I_{a M_a}(\underline{r}_\beta, \underline{r}_\alpha)$$

$$= \sum_{J_{BA}\, J_{ba}\, \ell} \langle I_b I_a M_b, -M_a \mid J_{ba} M_{ba} \rangle \langle I_B I_A M_B, -M_A \mid J_{BA} M_{BA} \rangle$$

$$\times \langle J_{ba} J_{BA} M_{ba} M_{BA} \mid \ell\, m \rangle (-)^{I_A - M_A + I_a - M_a} G_{\ell\, J_{BA} J_{ba}}(\underline{r}_\beta, r_\alpha)$$

$$\text{-------} \quad (2.25)$$

where the $G_{\ell\, J_{BA}\, J_{ba}}$ are the multipole components. Equation (2.25) may be inverted to produce the multipole components in terms of the Clebsch-Gordan coefficients and the nuclear matrix element.

The isospin representation has been ignored. However, if the isospin had been included then equation (2.25) would have had additional Clebsch-Gordan coefficients and a sum over the isospin transfer, t.

Finally, the transition amplitude (2.21) can be expressed in terms of the multipole components as follows

$$T^{DW}_{\beta\alpha}(\underline{k}_\beta,\underline{k}_\alpha) = \Sigma_{J_{BA}} \langle I_B\, I_A\, M_B\ ,\ -M_A \mid J_{BA}\, M_{BA}\rangle$$
$$\times\ (-)^{I_A - M_A} \Sigma_{J_{ba}\ell}\ \mathbf{t}^{m\, M_b\, M_a}_{\ell\, J_{ba}\, J_{BA}}(\theta,\phi)$$

where t is called the reduced amplitude. Following equations (2.21) and (2.25) the reduced amplitude may be expressed as

$$\mathbf{t}^{m\, M_b\, M_a}_{\ell\, J_{ba}\, J_{BA}}(\theta,\phi) = \Sigma_{M_b, M_a,}\ \langle I_b\, I_a\, M'_b\ ,\ -M'_a \mid J_{ba}\, M'_{ba}\rangle$$
$$\times\ \langle J_{ba}\, J_{BA}\, M'_{ba}\ \ M_{BA} \mid \ell\, m'\rangle$$
$$\times\ (-)^{I_a - M'_a} \int d\underline{r}_\beta \int d\underline{r}_\alpha\ \ \epsilon^{(-)}_{M_b, M_b}(\underline{k}_\beta, \underline{r}_\beta)^*$$
$$\times\ G_{\ell\, J_{BA}\, J_{ba}}(\underline{r}_\beta, \underline{r}_\alpha)\ \epsilon^{(+)}_{M_a, M_a}(\underline{k}_\alpha, \underline{r}_\alpha)$$

-------- (2.26)

The distorted-wave cross-section angular distributions are determined by the ℓ-transfer. However, it is also possible to make j-value assignments by comparing the theoretical and experimental angular distributions. This angular distribution dependence on j has 3 sources:

(a) The radial part of the bound state wavefunction for transferred particle is dependent on j. This is mimicked by the optical potential that is chosen for the bound particle wavefunction. It has a spin-orbit part. However, this is a minor effect.

(b) The distorted waves are spin-dependent because of the spin-orbit coupling term in the distorting potentials.

(c) In the case of transfer reactions which involve two or more-nucleon particles, it is necessary to include in the calculations the non-S components (for example, the D-state in deuteron). This topic is covered in a paper by Lee and Schiffer[11]. Figure (2.7), which is reproduced from reference (1), demonstrates this j-dependence of the distorted-wave method calculations.

The nuclear matrix element contained in the expression for the transition amplitude contains the overlaps (μ_B,μ_A) and (μ_b,μ_a). A measure of these overlaps is the spectroscopic factor, for example, $S_{\ell j}(A,x|B)$ which represents the probability that when B is in state μ_B it is composed of x (with orbital angular momentum ℓ and total angular momentum j relative to A) and A in state μ_A. One way to check on the validity of the distorted-waves method analysis of a reaction is to compare the calculated cross-sections with experimental cross-sections so as to extract spectroscopic factors, which can then be compared with theoretically calculated spectroscopic factors.

This interpretation of direct nuclear reactions (especially light ion reactions) has been extensively studied and tested[12][13][14].

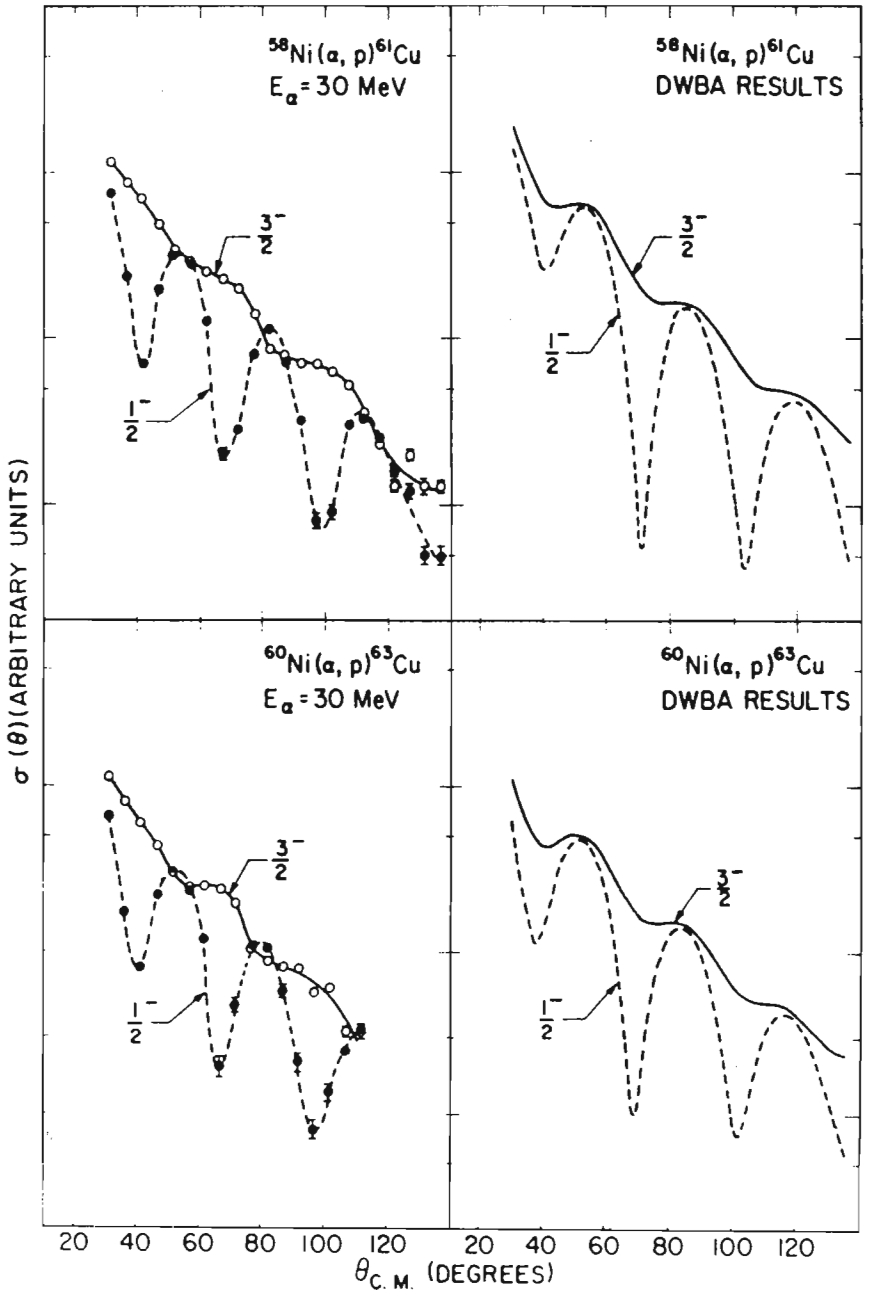

Fig. 2.7 DW calculations for $\ell = 1$ transfers demonstrating j-dependence. Reproduced from August, Shapiro and Cooper, Phys.Rev.Lett. 23 (1969) 537.

REFERENCES:

(1) G. R. Satchler, Direct Nuclear Reactions (Oxford Science publications, Oxford, 1983).

(2) N. K. Glendenning, Direct Nuclear Reactions (Academic Press, Inc., New York, 1983.

(3) F. G. Perey and D. S. Saxon, Phys. Lett. 10 (1964) 107.

(4) R. D. Woods and D. S. SAxon, Phys. Rev. 95 (1954) 577.

(5) D. Wilmore and P. E. Hodgeson, Nucl. Phys. 55 (1964) 673.

(6) P. E. Hodgeson, Rep. Prog. Phys. 47 (1984) 613.

(7) F. D. Becchetti and G. W. Greenlees, Phys. Rev. 182 (1969) 1180.

(8) W. W. Daehnick, J. D. Childs and Z. Vrcelj, Phys. Rev. C21 (1980) 2253.

(9) N. Austern, Direct Nuclear reaction theories (Wiley Interscience, New York 1970).

(10) K. R. Greider and L. R. Dodd, Phys. Rev. 146 (1966) 671.

(11) L. L. Lee and J. P. Schiffer, Phys. Rev. B136(1964) 405.

(12) P. G. Roos et al, Nucl. Phys. A255 (1975) 187.

(13) P. B. Foot et al, Phys. Rev. C31 (1985) 1133.

(14) B. M. Preedom, E. Newman and J. C. Hiebert, Phys. Rev. 166 (1968) 1156.

Chapter Three

The experimental details

3.1 Introduction

The $^{90}Zr(n,d)^{89}Y$ reaction is a proton pick-up reaction on ^{90}Zr. A comparison between experimentally obtained cross-sections and theoretically predicted cross-sections leads to information on the nuclear structure on ^{90}Zr and to the level scheme of ^{89}Y. The measurement of experimental deuteron cross-sections has been made possible with the aid of a spectrometer specifically designed to study neutron-induced charged-particle emission reactions[1][2]. The measurements were performed at the Van de Graaf accelerator facility at the National Accelerator Centre in Faure, South Africa. These neutron-induced particle emission reactions have been difficult to study experimentally[1]. The use of conventional silicon surface barrier ΔE-E telescopes results in a low reaction yield which increases the experimental runtime excessively. In addition, high background rates, competing reactions and neutron damage to the detectors were all unresolved problems. The present experiment improves on these problems.

The incident neutrons are produced in the d-t ($^{3}H(d,n)^{4}He$) reaction in a tritium gas-cell. The 6 MV Van de Graaf accelerator produces 5.25 MeV deuterons which are directed onto the gas cell. The d-t reaction, which has the very high, positive Q-value of 17.5 MeV, produces neutrons with ≈22 MeV energy[3].

3.2 The particle spectrometer

The particle spectrometer was designed by Professor K. Bharuth-Ram and Dr W.R. McMurray[1]. It consists of three multi-wire proportional counters (PC1, PC2, A/Co) and a plastic scintillator. (See figure (3.1). PC1 and PC2 are employed as "ΔE" detectors while the scintillator acts as an "E" detector, so that the spectrometer provides ΔE-E particle identification. In addition, the spectrometer allows for background suppression. However, its major advantage is that it permits simultaneous data accumulation over an 80° angle range with an angular resolution of ≈ 4° (FWHM); the reactions studied by this system are low yield reactions and this aspect of its functional ability decreases the required experimental run-time.

The proportional counters are approximately 6 mm thick and their active areas are of the order of 1000 mm^2. They are continuously bathed by a 10% methane - 90% argon mixture. The Zirconium target is a ^{90}Zr-enriched foil with a surface density of 15 mg/cm^2. It is a 10 mm wide strip and is positioned between the first and second proportional counters on the side of the incident neutron beam. A collimator, between the proportional counters PC1 and PC2, determines the effective height of the target foil as 12 mm. Included in this proportional counter sandwich are a series of thin wires (as "walls") between the A/Co and PC2 proportional counters to reduce the particle background. The EHT to the proportional counters was set by using the Am-Mo 17.5 keV X-ray source.

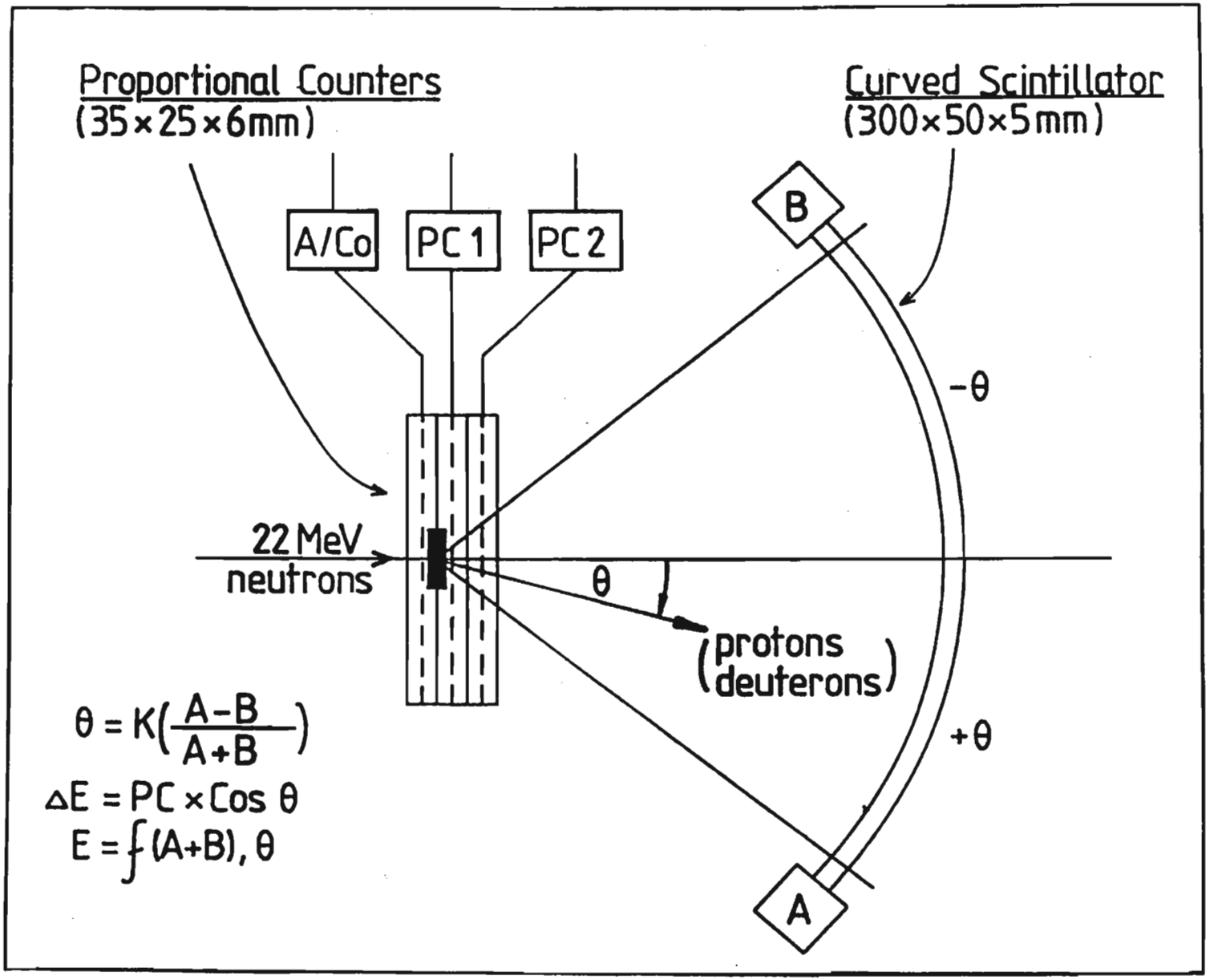

Fig. 3.1 Schematic diagram of the spectrometer designed by K. Bharuth-Ram and W.R. McMurray. (Reproduced from ref.(1).

The voltages were set to produce peak values of 2 volts for each of the proportional counters. The Am-Mo source is placed on the A/Co side of the sandwich.

PC1 and PC2 act in coincidence with the scintillator while A/Co acts in anticoincidence with PC1, PC2 and the scintillator. This ensures that events that do not originate in the ^{90}Zr-target are ignored.

The scintillator is 5 mm thick, 50 mm high, 300 mm long and has a radius of curvature of 200 mm. The geometry therefore subtends an angle of more than 80° at the target. It is viewed by two photomultipliers (labelled A and B in figure (3.1)) at its ends. The energy, E, signal is obtained by summing the outputs from A and B.

The electronics on the beam line and in the control room are shown schematically in figure (3.2). The signals from the "ΔE" detectors (PC1 and PC2) and the "E" detector (A+B) each contribute a fast pulse and a slow pulse. The fast pulses from PC1 and PC2 provide the start pulses for the two TAC's while the fast pulse from the scintillator provides the stop pulse for both TAC's. In addition, after coincidence/anticoincidence requirements are met these produce the gate pulses for the ADC's (analogue-to-digital converters). The slow pulses from the "ΔE" and "E" detectors are the ADC inputs for the ΔE and E information.

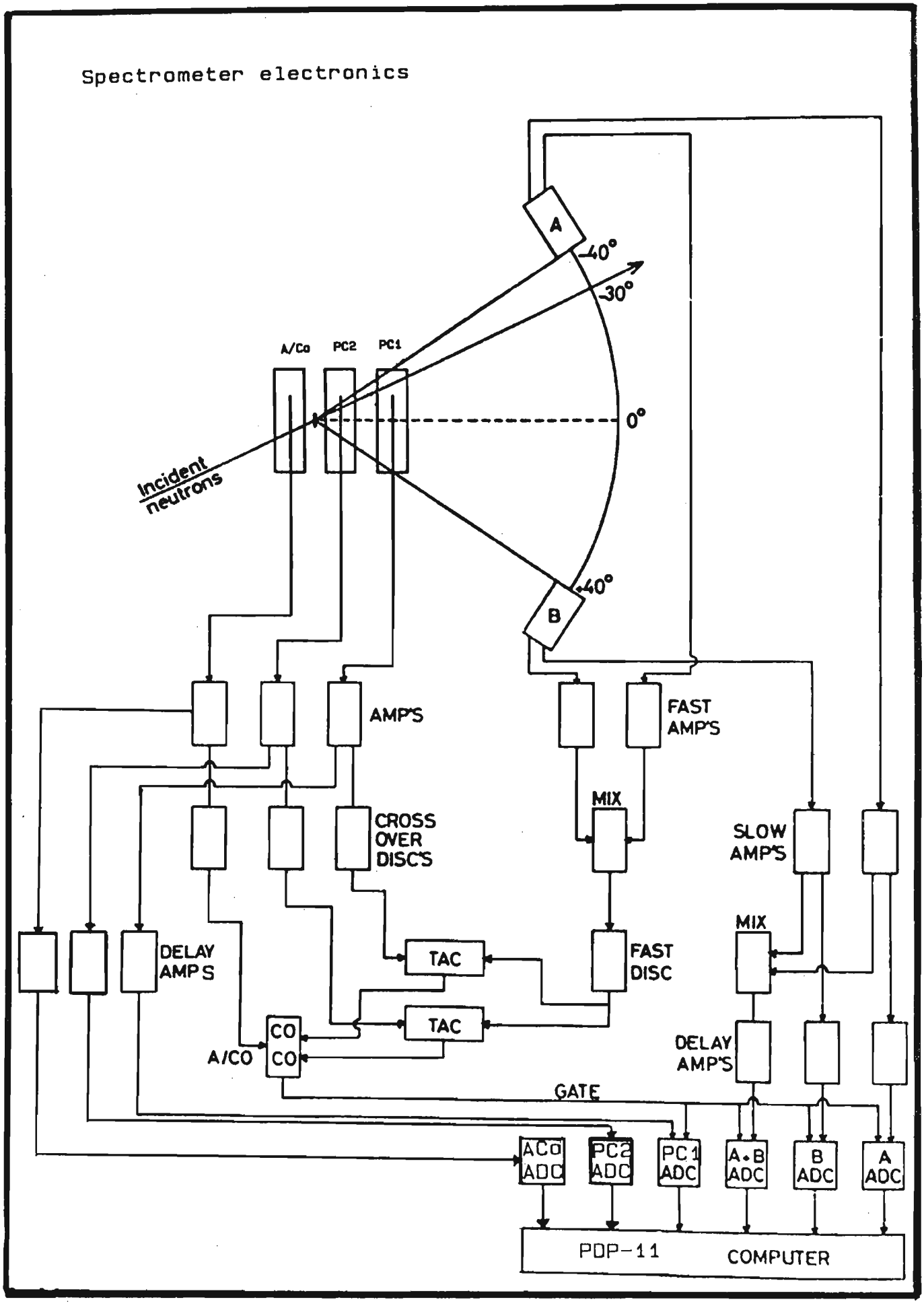
Spectrometer electronics
A
-40°
-30°
A/Co
PC2
PC1
0°
Incident neutrons
+40°
B
AMP'S
FAST AMP'S
MIX
CROSS OVER DISC'S
SLOW AMP'S
MIX
DELAY AMP'S
TAC
FAST DISC
TAC
CO
CO
A/CO
DELAY AMP'S
GATE
ACo ADC
PC2 ADC
PC1 ADC
A+B ADC
B ADC
A ADC
PDP-11 COMPUTER

3.2.1 The path for the fast pulses

The three proportional counters have their pulses fed through preamplifiers into spectroscopy amplifiers. These amplifiers have two outputs - a bipolar output and a unipolar one. The bipolar outputs are utilized for the fast pulse; they pass through windows and are delayed in constant fraction timing single-channel analysers and are amplified to have the same amplitude.

The pulses for the fast side from the photomultipliers, A and B, pass through amplitude windows and delays in timing single channel analyzers and are amplified to have the same amplitude for the same energy loss through the PC counters. The fast summed pulse passes through a constant fraction discriminator into a timing amplifier.

The PC1 and PC2 fast pulses become the start pulses for the two time-to-pulse-height converters/single-channel analysers. The A+B fast pulse acts as a stop pulse for each of the TAC's. The single-channel analyser outputs from these units are fed into linear gates in which they are delayed and adjusted to provide the correct gate-widths (see later). These pulses are the two coincidence pulses, which are the partial requirements for the triggering of an event. The fast pulse from A/Co after being appropriately delayed is fed into the coincidence unit, in anticoincidence with the two coincidence pulses, so as to eliminate events not originating in the target foil.

The output of the coincidence unit provides the gate pulse for the ADC's. Each pulse from this box is the count of an event.

3.2.2 The path for the slow pulses

The slow unipolar pulses of PC1, PC2 and A/Co are fed via delay amplifiers into the ADC's. The A and B slow pulses are fed through preamplifiers into spectroscopy amplifiers in which their amplitudes are adjusted to be the same for a particle detected in the centre of the scintillator. The unipolar outputs of these amplifiers are delayed and directed into the AD'c. In addition, for the purpose of providing a monitor during data accumulation the A and B pulses are summed in a dual sum and invert box and this (A+B) "energy" pulse is fed into an ADC.

3.2.3 The setting-up

^{207}Bi is a source of ≈1 MeV internal conversion electrons. The EHT's to the photomultipliers are set such that the ^{207}Bi source, at the midpoint of the scintillator (that is, at 0°) produces equal peaks of approximately 0.2 volts in each of A and B. The EHT is approximately 1530 volts for both the photomultipliers.

The fast timing gains, detector delays and bias settings were made with a 5.5 MeV proton beam on line from the accelerator. A long snout replaced the tritium cell in the setup procedure. The fast timing resolution for PC1/(A+B) and PC2/(A+B) were measured after time-calibrating the resulting TAC spectra, and are shown in figure (3.3).

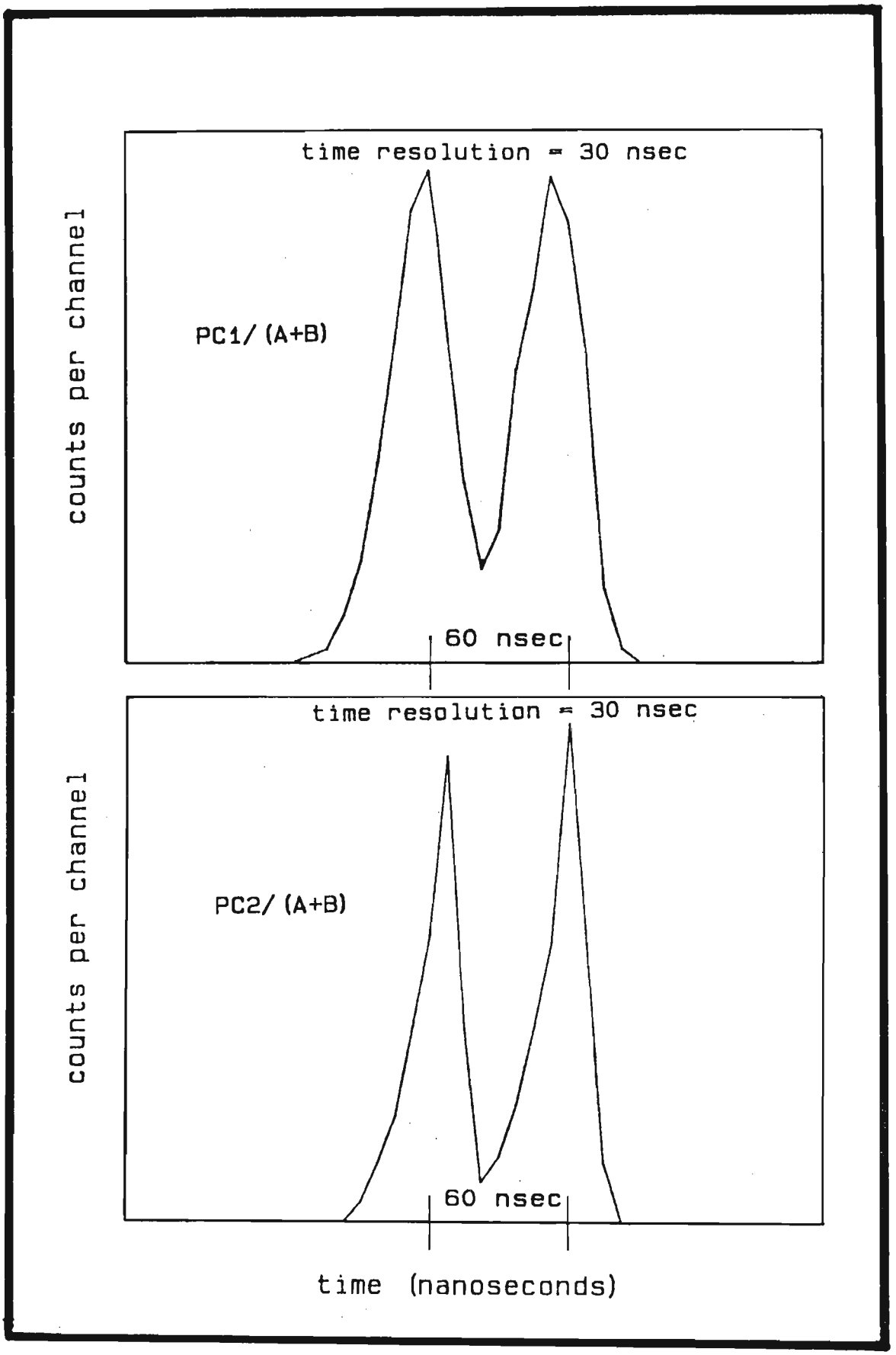

Fig. 3.3 The fast-timing resolution for PC1/(A+B) and PC2/(A+B).

The time between the PC1/(A+B) proton peaks is 60 nsec giving a timing resolution of 30 nsec. A similar result was found for the PC2/(A+B) case. It appears from these figures that PC2 had a better time response than PC1. Discriminator gates were imposed on the TAC output to eliminate events not contributing to the coincidence peaks, PC2 responded better than PC1.

The coincidence/anticoincidence conditions could now be set. The outputs of the two TAC's were delayed to satisfy the conditions shown in figure (3.4). An additional timing adjustment is necessary to ensure that the ADC slow inputs arrive after the gate pulse rising edge by about 0.5 μsec. Pulses which arrive before this time are rejected. Figure (3.5) demonstrates this condition.

The fast timing resolution was found to be improved by increasing the amount of methane in the methane-argon gas mixture that bathes the proportional counters. However, this has the effect of increasing the background in the proton spectra. (Whilst this study is of the (n,d) reaction, the system allows simultaneous accumulation of the (n,p) reaction data[4].) The real/random events ratio can be improved if the thickness of the scintillator is reduced to observe deuterons only in the energy range of interest, which is 9 to 18 MeV[1].

The data inputs A, B and (A+B) from the scintillator, and PC1 and PC2 from the proportional counters are gated by coincidence/anticoincidence requirements. They are accumulated in multi-parameter mode in the PDP-11 data acquisition system in the control-room of the accelerator. A program, written by Mr John Pilcher (of the National Accelerator Centre), performs the off-line analysis of the 5-parameter data collected

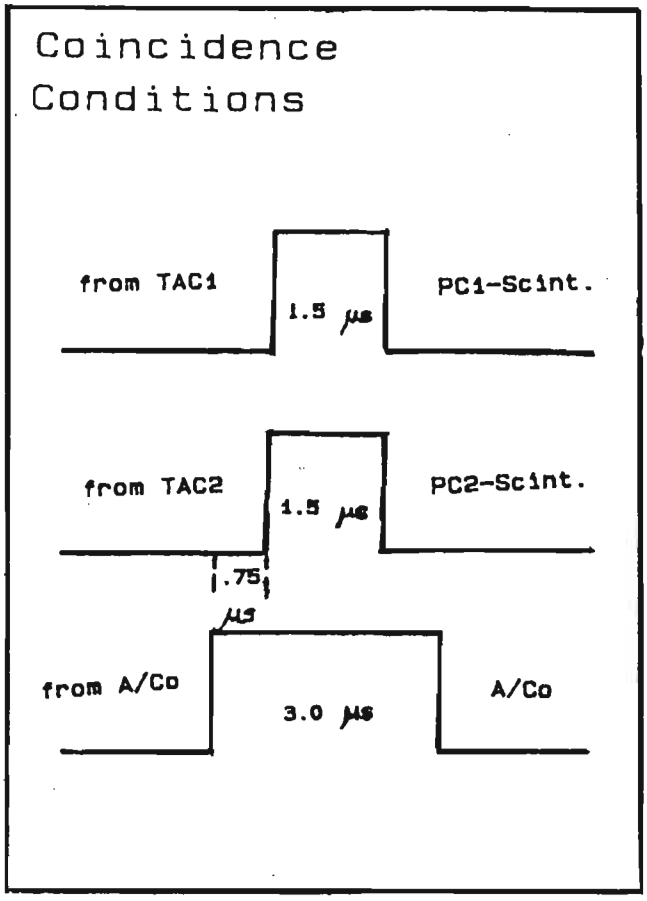

Fig. 3.4 The delays of the TAC1 and TAC2 output to meet coincidence/ anticoincidence requirements.

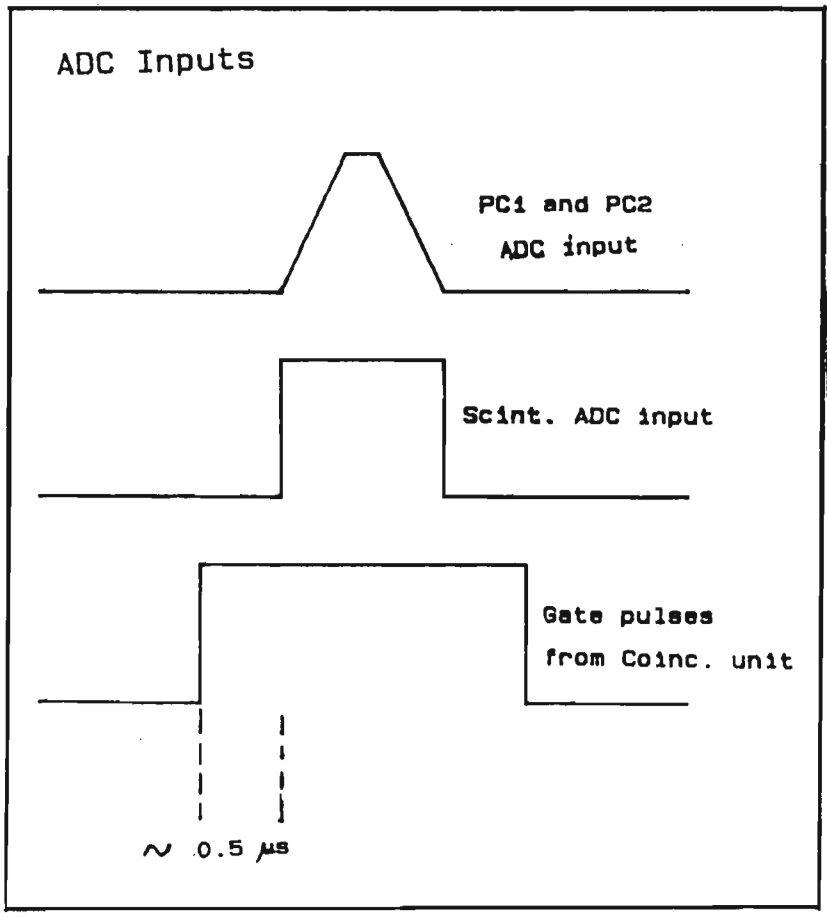

Fig. 3.5 Timing adjustment of the slow pulses in relation to the gate pulse.

The program, called PAID4, has the following facilities:

(a) It calculates the angle of detection of an event. This angle is computed as (see later)

$$\theta = k\ (A-B)/(A+B).$$

If additional higher order corrections to this calculation of the detection angle are required they may be performed as well. These will be described later.

(b) It makes angle-related corrections to the scintillator inputs, as follows:

$$E = f(A+B,\theta).$$

(c) It makes angle-related corrections to the inputs of the proportional counters as follows:

$$\Delta E_1 = PC1\ X\ \cos\theta \qquad \text{and} \qquad \Delta E_2 = PC2\ X\ \cos\theta.$$

(d) The identification of particles is greatly facilitated by the program's ability to draw in identification loci on two dimensional ΔE-E displays. This can be done separately for each of PC1 and PC2 for the sum of their inputs.

The spectrometer has been operated in vacuum and in air. The effect of in-vacuum operation on the energy loss of the deuterons and on the response of the scintillator to deuteron impingements are shown in figures (3.6) and (3.7). The major effect in this instance is the reduction in the detector threshold for both protons and deuterons, when the system is operated in vacuum. The deuteron energy loss in air becomes significant for low energy deuterons.

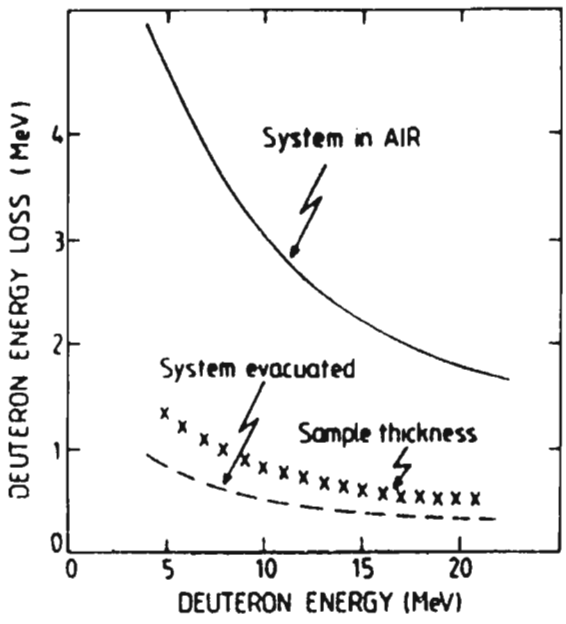

Fig. 3.6 **The effect of vacuum operation on the detection threshold of the scintillator. [Reproduced from Ref.(1)]**

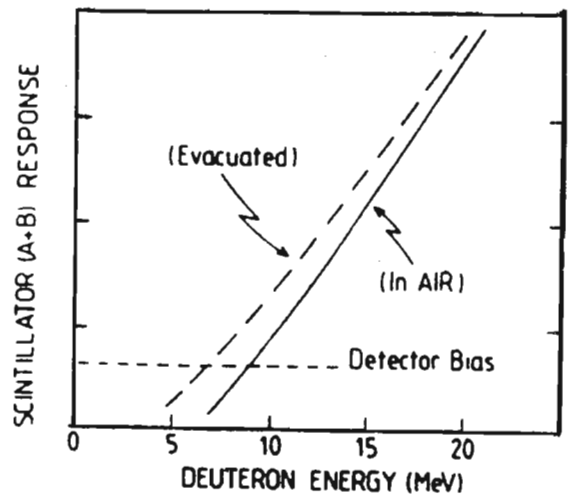

Fig. 3.7 **Deuteron energy loss in air and in evacuated chamber. [Reproduced from ref. (1)].**

3.2.4 The process of Particle Identification

PC1 and PC2 are the so-called "ΔE" detectors while the scintillator is the so-called "E" detector. The resulting ΔE-E plots are very suitable for particle identification. Seven ADC's are set up in the singles mode for the following parameters: A, B, (A+B), PC1, PC2, A/Co, TAC. They are all 1024 channels in size except for the TAC ADC which is set at 256 channels. In the multiparameter mode three monitoring spectra are set-up. They are each 4096 (64 X 64) channels in size. The parameters in the multiparameter set-up are as follows:

		X	Y
1.	64 X 64	A	B
2.	64 X 64	A+B	PC1

The particle identification efficiency is checked by using p-polythene, d-polythene and deuterated perspex samples from time to time during an experimental run. The samples are bombarded with 21.8 MeV neutrons and the particle identification loci are set (and checked). These loci are shown in figures (3.8) and (3.9). The 17 MeV proton spectrum from the p-poly sample and 19 MeV deuteron spectrum from the d-poly sample (in figure (3.10)) are obtained by lifting a slice out of the ΔE-E plot. As can be seen in the figure there is some overlap between the Landau distributions for the deuterons and protons which must indicate that particle identification is incomplete. However, it is adequate. Figures (3.11) and (3.12) show the spectra for the (n,p) and (n,d) reactions on ^{90}Zr respectively.

3.2.5 Angle determination

Angle calibration is performed with ^{207}Bi internal conversion electron source. The source is placed in machined slots (for this purpose) in the system which correspond to angular positions of -35°, 0°, and 35° at the scintillator. See figure (3.13). The process of angle determination depends on light attenuation and losses along the scintillator and this leads to a position sensitivity of the scintillator. Figure (3.13) shows that scintillator outputs, A and B, vary in a non-linear fashion with position. (A+B) varies more symmetrically with position and it was found [1] empirically that the ratio (A-B)/(A+B) is very nearly linear with respect to position. The value of k_1 (A-B)/(A+B) determines the position of an event on the scintillator relative to the incident neutron direction.

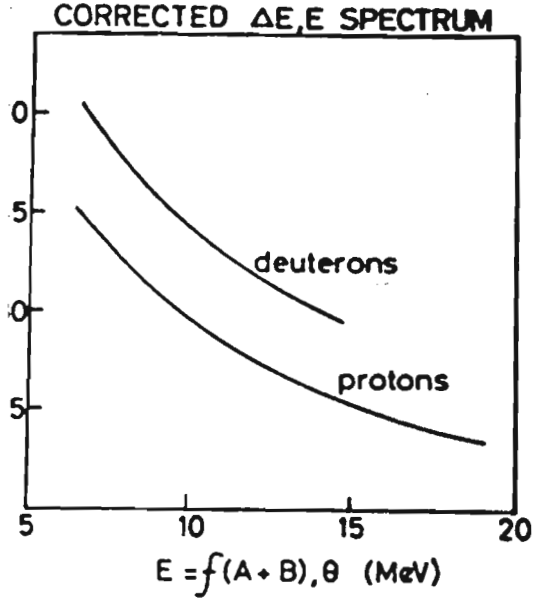

. 3.8 and Fig. 3.9 ΔE–E spectrum obtained from neutron collisions with ^{90}Zr–enriched foil. The proton locus is situated between a and c. The deuteron locus is above the line marked b. [Reproduced from ref.(1)].

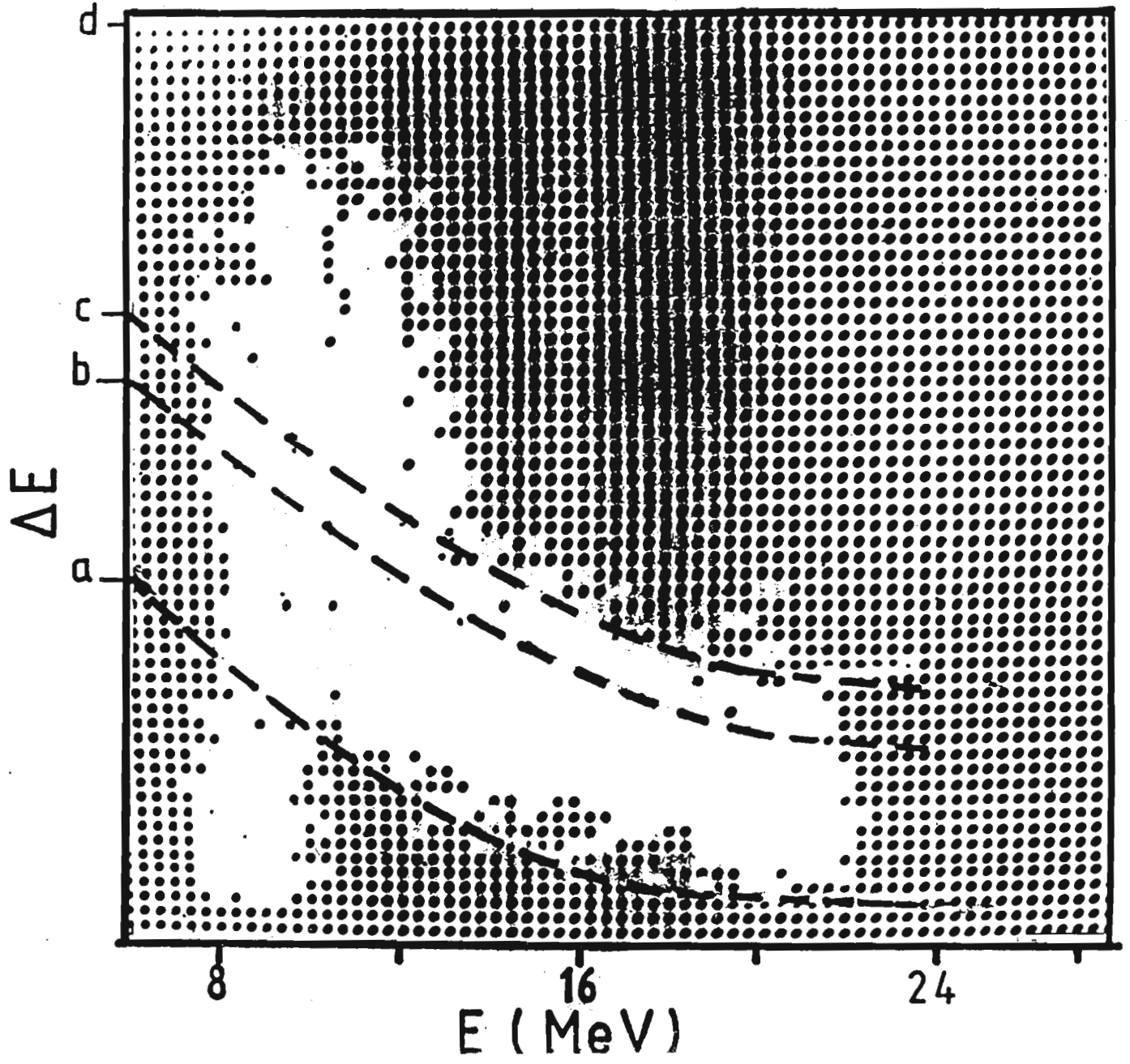

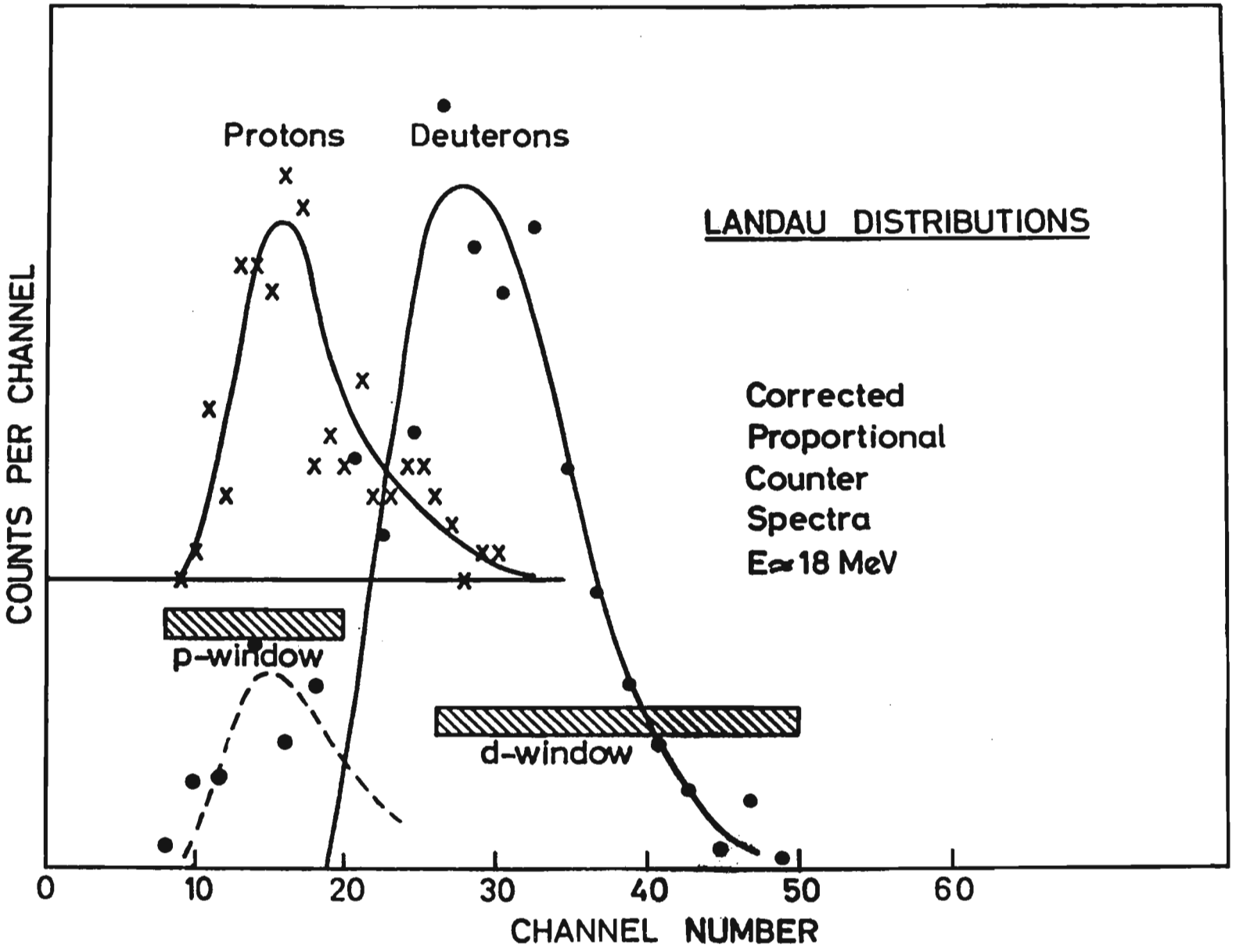

Fig. 3.10 Proportional counter spectra for monoenergetic protons and deuterons at 17 and 19 MeV respectively. Demonstrates the overlap in the Landau distributions. [Reproduced from Ref.(1)].

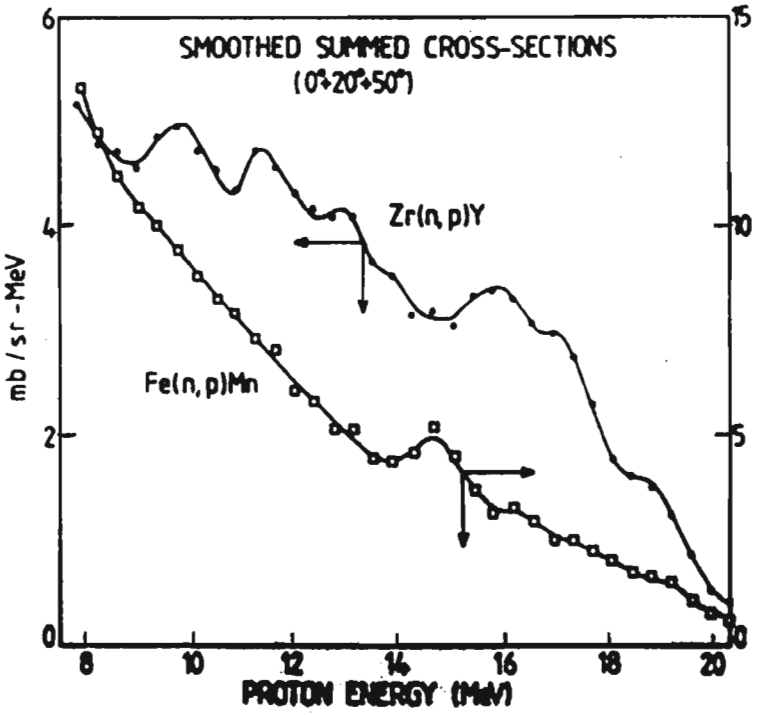

Fig. 3.11 Cross sections of the (n,p) reaction on zirconium and iron samples [Reproduced from Ref. (1)].

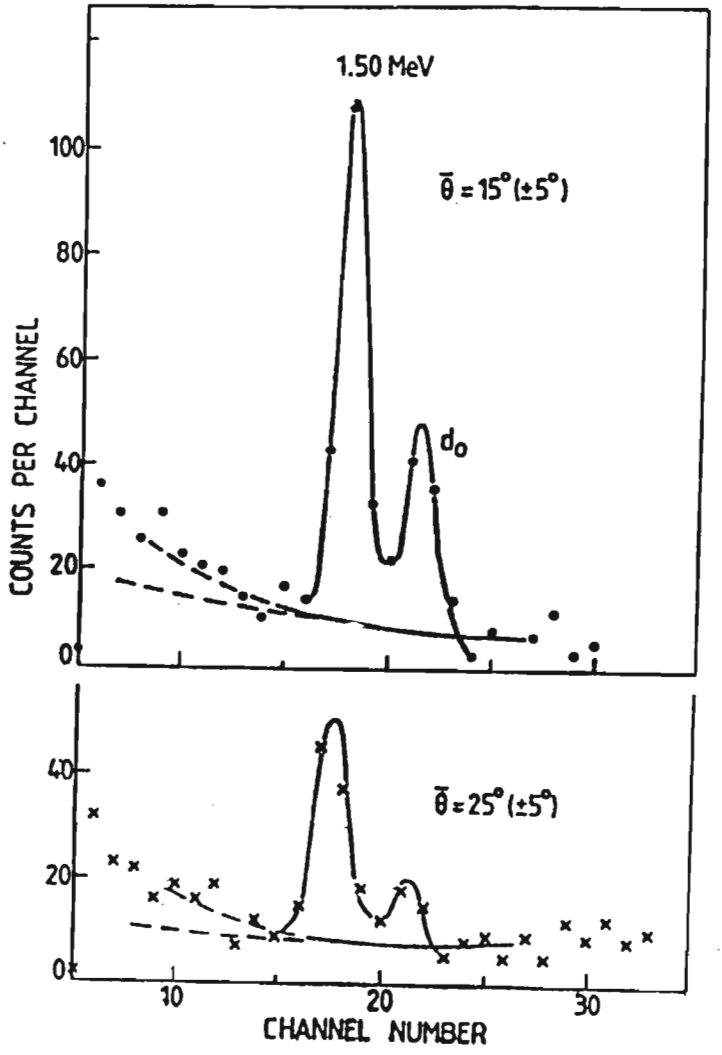

Fig. 3.12 Cross-sections of the (n,d) reactions

Additional corrections can be made to this angle calculation. These include zero offsets of A and B and slewing of the A and B amplitudes. The plots on figure (3.13) are from reference (1) and are the result of a much more detailed study. The data in table (3.1) is the result of a more recent run with only three sets of data points and figure (3.14) demonstrates the near-linearity of (A-B)/(A+B) with position.

Thus the detector system allows the simultaneous accumulation of data over an angular range of 80°. The angular resolution depends on the position resolution - checked above - and the geometry of the system (see later). The position resolution is demonstrated by placing a set of slits in front of the scintillator and then accumulating data. The slits correspond to the angles $\pm 7.5°$, $\pm 17.5°$, and $\pm 27.5°$. The spectrum in figure (3.15) shows proton events obtained from the (n,p) reaction on the p-poly sample at three average proton energies (21 MeV, 17 MeV, and 13 MeV) with the slits in position in front of the scintillator. The position resolution obtained in this manner corresponds to an angular resolution of less than 3° (FWHM).

3.2.6 Energy determination in the scintillator.

The energy determination of a detected particle depends on the stopping of the particle in the scintillator. As has already been mentioned, the thickness of the present scintillator may be reduced to improve the energy resolution, for the deuteron and proton energy range of interest.

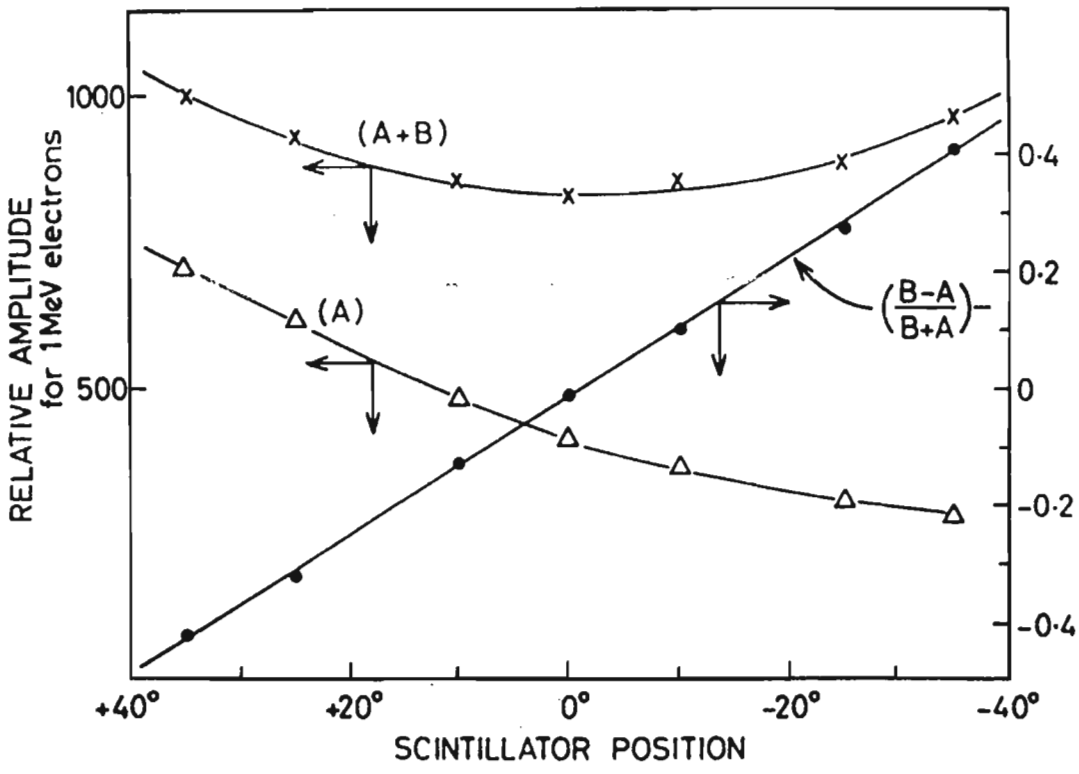

Fig. 3.13 Angle calibration of the scintillator using monoenergetic internal conversion electrons emitted from a ^{207}Bi source. [Reproduced from Ref.(1)].

	+35°	0°	-35°
	Channel Number	Channel Number	Channel Number
Scint A	350	205	165
Scint B	162	210	358
A+B	512	415	529
(A-B)(A+B)	0,367	-0.012	-0,369
Calibration factor: $= \frac{70 \text{ degrees}}{0.736} = 95.1$			

TABLE 3:1 Calibration of Scintillator Position dependence using ^{207}Bi, which is a 1 MeV internal conversion electron source (~ 3 MeV protons).

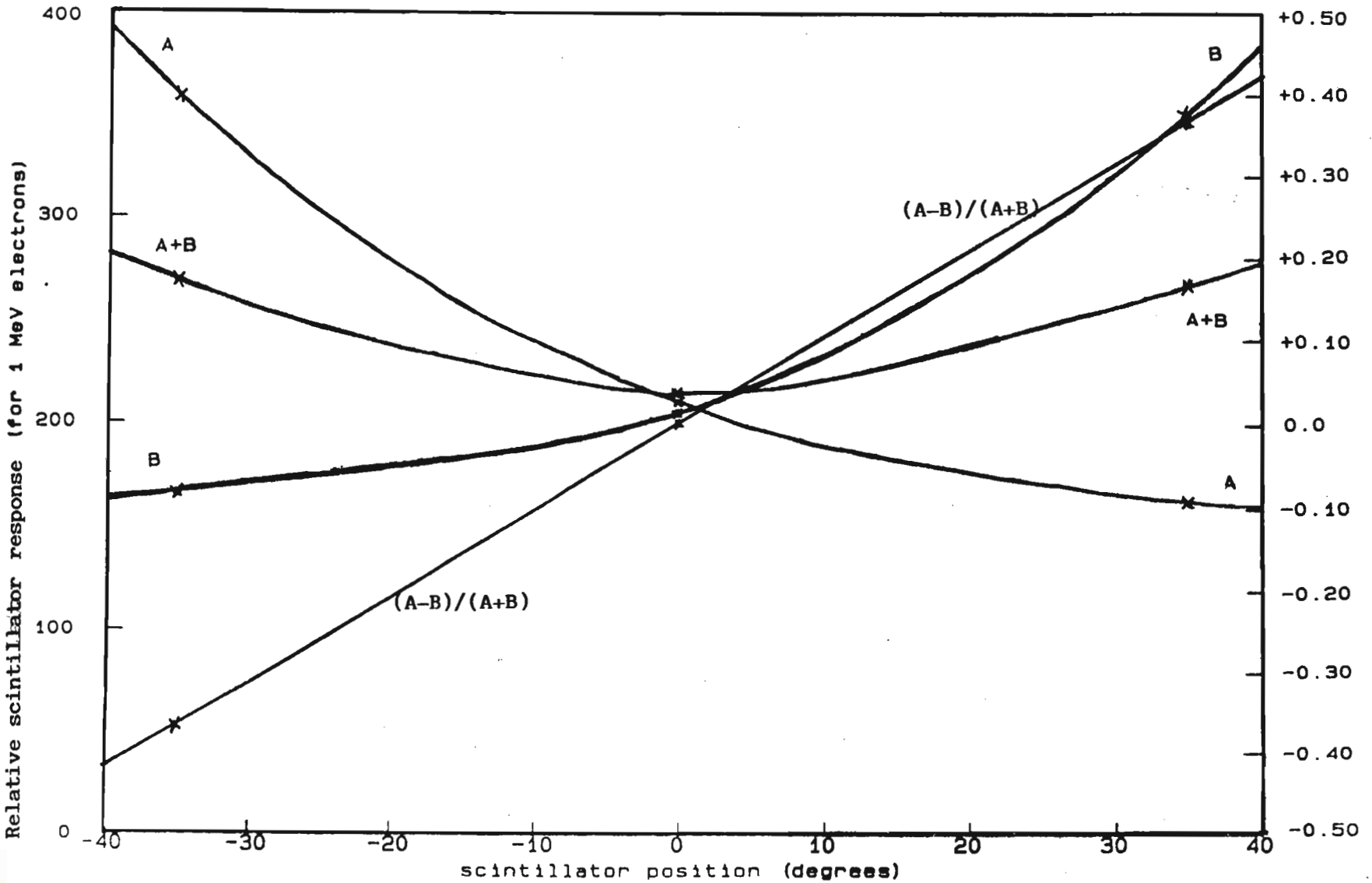

Fig. 3.14 Angle calibration of the scintillator using monoenergetic internal conversion electrons emitted from ^{207}Bi source. [Based on the limited data in Table (3.1) and normalized to the results of Refs(1) and (2).]

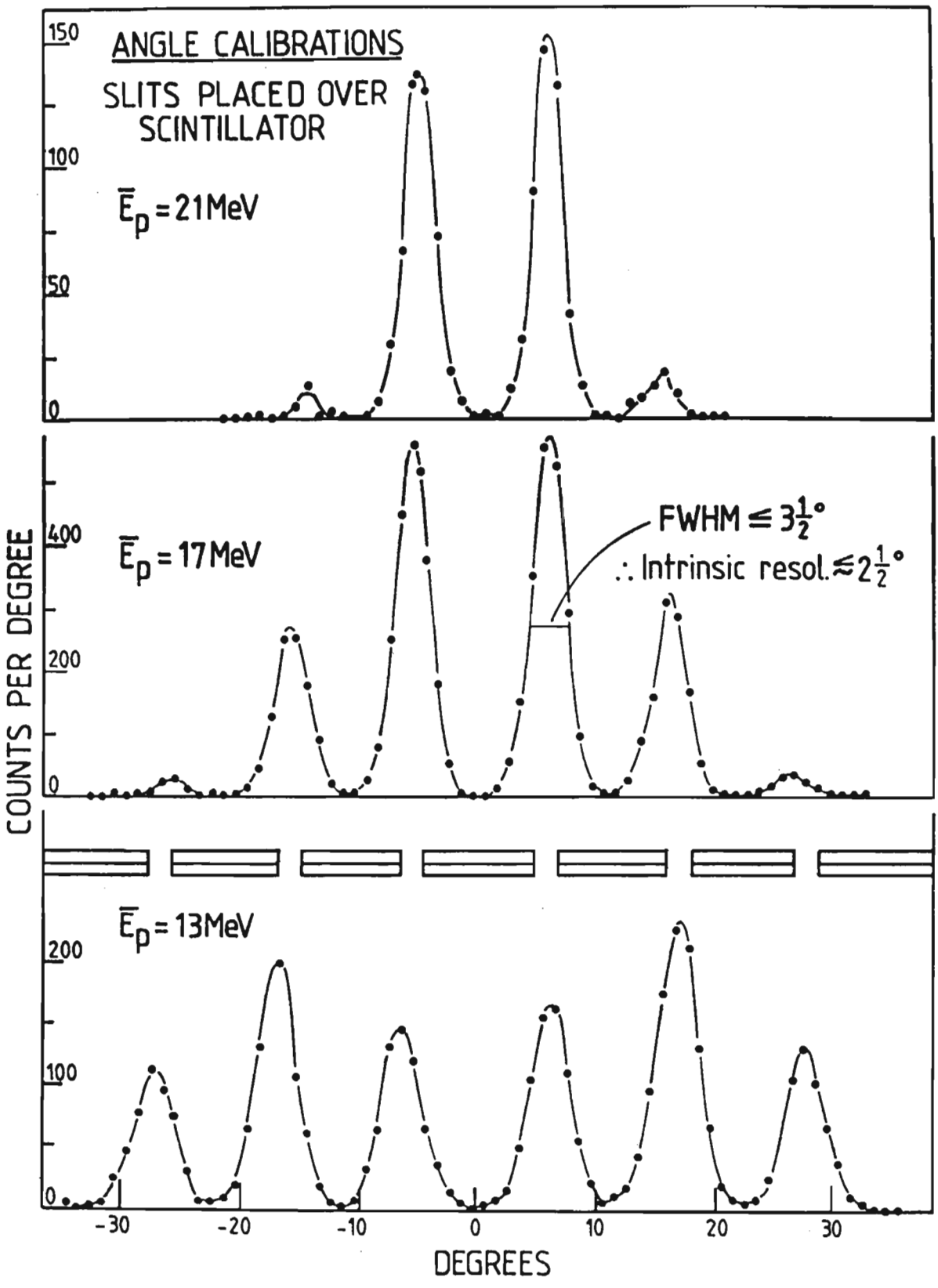

Fig. 3.15 Determination of the position resolution of the spectrometer by observing the sensitivity to slits placed in the path of protons produced in the (n,p) reaction on a p-poly sample. Performed for

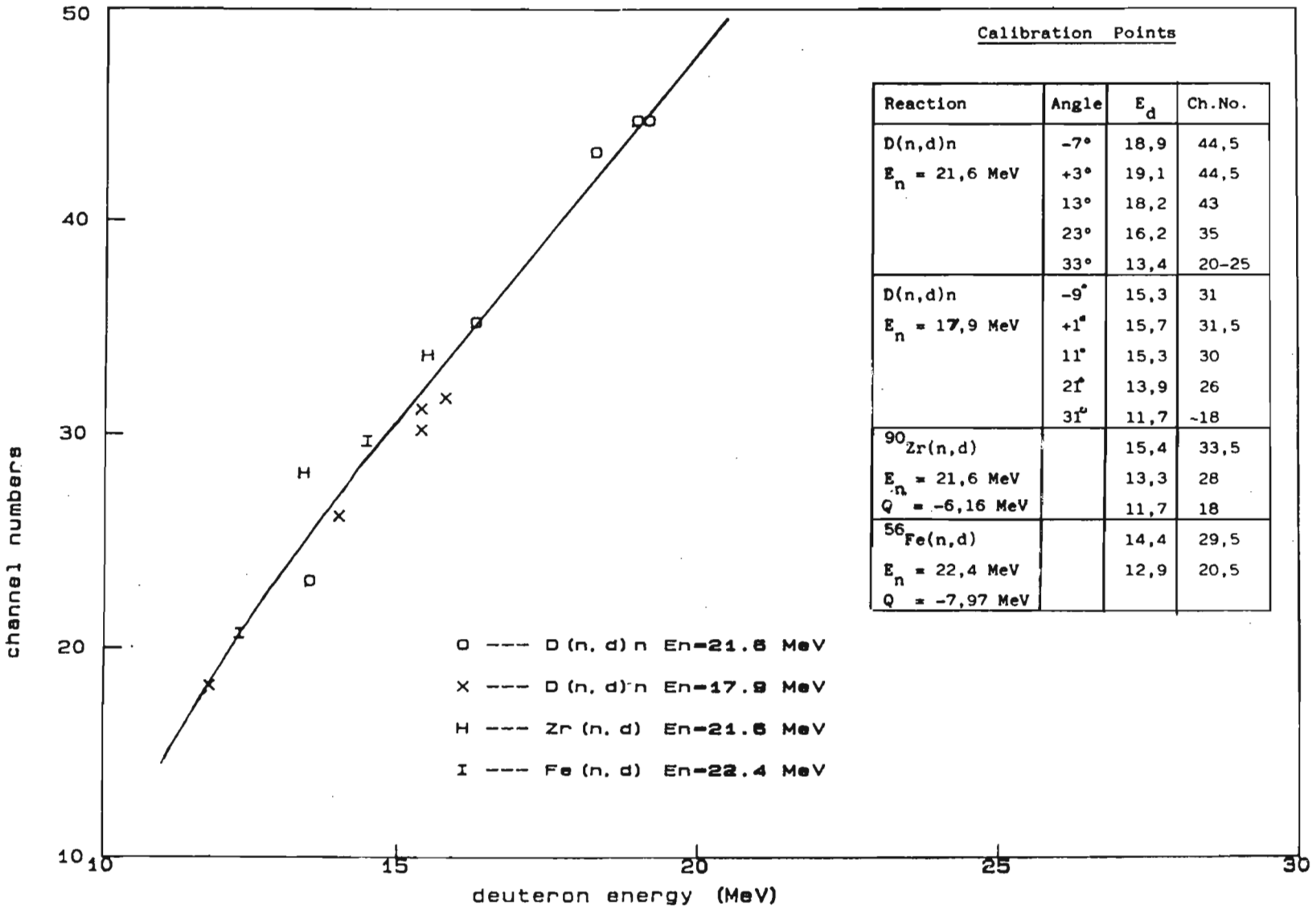

Calibration Points

Reaction	Angle	E_d	Ch.No.
D(n,d)n	-7°	18,9	44,5
E_n = 21,6 MeV	+3°	19,1	44,5
	13°	18,2	43
	23°	16,2	35
	33°	13,4	20-25
D(n,d)n	-9°	15,3	31
E_n = 17,9 MeV	+1°	15,7	31,5
	11°	15,3	30
	21°	13,9	26
	31°	11,7	~18
^{90}Zr(n,d)		15,4	33,5
E_n = 21,6 MeV		13,3	28
Q = -6,16 MeV		11,7	18
^{56}Fe(n,d)		14,4	29,5
E_n = 22,4 MeV		12,9	20,5
Q = -7,97 MeV			

Fig. 3.16 Deuteron energy calibration (based on data collected by K. Bharuth-Ram and W.R. McMurray)

The energy of the particles are obtained by summing the outputs of the A and B photomultipliers and is then corrected for angle-related effects by the program PAID4.

The energy scales have to be calibrated and this is performed with proton and deuteron spectra from the H(n,p) and D(n,d) reactions respectively on p-poly and d-poly samples. A deuteron energy calibration curve is shown in figure (3.16).

To obtain a measure of the energy resolution of the spectrometer, proton and deuteron spectra from the H(n,p) and D(n,d) reactions were obtained, for a scattering angle of zero degress, from a multiparameter dump with particle identification and angle selection. Kinematic calculations give an accurate value for the energy of these monoenergetic protons and deuterons. The energy resolution emerged as being of the order of 0.6 MeV (FWHM).

3.2.7 In conclusion

The functioning of the proportional counters and scintillators were checked at regular intervals during a run by checking the peak positions of A and B (with the ^{207}Bi source at 0°) and of PC1, PC2, and A/Co (with the Am-Mo source placed on the A/Co side of the sandwich). A further check that was performed with the same frequency, was with a deuterated perspex sample placed on the A/Co side of the sandwich. This data was collected in 3-coincidence mode and the PC1(A+B) and PC2(A+B) spectra (which were available immediately on the video monitor of the data acquisition computer) allowed a check of the deuteron locus as well as the functioning of the proportional counters and scintillator and the electronics.

The spectrometer has been used for the study of the reactions listed below:

$^{90}Zr(n,d)^{89}Y$ and $^{90}Zr(n,p)^{90}Y$

$^{27}A\ell(n,d)^{26}Mg$ and $^{27}A\ell(n,p)^{27}Mg$

and $^{56}Fe(n,d)^{55}Mn$ and $^{56}Fe(n,p)^{56}Mn$

In these reactions the spectrometer offers the following:

(i) efficient particle identification

(ii) background suppression

(iii) an acceptable energy resolution

(iv) an acceptable angular resolution

and (v) simultaneous accumulation of data over an angular range of 80°, which allows for acceptable beam times for the study of low yield (n,d) reactions.

3.3 The solid angle (or geometry) corrections

The spectrometer has a built-in geometry which adversely affects its allocation of angular position to events and its angular resolution. It is necessary for the analysis and design of experiments performed with the spectrometer to determine the effect of the geometry on the angle determination and resolution of the spectrometer.

3.3.1 The geometry

The accelerated deuteron beam (at 5.25 MeV) has a cross-sectional diameter of 4 mm[5]. It is directed into the tritium gas cell which is 30 mm long and has a diameter of 10 mm.

21.8 MeV neutrons are produced all along the deuteron beam within the cell, and in all directions. The target is sandwiched between the first (A/Co) and second (PC1) proportional counters. It is a foil and is assumed to be two-dimensional. The distance, d between the target and the forward face of the gas cell has been set at the values of d=60 mm and d=120 mm for calculational purposes.

The neutrons that collide into the target have their source in the 4 mm diameter deuteron beam, and depending on the size of the target and the value of d these neutrons arrive at the target in a range of angles about the axis of symmetry. Considering a target of width 10 mm and height 12 mm, and d=60 mm, the largest neutron angle is ≈8°. For d=120 mm this angle reduces to ≈4°. (See figure (3.17)).

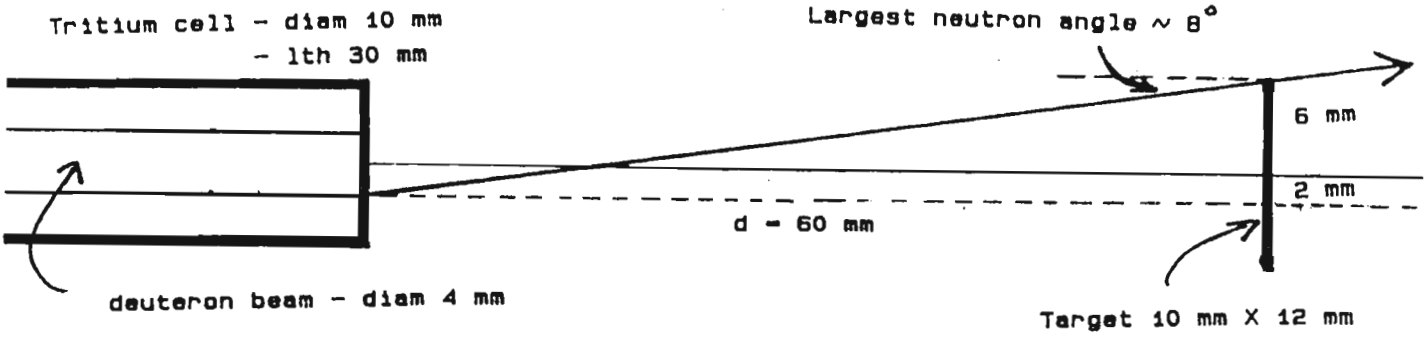

Fig. 3.17 The neutron source - target geometry. Determination of the angular range of impinging neutrons on the target.

The finite dimensions scintillator is the major source of error in the angle determination of the spectrometer. There are two sources:

(i) The scintillator has a radius of curvature of 200 mm. The target is located at the centre of the plastic arc and is therefore 200 mm from the scintillator. Consider a "largest angle" neutron that picks-up a proton from a ^{90}Zr nucleus located at the top edge of the target. If it is a zero-degree deflected deuteron it arrives at the scintillator at a position $\approx$35 mm from the axis of symmetry of the system, in which the target is located at d=60 mm from the gas cell. (See figure (3.18)). If the target is located at d=120 mm then this excursion from the axis of symmetry is $\approx$16 mm.

(ii) The scintillator has a width of 50 mm. If a strip of the scintillator corresponding to a nominal angle of 0° plus-or-minus 2.5° is considered it will be observed that the angular contributions to this strip occur in the range 0° to 8° (see figure (3.19)) for an angle of incidence of zero degrees at the axis of symmetry. This means that what was meant to be a $0° \pm 2.5°$ strip collects cross-section contributions from an angular range of 0° to 8°. Of course, this is a very conservative estimate since the case considered is the most symmetrical one. Table (3.2) shows the actual range of angular contributions to each of these scintillator strips.

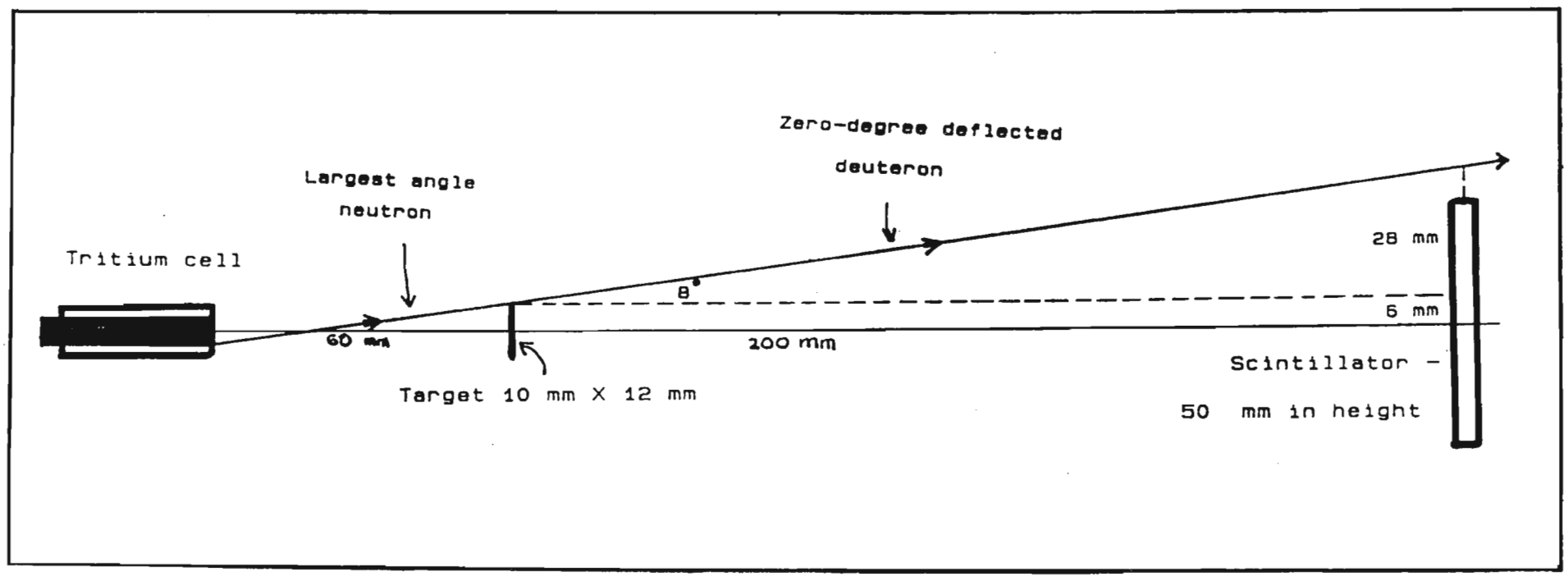

Fig. 3.18 The neutron source – target – scintillator geometry.

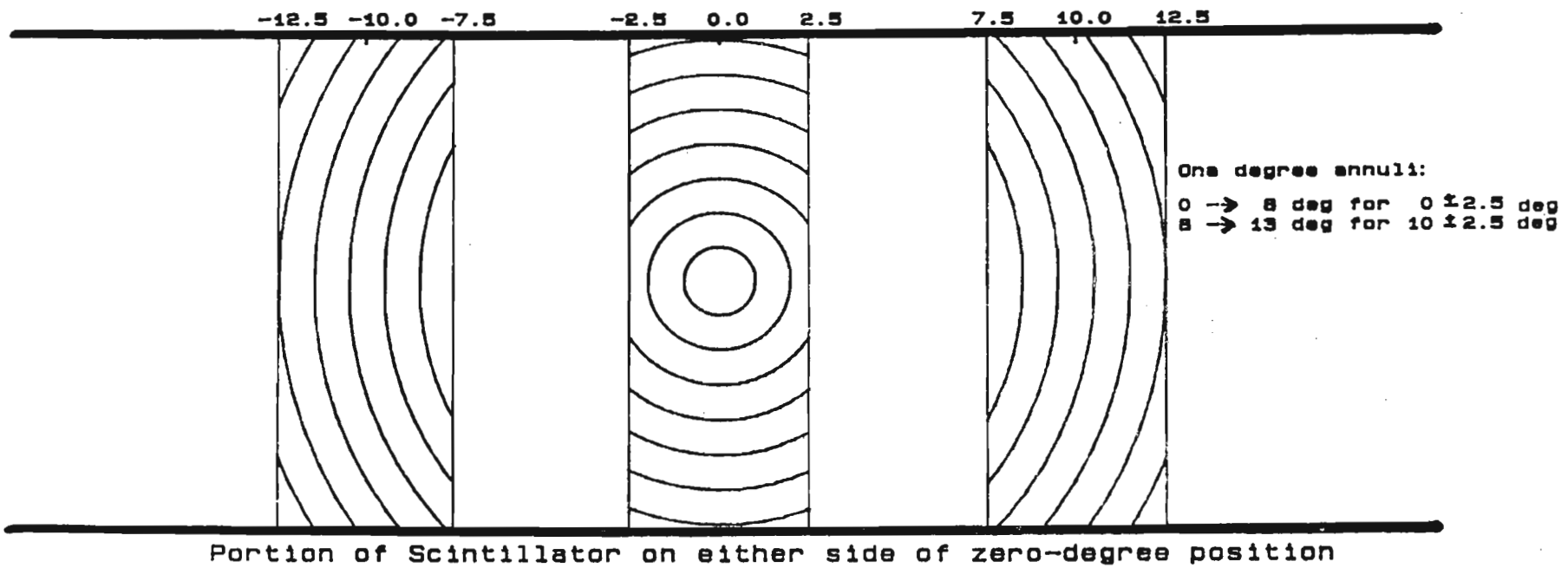

Fig. 3.19 The effect of the scintillator height (= 50 mm) on the assignment of mean angular positions to the scintillator.

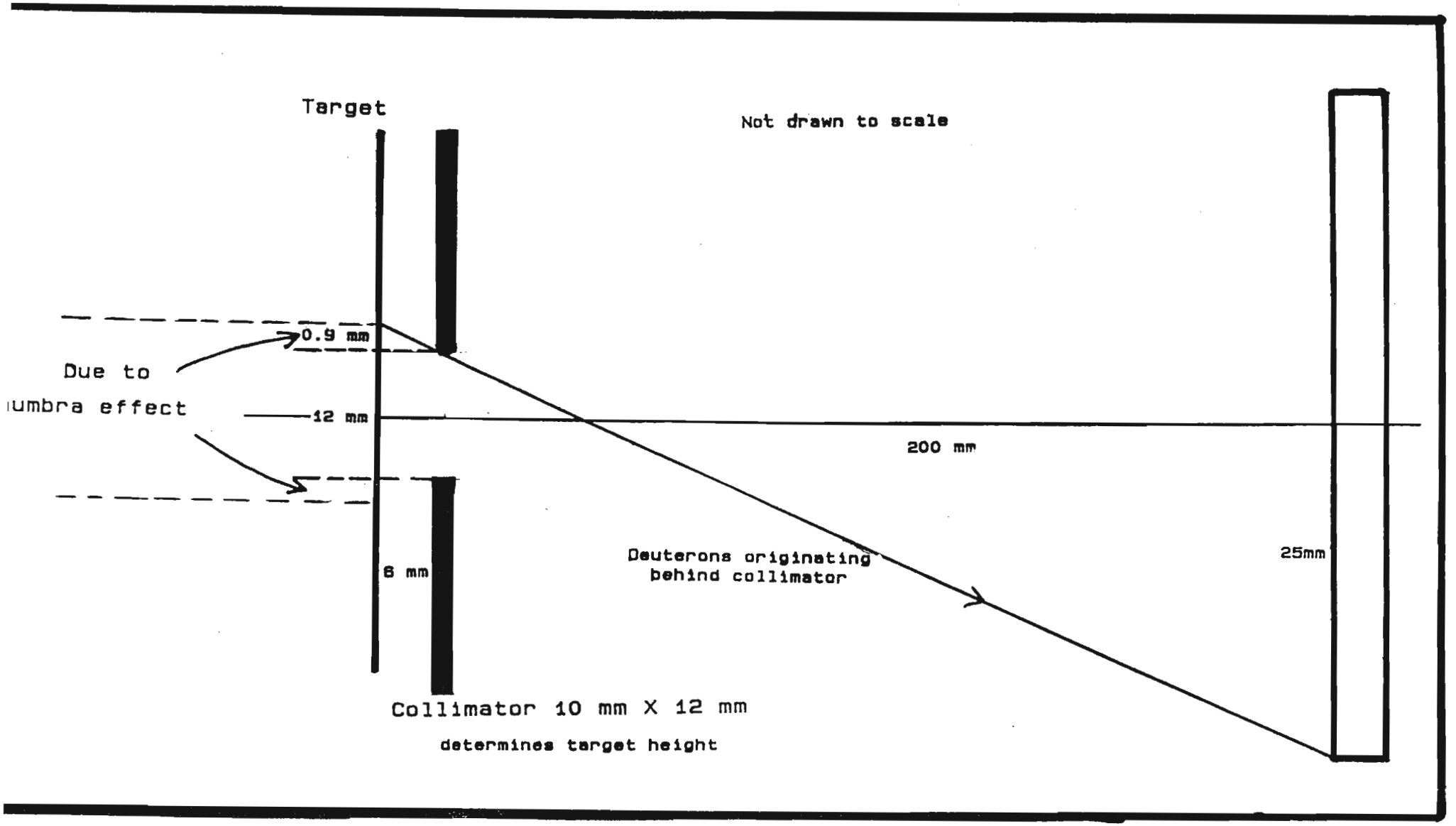

. 3.20 The Penumbra effect - due to the displacement of the collimator relative to the target.

One last effect was considered. The position of the collimator between PC1 and PC2 places it at a distance of 6 mm from the target. Figure (3.20) demonstrates a penumbra effect, which calculations have shown to be negligible. The penumbra effect effectively increases the height of the target but permits cross-section contributions from the additional target area in a very limited sense.

	Nominal Angle	Angle Limit	Angular Range on Scintillator	Mean Scattering Angle	New Angle Limit (FWHM)
d = 60 mm	2,5°	± 2,5°	0,0° - 17,0°	6,0°	± 4,0
	7,5°		0,0° - 20,5°	9,0°	± 4,2°
	12,5°		3,5° - 24,5°	13,5°	± 4,4°
	17,5°		8,5° - 29,0°	18,2°	± 4,4°
	22,5°		13,5° - 33,5°	23,1°	± 4,5°
	27,5°		18,5° - 38,5°	28,0°	± 4,5°
	35,0°		26,0° - 45,5°	35,4°	± 4,5°
	50,0°		41,0° - 60,0°	50,3°	± 4,5°
d = 120 mm	2,5°	± 2,5°	0,0° - 14,0°	5,4°	± 3,6°
	7,5°		0,5° - 17,5°	9,1°	± 3,6°
	12,5°		5,5° - 22,0°	13,3°	± 3,6°
	17,5°		10,5° - 26,5°	18,1°	± 3,7°
	22,5°		15,5° - 30,5°	23,0°	± 3,7°
	27,5°		20,5° - 36,0°	27,9°	± 3,7°
	35,0°		28,0° - 43,0°	35,3°	± 3,7°

TABLE 3.2 **Results of the calculation of mean scattering angles and new angle limits (FWHM) for ± 2,5° scintillator strips.**

The calculations were performed on an IBM Personal Computer. Two programs were developed : one for a purely digital calculation and a second for a semi-analytical calculation.

The latter was found to be cost effective but the first was run from time to time to check on the semi-analytical calculations. The correspondence between the calculations was at all times perfect. The calculations were performed in three stages:

(i) The tritium cell is 30 mm long and has a diameter of 10 mm. The deuteron beam has a diameter of 4 mm[5] and since the 21.8 MeV neutrons are produced in this beam, the neutron source is the extended cylinder of diameter 4 mm and length 30 mm. This source is digitized into 1 mm^3 boxes. The two-dimensional target has a 1 mm x 1 mm grid imposed upon it and a neutron source centroid is calculated based on the following. Each grid-cube produces neutrons in solid-angle cones that may or may not strike the target. The frequency of neutron impingements ($f(r_i)$) for each grid-volume of the neutron source (coordinates r_i) is stored together with the coordinates of the grid-volume. The centroid is calculated with the expression

$$\langle r_i \rangle = [\Sigma\ f(r_i)\ r_i] / [\Sigma\ r_i]$$

where both sums are over the number of neutron source grid-cubes. The x and y coordinates (see figure (3.21)) of this centroid lie on the axis of symmetry while $\langle z \rangle \approx 14$ mm from the window of the cell for the d=60 mm case and $\langle z \rangle \approx 15$ mm for the d=120 mm case. For the rest of the calculation, the neutron source was assumed to be a point source located at the centroid of the cell.

(ii) The only neutrons of interest to the study are those that impinge on the target. (A long counter is set up throughout the experiment, however, to monitor the neutron production in the gas cell). The next step was to store on computer diskette the positions on or off the scintillator of the zero degree deflected "deuterons" for each impingement on the target. This calculation required the angle of incidence of each "neutron" on the target which varied from 0° to ≈ 8° for the d=60 mm case and from 0° to ≈ 4° for the d=120 mm case.

As the last part of the calculation requires the zero degree deflection positions on the scintillator each time it is run, this proved to be time and cost effective.

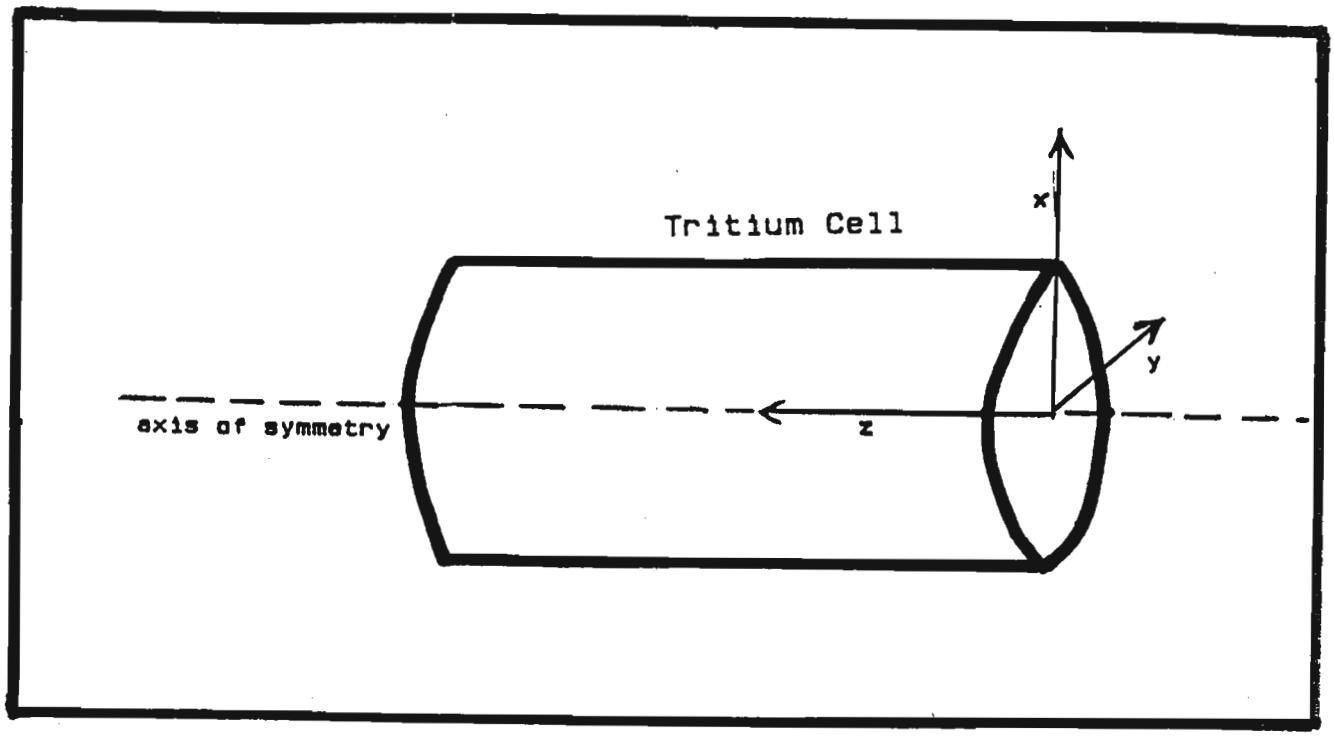

Fig. 3.21 The coordinate system employed in the calculation of the cell controid.

(iii) These correction calculations involve the determination of the relative area contributions of half-degree annuli around each of the zero degree deflection points, to particular strips of the scintillator - the typical strips corresponding to the nominal angles of 2.5°, 7.5°, 12.5°, 17.5°, 22.5°, 27.5°, 35.0°, and 50.0° plus or minus 2.5°. Table (3.2) shows the angular range of the annuli that contribute to each of these scintillator strips (for the d=60 mm case). The information to reallocate mean angular representations to the scintillator strips was available and performed with the expression

$$\langle\theta\rangle = [\Sigma A(\theta).\ \theta] \ / \ [\Sigma\theta]$$

where both sums run over the angular range of the annuli that contributed to a particular strip and $A(\theta)$ is the area contribution of the annulus centred on θ. These new mean scattering angles (for the d=60 mm case) corresponding to the original nominal angles are shown in table (3.2) with the new angle limits which are taken at FWHM. The same calculation for the d=60 mm case is performed for nominal angles of 5.0°, 15.0°. 25.0°, and 35.0° with angle limits of plus or minus 5°. The results for this calculation are given in table (3.3).

	Nominal Angle	Angle Limit	Angular Range on Scintillator	Mean Scattering Angle	New Angle Limit (FWHM)
d = 60 mm	5,0°	± 5,0°	0,0° - 20,5°	7,5°	± 4,7°
	15,0°	± 5,0°	3,5° - 29,0°	15,9°	± 5,4°
	25,0°	± 5,0°	13,5° - 38,5°	25,5°	± 5,5°
	35,0°	± 3,0°	25,5° - 46,0°	35,4°	± 4,7°

TABLE 3.3 Results of the calculation of mean scattering angles and new angle limits (FWHM) for the stated scintillator strips.

In the low yield experiments studied with this spectrometer, it is advantageous for statistical reasons to choose the latter set of nominal angles with an angle limit of plus or minus 5°. However, there are two major drawbacks with this. The first one concerns the fact that the angular resolution is decreased by approximately 25% and in an experiment in which the energy resolution is of the order of 0.6 MeV, this places a premium on the efficiency of the system. The second drawback hinges on the fact that the system allows for the simultaneous accumulation of data over an angular range of $\approx 80°$. However, to improve the statistics of an experiment the spectrometer is usually used in its most symmetrical form; that is, the midpoint of the scintillator is located on the accelerator beam line (or what has been referred to as the axis of symmetry). This reduces the angular range of the data accumulation from 80° to 40° - thus doubling-up the statistics. This means that for the second case (nominal angles 5° etc.) there are just four experimental cross section data points which are available to compare with the distorted-wave method calculations.

The former case provides seven such points which make the comparisons possible. The area - annuli angle curves are shown for both cases in figures (3.22) and (3.23) respectively. These curves indicate that there is considerable overlap between the contributions of successive nominal angles but there is sufficient resolution between peaks to recognize mean scattering angles.

The calculations were repeated for the d=120 mm case. Table (3.2) shows that doubling the distance between the tritium cell and the target improves the angular resolution of the spectrometer by approximately 10% and brings the mean scattering angle closer to the nominal angles. This improvement is significant but has to be balanced with the decrease of neutron flux which decreases by a factor of four by doubling the distance between the tritium cell and the zirconium target. In the low yield (n,d) reaction this consideration is important.

3.4 Results

The angle range of 0° to 50° was covered in two sets of measurements with different orientations of the spectrometer to the beam axis and different cross-section normalisation factors.

Deuteron spectra were generated for nominal scattering angles of 2.5°, 7.5°, 12.5°, 17.5°, 22.5°, 27.5°, 35.0°, and 50° with angle limits of plus or minus 2.5°. These spectra are shown in figure (3.24) with the background counts present. To subtract out the background, it is necessary to choose an acceptable background line and this is done for the 12.5° spectrum in figure (3.24). Figure (3.25) shows the modified 12.5° spectrum - the type of spectrum from which the cross-section integrals are taken. Table (3.4) shows the integrals for the peaks, which are identified for the time-being as d_o and $d_{\quad}$

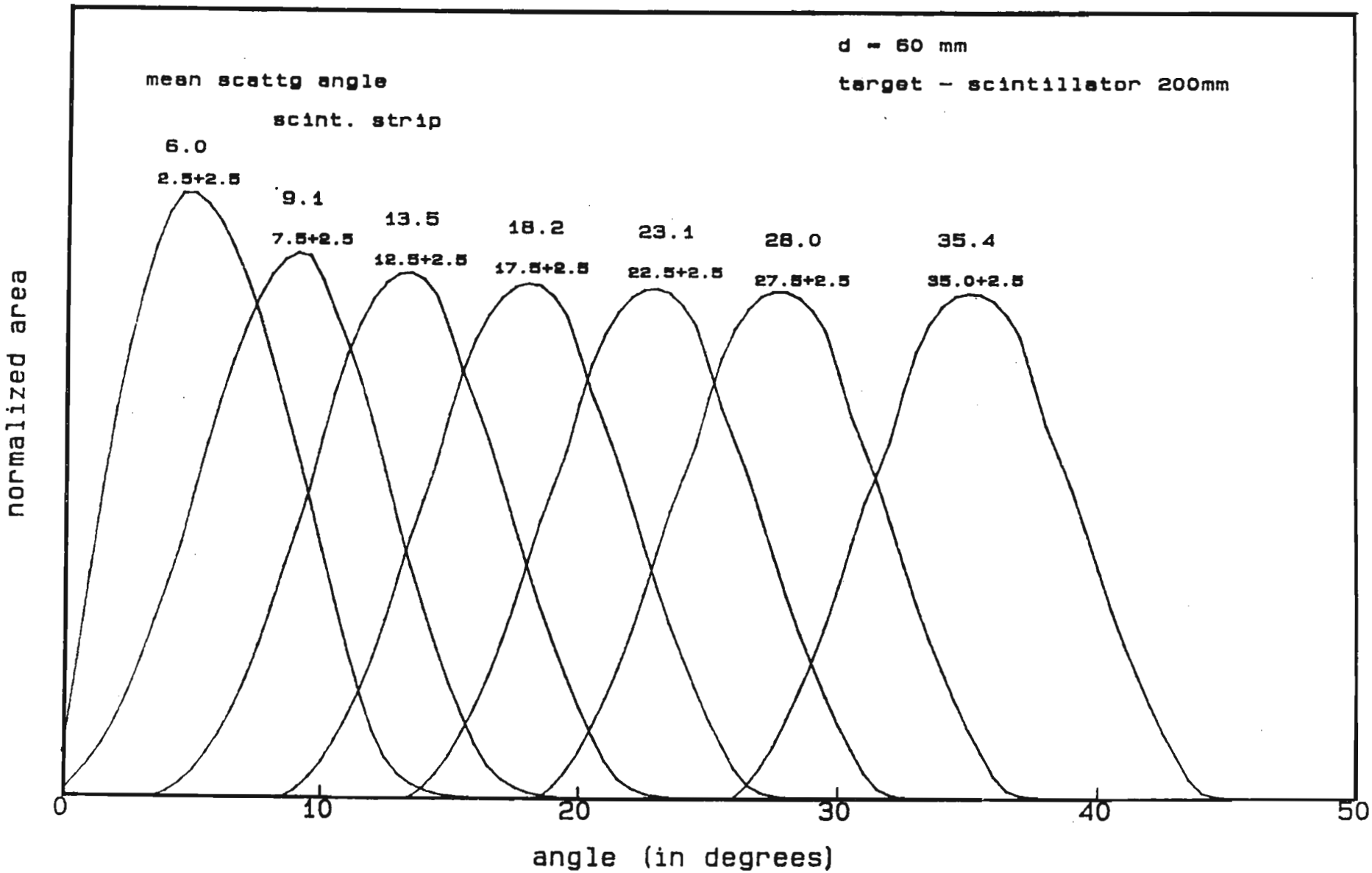

Fig. 3.22 Determination of the mean scattering angles and the angular resolution of the scintillator for the case d = 60 mm.

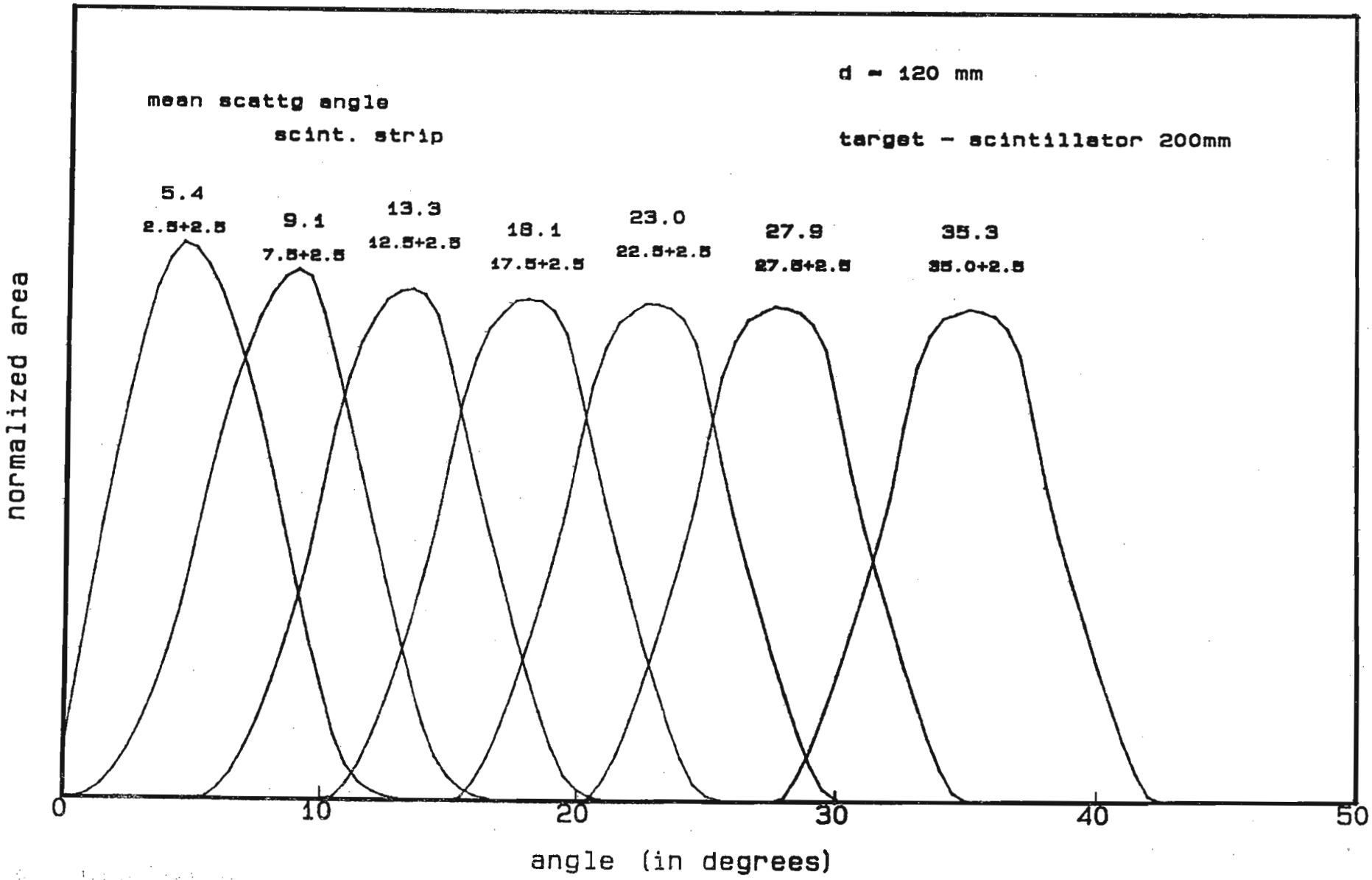

Fig. 3.23 Determ^{n} of mean scattering angles and the angular resolution of the scintillator for the case d = 120 mm.

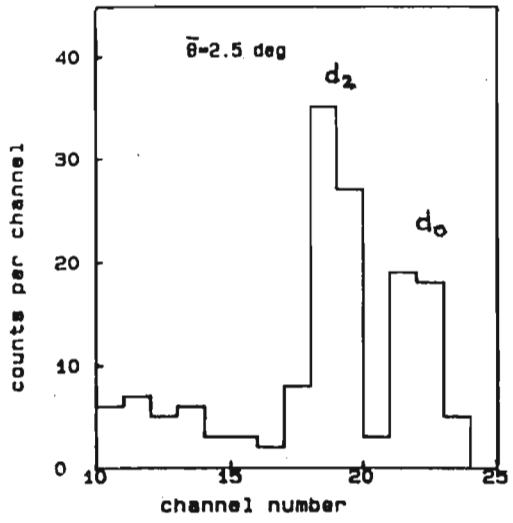
θ̄=2.5 deg
d₂
d₀
counts per channel
channel number
0
10
20
30
40
10
15
20
25

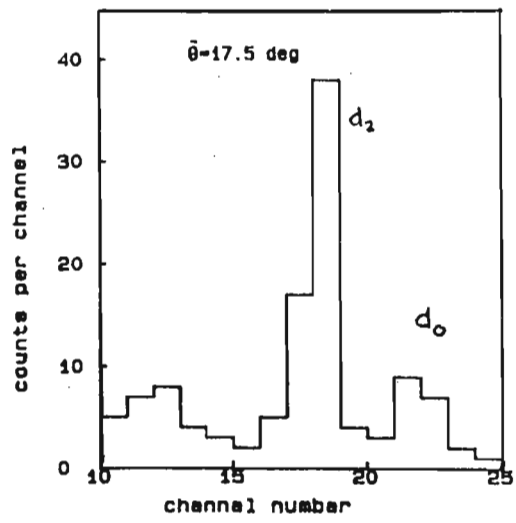
θ̄=17.5 deg
d₁
d₀
counts per channel
channel number
0
10
20
30
40
10
15
20
25

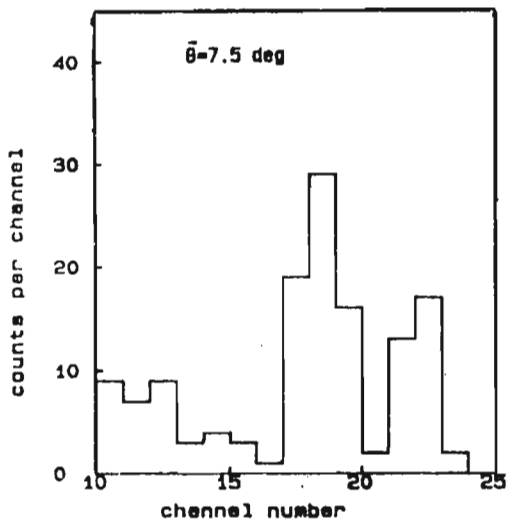
θ̄=7.5 deg
counts per channel
channel number
0
10
20
30
40
10
15
20
25

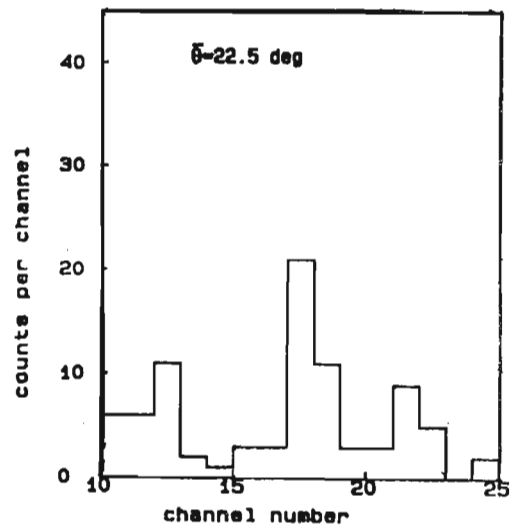
θ̄=22.5 deg
counts per channel
channel number
0
10
20
30
40
10
15
20
25

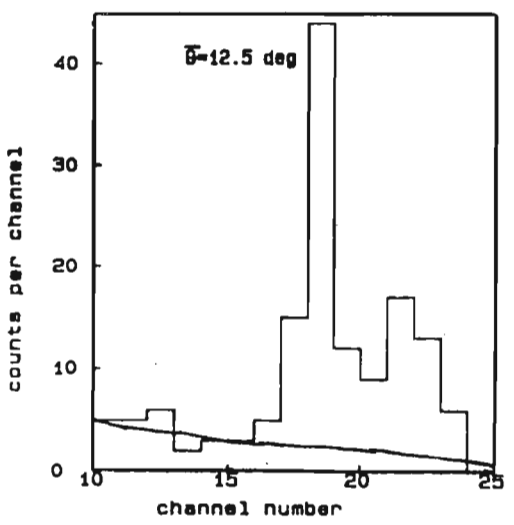
θ̄=12.5 deg
counts per channel
channel number
0
10
20
30
40
10
15
20
25

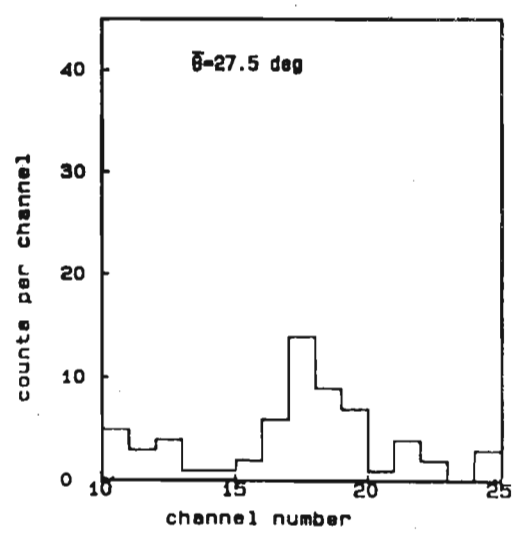
θ̄=27.5 deg
counts per channel
channel number
0
10
20
30
40
10
15
20
25

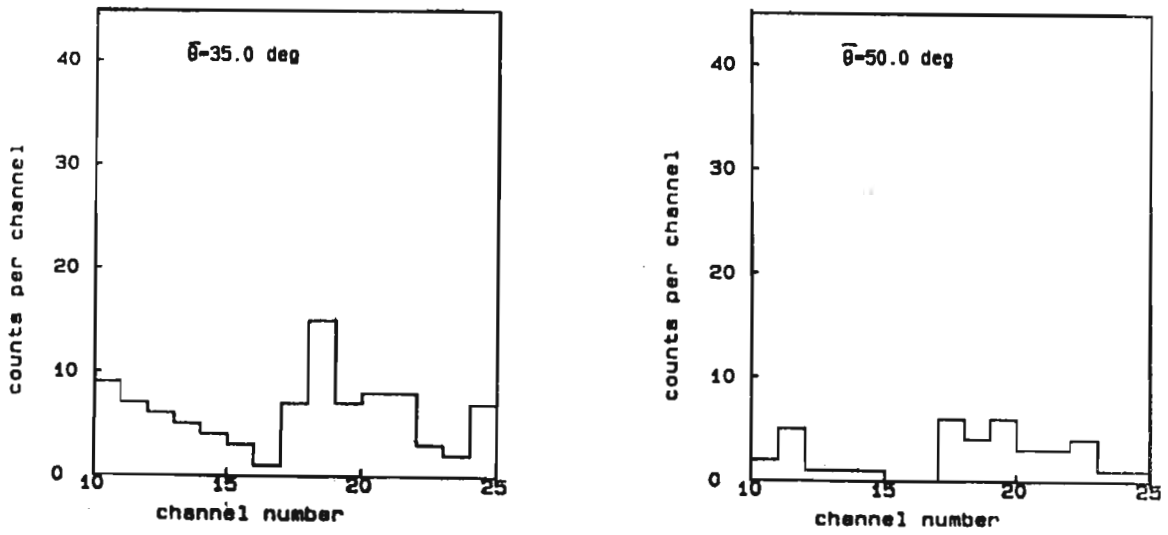

Fig. 3.24 Deuteron spectra generated for nominal angles $\bar{\theta} \pm 2.5°$.

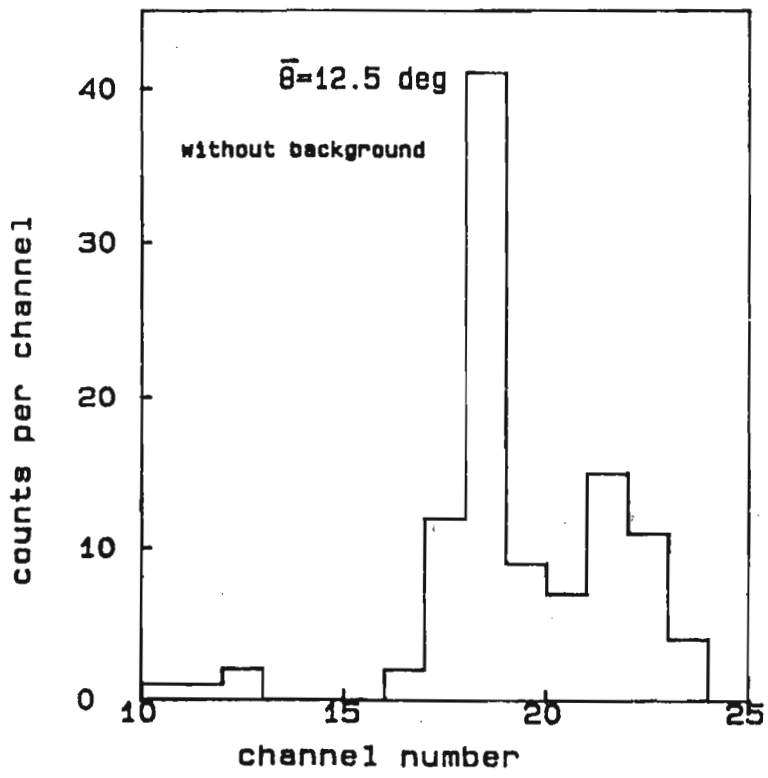

Fig. 3.25 Deuteron spectrum for $\bar{\theta} = 12{,}5°$.
The background counts are
subtracted out.

Nominal Angle ± 2,5°	d_o	d_2	
2,5°	36	68	x 0,15 mb/ster
7,5°	34	61	
12,5°	34	70	
17,5°	16	54	
22,5°	14	32	
27,5°	4	32	
35,0°	10	18	x 0,12 mb/ster
50,0°	6	11	

TABLE 3.4 **Angular distribution of the absolute cross sections of the (n,d) reaction on ^{90}Zr.**

REFERENCES

(1) W.R. McMurray and K. Bharuth-Ram, S.Afr. J. Phys. 8 (1985) 22.

(2) W.R. McMurray et al, SUNI Annual Research Report 55 (1978) 14.

(3) J. Soukup et al, Nucl. Instr. Meth. 141 (1977) 409.

(4) W.R. McMurray, K. Bharuth-Ram and S.M. Perez, Z. Phys. A315 (1984) 189.

(5) Personal communication with Dr W.R. McMurray.

Chapter Four

Distorted-wave method calculations and results

The experimental study of the $^{90}Zr(n,d)^{89}Y$ reaction cross-sections produced results with sufficient energy and angular resolution and statistics to permit a distorted-wave method analysis of the angular distribution of the reaction cross-sections. These calculations were performed with the code DWUCK4[1] on the CYBER 815 Computer at Council for Scientific and Industrial Research.

4.1 Description of the computer code DWUCK4.

DWUCK4 calculates the differential cross-section for a reaction using a very general form of the distorted-wave method, so as to be employable over a large range of reaction studies. These calculations are performed in the zero-range approximation with the local energy approximation being applied to correct for nonlocal and finite-range effects. Its inability to perform exact finite-range calculations restricts its usage. Knock-on and heavy-ion stripping and pick-up reactions have very large finite-range effects which have to be treated exactly. For these reactions it is necessary to turn to one of the other codes available, such as LOLA[2], which can treat the finite-range effects exactly.

The programme DWUCK4 computes the cross sections using the theory described in Chapter Two. The notation follows that of Austern[3] very closely, which is suitable for light-ion reactions.

(The notation adopted in Chapter Two follows that of Satchler[4] and Glendenning[5] which has more symmetry and provides a better picture for heavy-ion interactions. The calculated cross sections $\sigma^{\ell mj}$ (DW) have units of fm^2/ster (=10 mb/ster).

4.1.1 Optical model potential options available in the program

The optical potential options available in the program are the following:

(a) Volume Woods-Saxon potential

(b) Surface Woods-Saxon potential

(c) Spin-orbit potential

(d) Coulomb potential

(e) Second derivative Woods-Saxon potential

(f) Spin-orbit potential from a surface Woods-Saxon potential

(g) Volume Woods-Saxon potential X r^{power}

(h) Surface Woods-Saxon potential X r^{power}

(i) Normalized harmonic oscillator potential

(j) Gaussian shape potential X r^{power}

(k) Legendre expansions of the volume and surface Woods-Saxon potentials.

Finally, the program has the facility to accept an externally introduced potential. The first four listed above are used in this study and they have been described in Chapter Two. The choice of potentials in the calculations performed depends on the choice of potentials to describe the associated elastic scatterings. The rest of the potentials were not utilized or tried for the reason that they were not used to describe the elastic scatterings.

4.1.2 The finite-range correction factor

In a one-particle pick-up reaction, such as

$$a + A = a + (c + B) \rightarrow (a + c) + B = b + B$$

the overlap between a and b is described by the function

$$D(\underline{r}_{ca}) = (\mu_a \mid V_{ac}\mu_b)$$

where V_{ac} is the interaction $V_{ac}(r_{ca})$. This expression for the overlap occurs in the expression for the transition amplitude and represents a six-fold integration for a value of the transition amplitude. To reduce the integration to a two-dimensional integration, the zero-range approximation is used for the overlap. This involves the replacement of the function $D(\underline{r}_{ca})$ by a δ-function. This is feasible for light ion reactions[4] as D has a short range in this case. The overlap is then represented by

$$D(\underline{r}_{ca}) \approx D_o \delta(\underline{r}_{ca})$$

where D_o is called the overlap integral and is given by

$$D_o = \int D(\underline{r}_{ca}) d\underline{r}_{ca}.$$

For the (n,d) reaction, the overlap integral is evaluated to be 1.55×10^4 MeV^2 fm^3 [6]. This approximation greatly simplifies the calculation of the distorted-wave method transition amplitude but at the cost of an overestimation of the contribution of the nuclear interior to the transition amplitude. This is countered by making a finite-range correction, made within the local energy approximation[3][4][5] (LEA), in which a simple, nearly equivalent, "local" potential replaces the nonlocal potential.

The wavefunctions $\varepsilon^{(L)}$ for this local potential are related to those of the nonlocal potential by the relationship

$$\varepsilon^{(NL)}(\underline{r}) = F(\underline{r}) \quad \varepsilon^{(L)}(\underline{r})$$

where $F \to 1$ as $r \to \infty$ for the scattering waves. The first-order correction factor from the LEA for the zero-range approximation in the overlap multiplies the form factor

$$\langle bB \mid V \mid aA \rangle$$

The program requires the input of a finite-range correction parameter which is calculated by taking the derivative of the Fourier transform of the overlap at zero momentum and then dividing by the transform[4]. For the (n,d) reaction, this parameter is quoted as being between 0.621 and 0.695[1].

4.1.3 The nonlocal correction factor

The use of an equivalent local potential introduces an element of error in the calculation of the transition amplitude. A nonlocal correction is introduced which multiplies the form factor. The form of the correction is

$$W_{NL}(r) = \exp[2 \beta_i^2 m_i V_i(r) / 8h^2]$$

for each of the particles. The V_i are the local potentials, and the β's are the nonlocal parameters. They are usually quoted as 0.85 for nucleons and 0.54 for the deuterons[1].

In general, the program is user-friendly and has many run-time saving devices. The results of the calculations are presented in the next section.

4.2 The optical potential and the optical potential parameters

The choice of optical potential in this analysis depended on the potentials used in the description of the allied elastic scattering data. However, this choice is identical to the choices made by many authors in the analysis of similar reactions [7][8][9][10][11].

All distorted-wave method studies of single-nucleon stripping and pick-up reactions since 1943 that have been consulted have adopted the following optical model potential.

$$V = -V_R f(x_R) - iWf(x_w) + 4iW_D(d/dx_D)f(x_D)$$

$$-(\hbar/m_\pi c)^2 \; V_{so}(\underline{L}.\underline{\sigma})r^{-1}(d/dr)f(x_{so}) + V_c$$

where $f(x_i) = [1 + \exp(x_i)]^{-1}$ and the $x_i = (r - r_i A^{1/3})/a_i$.

The terms are all defined in the section on optical potentials in Chapter 2. The Coulomb potential is approximated by a potential due to a uniformly charged sphere of radius $r_c A^{1/3}$.

A search for optical potential parameters that describe the elastic scattering of neutrons on ^{90}Zr at an incident energy in the region of 21.6 MeV was unsuccessful. Some analysis of elastic scattering of protons on ^{90}Zr at $\approx$ 40 MeV[12] and at $\approx$ 21 MeV[13] is available. An examination of global parameter sets for similar[14] nuclei and at similar energies indicates that the parameters for protons and neutrons have quite different values. Hence it was decided to rely on global parameter sets for the neutron optical potential.

After some experimentation with different parameter sets[15][16][17], the set of Becchetti and Greenlees[14] proved to provide the best fit. This set of parameters is for nucleons with A>40 and for elastic scattering in which the bombarding energy <50 MeV. The parameters have the following form for the neutron potential:

$$V_R = 56.3 - 0.32E - 24.0(N-Z)/A \text{ MeV}$$

$$r_R = 1.17 \text{ fm}$$

$$a_R = 0.75 \text{ fm}$$

$$W = 0.22E - 1.56, \text{ or zero MeV (whichever is greater)}$$

$$W_D = 13.0 - 0.25E - 12.0(N-Z)/A \text{ MeV}$$

$$r_w = r_D = 1.26 \text{ fm}$$

$$a_w = a_D = 0.58 \text{ fm}$$

$$r_c = 1.30 \text{ fm}$$

$$V_{so} = 6.2 \text{ MeV}$$

$$r_{so} = 1.01 \text{ fm}$$

$$a_{so} = 0.75 \text{ fm}$$

where E is the incident neutron energy in MeV. The parameter values for E=21.6 MeV are given in table (4.1).

For the deuteron parameters a similar search was carried out for the elastic scattering of deuterons on ^{89}Y at an energy of 13-16 MeV, which is the deuteron energy region of interest in this experiment. Failure to find such data necessitated the use of a global parameter set for this analysis also.

A non-relativistic set was used which was compiled by Daehnick, Childs and Vrcelj[18], and is intended for the bombarding energy range of 12-90 MeV.

The parameters are defined as follows:

$V_R = 88.5 - 0.26E + 0.88ZA^{1/3}$ MeV

$r_R = 1.17$ fm

$a_R = 0.709 + 0.0017E$ fm

$W = (12.2 + 0.026E)(1 - e^{\beta})$ MeV

where $\beta = -(E/100)^2$

$W_D = (12.2 + 0.026E)\, e^{\beta}$ MeV

$r_w = r_D = 1.325$ fm

$a_w = a_D = 0.53 + 0.07A^{1/3} - 0.04 \sum_i \exp(-\mu_i)$

where $\mu_i = [(M_i - N)/2]^2$ and the M_i are the magic numbers 8, 20, 28, 50, 82, and 126, and N is the neutron number.

$r_c = 1.30$ fm

$V_{so} = 7.33 - 0.029E$ MeV

$r_{so} = 1.07$ fm

$a_{so} = 0.66$ fm

The parameter values for the deuterons produced in the ground state transition, for which E=15.4 MeV are given in the table (4.1).

	V_o (MeV)	r_{oR} fm	a_R fm	W_o MeV	r_{oI} fm	a_I fm	W_D MeV	r_{oD} fm	a_D fm	V_{so} MeV	r_{so} fm	a_{so} fm	r_c fm
n (a)	46.7	1.17	0.75	3.19	1.26	0.58	6.2	1.26	0.58	6.2	1.01	0.75	1.3
d (b)	92.1	1.17	0.74	2.97	1.33	0.80	12.3	1.33	0.80	6.9	1.07	0.66	1.3
p (a)	(c)	1.17	0.75							6.2	1.01	0.75	1.3

(a) Ref.(14) Becchetti and Greenlees.

(b) Ref.(18) Daehnick et al.

(c) Potential depth adjusted to give correct binding energy ($|B_n| = |B_n\ (g.s.)| + E_{Ex}$).

Table 4.1 The optical model potential and bound state parameters.

The optical potential for the proton that is bound to the ^{89}Y nucleus, consists of a real Woods-Saxon well and a real spin-orbit potential. The real well depth is pre-set at some convenient value and then a search is performed by the program on the well-depth for the fixed binding energy. This binding energy is adjusted for each excited state, so that

$$|B_n| = |B_n(g.s.)| + E_x$$

where $B_n(g.s.)$ is the binding energy of the proton in the ground state of ^{89}Y while E_x is the excited state energy of the ^{89}Y nucleus. The rest of the parameters are obtained from reference (14) and are reflected in table (4.1).

Level(keV)		Jπ
0.0		1/2-
909.2	1	9/2+
1507.4	5	3/2-
1744.5	2	5/2-
2222	2	5/2+
2530.0	2	7/2+
2566.5	2	(11/2)+
2622.1	8	9/2+
2873	4	(5/2,7/2)+
2884	6	3/2-
2893		
3069	4	3/2-
3107	5	(3/2,5/2)-
3139	5	(3/2,5/2)-
3247	5	
3413	5	
3452?	5	
3501		
3512	6	3/2-
3558	5	(1/2)-
3612	4	
3626	6	(9/2,11/2)+
3716	5	5/2+
3748	5	(9/2,11/2)+
3849	5	
3864	6	(3/2,5/2)-
3924		
3975		(9/2,11/2)+
3990	5	(3/2,5/2)-
4000	20	1/2+
4011		
4022	6	(3/2,5/2)-
4103	6	
4169	6	(3/2,5/2)-
4188	6	(3/2,5/2)+
4229	6	
4251		
4304		(7/2,9/2)-
4330		
4352		
4383		
4404		
4456		(7/2,9/2)-
4460	20	(1/2+)
4473		
4489		
4508		
4526		(5/2,7/2)+
4536		(3/2,5/2)-
4555		(7/2,9/2)-
4580	20	(3/2,5/2)+

Level(keV)	Jπ
4588?	
4603	(7/2,9/2)-
4636	
4654	
4682	
4737	
4770	
4785	
4817	
4831	
4849	(3/2,5/2)+
4862	
4888	
4907	
4927	
4954	
4973	
5006	
5026	
5046	
5075	1/2+
5089	
5099	
5115	(3/2)-
5125	
5148	
5170	
5183	(3/2,5/2)+
5211	
5257	
5275	1/2+
5289	
5303	
5321	
5343	1/2+
5362	
5382	
5421	
5430	(3/2,5/2)+
5455	
5476	
5506	
5542	
5562	
5582	
5592	
5622	
5631	
5647	
5668	
5694	

Level(keV)		Jπ
5725		
5739		
5753		
5774		
5793		
5801		
5820		
5843		
5853		(3/2,5/2)+
5888		
5915		
5950		
5981		
6004		
6100	20	(3/2,5/2)+
6200	20	(7/2,9/2)+
6280	20	(3/2,5/2)+
6480	20	(1/2+)
6590	20	(3/2,5/2)+
6680	20	
6780	20	
7720	20	

Fig. 4.1 Level scheme of ^{89}Y. Reproduced from ref.(25).

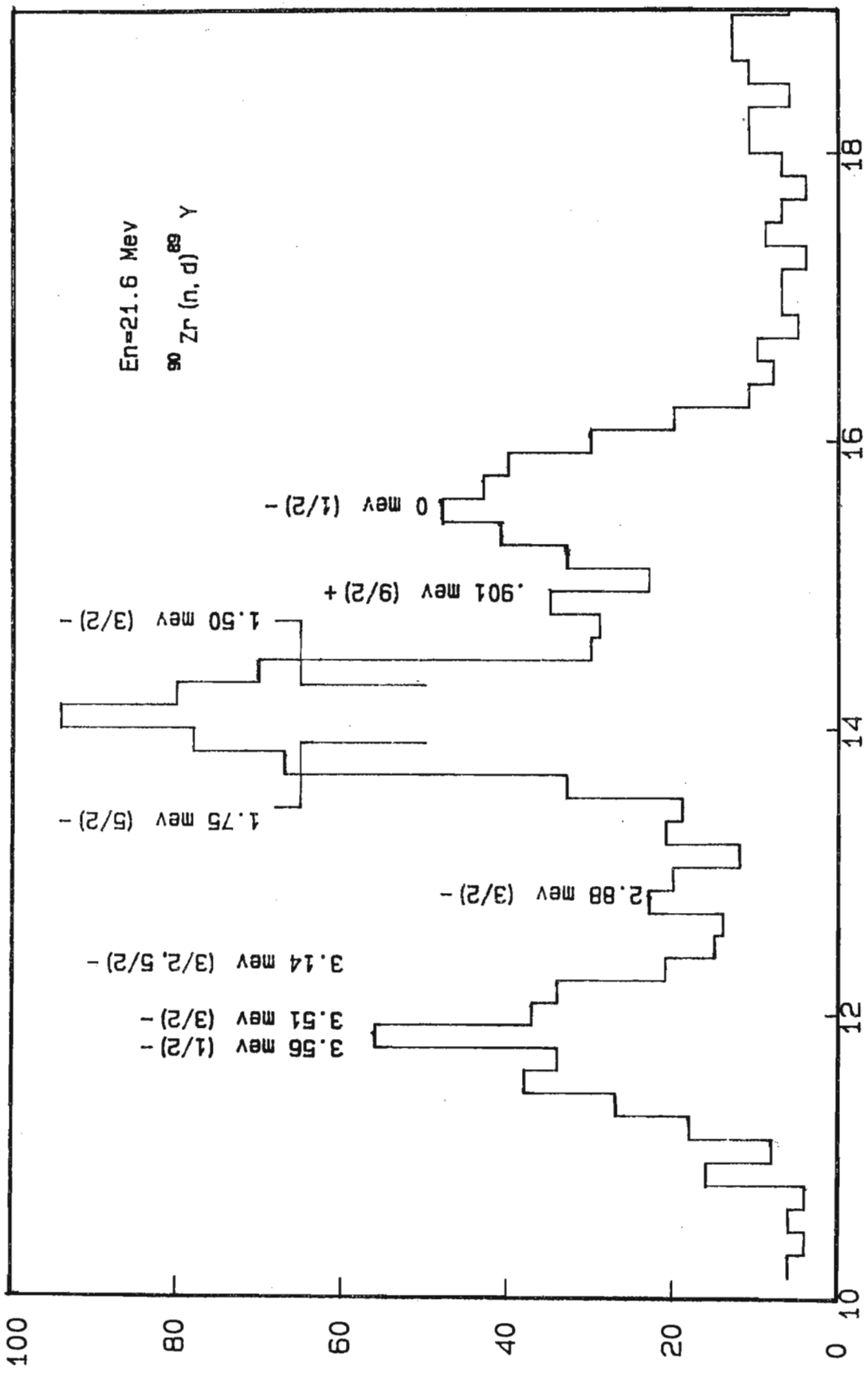

Fig. 4.2 Deuteron spectrum summed in an angle range of 60°.

4.3 The analysis

4.3.1 The target nucleus, ^{90}Zr.

The ^{90}Zr nucleus has been studied quite extensively[19] - [24]. It is a member of the group of nuclides about A=90 which may be regarded as few-nucleon systems coupled to the inert ^{88}Sr core[19][20][21]. These are the lightest nuclei in which the valence protons and neutrons fill different shell model orbitals[19]. In the shell model description, ^{90}Zr is characterized by two valence protons outside the closed $2p_{3/2}$ proton subshell, since the neutron number of ^{90}Zr is equal to the neutron number of ^{88}Sr (= 50, a magic number). The valence protons can occupy three possible configurations: $(2p_{1/2})^2$, $1g_{9/2})^2$, and $(2p_{1/2}1g_{9/2})$. The $(2p_{1/2})^2$ configuration produces the ground state with $J^\pi = 0^+$ while the $(1g_{9/2})^2$ configuration produces amongst others, the first excited state with $J^\pi = 0^+$ at an excitation energy of 1.752 MeV[25]. The N = 50 nuclei can be described by the valence protons if the filled $1g_{9/2}$ neutron orbital is a good, closed one. This does appear to be the case. The neutron occupation of the outerlying $2d_{5/2}$ shell model orbital in ^{90}Zr has been shown[26], via a neutron pick-up reaction, to be 0.0013. Occupation of this orbital in ^{88}Sr is higher at 0.1[27].

Studies of the $2p_{3/2}$ proton orbital closure indicate that this is also well established. Proton stripping on ^{88}Sr [28] shows that the occupation of the $2p_{1/2}$ proton orbital of ^{88}Sr is approximately 0.1. A further measure of the closure of this orbital and the $1g_{9/2}$ neutron orbital is indicated by the fact that ^{88}Sr has only two excited states below the excitation energy of 3 MeV. ^{90}Zr is then assumed to be described by its two valence protons.

4.3.2 The residual nucleus, ^{89}Y

This nucleus is similarly described by its single valence proton linked to the closed, inert core of ^{88}Sr. The level scheme of ^{89}Y is given in figure (4.1)[25]. It has a ground state spin of $(1/2)^-$ from the $(2p_{1/2})$ configuration, a first excited state at 0.909 MeV with spin $(9/2)^-$ from the $(1g_{9/2})$ configuration, a second excited state at 1.51 MeV with spin $(3/2)^-$ from the $(1p_{3/2})^{-1}$ configuration, etc.

4.3.3 The experimental data

Figure (4.2) shows a summed deuteron spectrum (summed over 60°). The channel number-energy calibration follows the study in chapter 3. The figure indicates the state of the residual nucleus (^{89}Y) opposite each of the deuteron peaks. A study of this reaction spectrum indicates deuteron peaks corresponding to deuteron energies of 15.5 MeV and 14.0 MeV with several smaller peaks in evidence. Kinematic calculations and a comparison with the accepted level structure of ^{89}Y[25] leads to the identification of the transitions that correspond to each of these peaks. Unfortunately, the energy resolution of $\approx$ 0.6 MeV of the experimental data is not high enough to resolve all the peaks into a one-to-one correspondence with the transitions of ^{90}Zr to the excited states of ^{89}Y. One such peak is that identified as the "1.6 MeV" peak and an adhoc fashion analysis of this peak is performed in this study.

4.3.4 The ground state transition

Kinematic calculations indicate that the deuterons produced in the transition from the ground state of ^{90}Zr to the ground state of ^{89}Y should have a laboratory energy of 15.5 MeV.

It is clear then that the first peak in the deuteron spectrum in figure (4.2) corresponds to this transition. The ground state of ^{90}Zr has $J^{\pi} = 0^{+}$ while the ground state of ^{89}Y has $J^{\pi} = 1/2^{-}$. Then, j (= total angular momentum transferred) has a value of 1/2 and there is a change in parity. The change in parity implies that ℓ (= the orbital angular momentum transferred) must be odd[4][5]. This identifies the orbital angular momentum of the proton (bound to the ^{89}Y nucleus) as $\ell_p = 1$ and its total angular momentum as $j_p = 1/2$. This ensures that the proton picked-up in the ground state transition is from the $2p_{1/2}$ shell model orbital in ^{90}Zr. Gloeckner[19] calculates the proton occupancy of this orbital as 1.33 and earlier experimental values for this occupancy are given in table (4.2).

4.3.5 The transition to the first excited state

In the summed deuteron spectrum in figure (4.2), a small but definite peak occurs at ≈ 14.6 MeV. This peak is not apparent in the spectra for individual angles (see figure 3.24) because of poor statistics. This peak corresponds to a transition from the ground state of ^{90}Zr to the first excited state of ^{89}Y at 0.909 MeV. This transition involves a j-value of 9/2 and no change in parity, which produces an ℓ-value of 4. It is clear then that this deuteron peak corresponds to a pick-up of a proton with $\ell_p = 4$ and $j_p = 9/2$; that is, a proton in the $1g_{9/2}$ proton orbital. As has already been indicated, poor statistics did not permit an analysis of this peak except as a contribution to the ground state transition.

The number of protons shared by the $2p_{1/2}$ and the $1g_{9/2}$ proton orbitals is two and so the theoretical proton occupancy of the $1g_{9/2}$ orbital is 0.67, following Gloeckner[19]. The experimental values for this occupancy obtained in previous experiments are given in table (4.2).

The deuteron peak at approximately 14 MeV is broad and unresolved. Kinematic calculations, together with the level scheme of ^{89}Y, indicate that at least three deuteron peaks may be submerged in this "1.6 MeV" peak.

4.3.6 The transition to the second excited state

The second excited state of the ^{89}Y nucleus has an excitation energy of 1.51 MeV and a transition to this state will result in a deuteron peak at ≈ 14.0 MeV. Such a transition (from $J^\pi = 0^+$ to $J^\pi = 3/2^-$) corresponds to a j-value of 3/2 and a change in parity, which implies an ℓ-value of 1. It is clear then that this transition results from the pick-up of a proton with $\ell_p = 1$ and $j_p = 3/2$, which identifies the pick-up as being from the $2p_{3/2}$ proton orbital. This orbital is filled with $2j_p + 1 = 4$ protons which are available for this transition.

4.3.7 The transition to the third excited state

The second deuteron peak submerged in the "1.6 MeV" peak originates in the transition from the ground state of ^{90}Zr to the third excited state of ^{89}Y at 1.75 MeV which has $J^\pi = 5/2^-$. This deuteron peak then, corresponds to a j-value of 5/2 and an ℓ-value of 3 and so the transition corresponds to a proton pick-up from the $1f_{5/2}$ proton orbital. The occupancy of this orbital is 6.

4.3.8 The transition to the fourth excited state

The fourth excited state of ^{89}Y has an excitation energy of 2.22 MeV. Kinematic calculations show that deuterons produced in a transition to this state (if it were possible) would have an energy of $\approx$ 13.6 MeV which would make it lie within the "1.6 MeV" peak. This is a $5/2^+$ state and the excitation of this state would require the pick-up of a proton from a j = 5/2 shell model orbital with an ℓ = 2 orbital angular momentum since there is no change in parity. This effectively forbids the excitation of this state in the (n,d) reaction since the proton occupancy of the $2d_{5/2}$ shell is zero in ^{90}Zr.

4.4 The distorted-wave method analysis

The distorted-wave method calculations were performed with the optical potentials and optical potential parameters described in section (4.2) above. The finite-range corrections (for the zero-range approximation) and the nonlocal potential corrections are performed in the LEA. The finite range correction parameter was set in the middle of the field prescribed by Kunz[1], at 0.667 while the nonlocal correction parameters were set at β = 0.85 for the nucleons and β = 0.54 for the deuterons[1]. The comparisons between the theoretical and experimental cross sections were carried out via the relationship[7]

$$\sigma(\theta)_{EXP} = 3/2\ D_o^2\ (C^2S)\ \sigma(\theta)_{DW}$$

The value of the overlap integral D_o^2 was estimated by Bassel[6] to be 1.55 from calculations which included the effect of the deuteron d-state admixture in the deuteron wavefunction. The quantity C^2S where

$$C = \langle T_f\ T_{fz}\ \tfrac{1}{2}\ t_z \mid T_i\ T_{iz} \rangle$$

is the isospin Clebsch-Gordan coefficient with T_i and T_f being the isospins of the initial and final nuclei, is then the spectroscopic factor of a particular transition ($i \rightarrow f$).

Chi-squared fits to the experimental cross sections were obtained by minimizing the expression

$$\chi^2 = \sum_{i=1}^{n} [(C^2S)\sigma(\theta_i)_{EXP} - \sigma(\theta_i)_{DW}]^2/[\delta(\sigma(\theta_i))]^2$$

where N is the number of experimental points while $\delta(\sigma(\theta_i))$ is the error (or inverse of weight) associated with $\sigma(\theta_i)_{EXP}$. The $\sigma(\theta_i)_{DW}$ were folded into the modified angular scale because of the solid angle corrections that were necessary for the existing geometry in the experimental set-up.

The angular distribution of the ground state deuteron cross section is shown in figure (4.3), together with distorted-wave method fits. The broken-line fit represents a calculation based on the assumption that the deuteron cross section is due to a pure $2p_{1/2}$ proton pick-up and the comparison described above produces a spectroscopic factor of 1.8 ± 0.4. However, the energy resolution of the spectrometer is in the region of 0.6 MeV (FWHM) and it is likely that the "ground state" peak contains some contribution from the proton pick-up from the $1g_{9/2}$ shell model orbital. (See figure (4.2)). A small contribution from this proton pick-up cross section, of the order of 0.1 protons, improves the fit to the experimental points significantly and decreases the spectroscopic factor to 1.7 ± 0.4. This compared favourably with the calculated value of 1.33[19]. This second fit is represented by the solid line curve in figure (4.3).

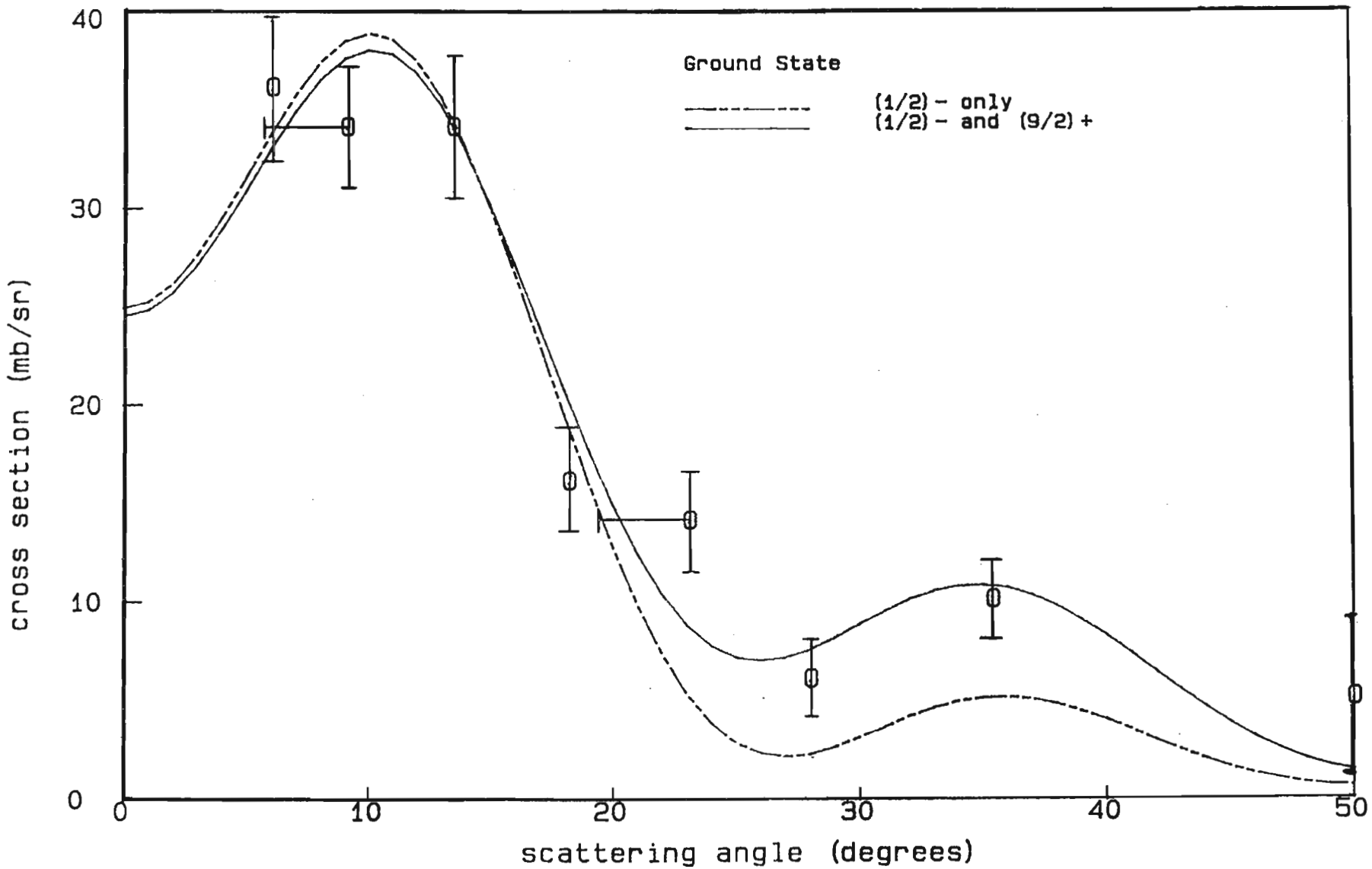

Fig. 4.3 Angular distribution of the cross-section of the ground state transition in the $^{90}Zr(n,d)^{89}Y$ reaction.

As we have seen, two deuteron peaks are submerged in the "1.6 MeV" peak, as the fourth excited state of ^{89}Y is unlikely to be excited in this reaction. The two peaks are those due to the pick-up of:

(a) the $2p_{3/2}$ shell model orbital protons and

(b) the $1f_{5/2}$ shell model orbital protons.

These transitions produce deuteron peaks that are associated with the second and third excited states of ^{89}Y which have excitation energies of 1.51 and 1.75 MeV, respectively. These peaks occur with approximately equal separation on either side of 1.6 MeV (where the combined peak appears to be peaked). The insufficient energy resolution forces a combined treatment of these two peaks. This was done by manually choosing different spectroscopic factors for each of the transfers and then obtaining the best fit for the angular distribution of the deuteron cross sections for this "1.6 MeV", using a modified version of the Chi-squared equation described above. The best fit produces the following spectroscopic factors for the pair of transitions:

$j = 3/2, \quad \ell = 1, \quad C^2S = 1.8 \pm 0.4$

$j = 5/2, \quad \ell = 3, \quad C^2S = 0.7 \pm 0.4.$

Whilst this process must appear quite arbitrary it must be said that the distorted-wave fits are sensitive to the choice of spectroscopic factors. The reason for this lies in the fact that the distorted-wave cross sections for the $j = 3/2$ transition (which is an $\ell=1$ transition) peaks at approximately 10° while the $j = 5/2$ transition (which is an $\ell=3$ transition) peaks at approximately 25°.

This ensures that the distorted-wave method fits, which are independently sensitive to the choice of spectroscopic factors, are also sensitive in combination since the one dominates the region about 10° while the other dominates the region about 25°. Figure (4.4) shows a distorted-wave method fit to the experimental points of this "1.6 MeV" peak.

Table (4.2) provides a comparison of the spectroscopic factors for the transitions investigated in the present study with those of earlier experiments[22][23] and those that are derived from shell model limits. Preedom's values[22] are consistly high. The ground state spectroscopic factor obtained in this study agrees within error with the prediction of Gloeckner[19] and with the values obtained from earlier experiments.

Excitation Energy (MeV)	Present Work	Ref.(4)	Ref.(10)	Model Limits
0.0	1.7(5)	1.91	1.4	1.33
0.91		1.10	0.6	0.67
1.51	1.8(5)	4.25		4.0
1.75	0.7(4)	7.80		6.0

Table 4.2 Comparison of spectroscopic factors.

For the 1.51 and 1.75 MeV states, the values obtained in this study are very much lower than the model limits. These model limits are derived from the proton occupancy of the $2p_{3/2}$ and $1f_{5/2}$ shell model orbitals. If it may be assumed that the only states with $J^{\pi} = 3/2^-$ and $5/2^-$ excited in this reaction are the states at 1.51 and 1.75 MeV respectively then it will be true that the spectroscopic factors for these transitions will be

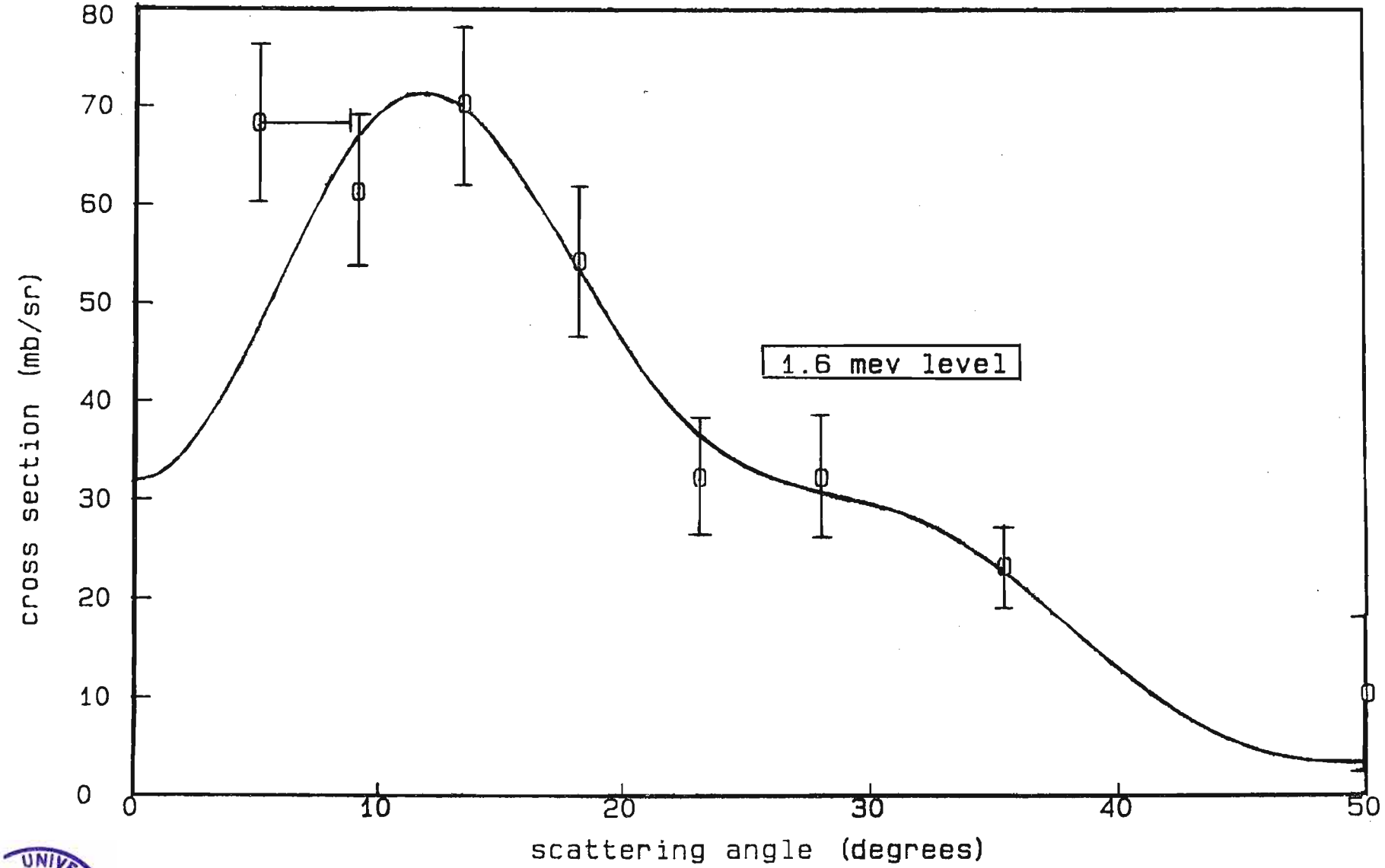

Fig. 4.4 Angular distribution of the cross-section of the transition to the 2nd and 3rd excited states of ^{89}Y in the $^{90}Zr(n,d)^{89}Y$ reaction.

the model limits. However, it is clear from a survey of the level structure[29] of ^{89}Y that there are at least thirteen states of ^{89}Y with $J^{\pi} = 3/2^-$ (below an excitation energy of 5 Mev) and at least eight excited states with $J^{\pi} = 5/2^-$ (below an excitation energy of 4.5 MeV). It is true that direct reactions tend to favour lower excitation energy final states, but the energies considered here are relatively small. Further, a study of the summed deuteron spectrum in figure (4.2) indicates that some of these levels are indeed excited in this (n,d) reaction. The statistics are unfortunately much too poor to permit a distorted-wave method analysis of these deuteron peaks. What is evident therefore, is that the transition strengths to these states at 1.51 MeV and 1.75 MeV do not exhaust the sum rule limits for proton transfers from the $2p_{3/2}$ and $1f_{5/2}$ shell model orbitals.

An attempt to calculate the relative spectroscopic factors to each of the $J^{\pi} = 3/2^-$ excited states of ^{89}Y was attempted. Use was made of the theory of deShalit and Talmi[30] for the coefficients of fractional parentage and the expression of Glaudemans[31] for the spectroscopic factor ($S = n \times c.f.p.^2$ where c.f.p. is the coefficient of fractional parentage and n is the nucleon occupation number of the orbital under consideration). Proton seniority considerations in the calculations tended to show that the theory used above cannot predict the excitation of $3/2^-$ states beyond that at 1.51 MeV.

REFERENCES.

(1) P. D. Kunz, unpublished.

(2) R. M. deVries, unpublished.

(3) N. Austern, Direct nuclear reaction theories (Wiley-Interscience, New York 1970).

(4) G. R. Satchler, Direct Nuclear Reactions (Oxford Science Publications, Oxford 1983).

(5) N. K. Glendenning, Direct Nuclear Reactions (Academic Press, Inc., New York 1983).

(6) R. H. Bassel, Phys. Rev. 149 (1966) 1.

(7) P. G. Roos et al, Nucl. Phys. A255 (1975) 187.

(8) P. B. Foot et al, Phys. Rev. C31 (1985) 1133.

(9) W. N. Wang and E. J. Winhold, Phys. Rev. 140 (1965) B882.

(10) C. B. Fulmer and J. B. Ball, Phys. Rev. 140 (1965) B330.

(11) B. M. Preedom and E. Newman, Phys. Rev. 166 (1968) 1156.

(12) M. P. Fricke et al, Phys. Rev. 156 (1967) 1207.

(13) J. B. Ball, C. B. Fulmer and R. H. Bassel, Phys. Rev. 135 (1964) B706.

(14) F. D. Becchetti and G. W. Greenlees, Phys. Rev. 182 (1969) 1190.

(15) D. Wilmore and P. E. Hodgeson, Nucl. Phys. 55 (1964) 673.

(16) L. Rosen et al, Ann. Phys. NY 34 (1965) 96.

(17) J. Rapaport et al, Nucl. Phys. A313 (1979) 1.

(18) W. W. Daehnick, J. D. Childs and Z. Vrcelj, Phys. Rev. C21 (1980) 2253.

(19) D. H. Gloeckner, Nucl. Phys. A253 (1975) 301.

(20) I. Talmi and I. Unna, Nucl. Phys. 19 (1960) 225.

(21) N. Auerbach and I. Talmi, Nucl. Phys. 64 (1965) 458.

(22) J. Vervier, Nucl. Phys. 75 (1966) 17.

(23) C. B. Fulmer and J. B. Ball, Phys. Rev. 172 (1968) 1199.

(24) M. R. Cates, J. B. Ball and E. Newman, Phys. Rev. 187 (1969) 1682.

(25) Nuclear Data Sheets 16 (1975) 445.

(26) R. W. Bercour and R. E. Warner, Phys. Rev. C2 (1970) 297.

(27) J. Picard and G. Bassani, Nucl. Phys. A131 (1969) 636.

(28) P. J. Brussard and P.W.M. Glaudemans, Shell-model applications in nuclear spectroscopy (North-Holland, Amsterdam 1977).

(29) A. deShalit and I. Talmi, Nuclear shell theory Academic Press, New York 1963).

Chapter Five

Discussion

5.1 Introduction

The major tasks of this study may be divided into four distinct topics, which are described below. They have all been covered with some success. In this discussion, it is hoped first of all to summarize some of the results of the analysis performed and then to suggest how the analysis may be improved to present greater efficiency in the spectroscopic nature of the study.

The aims of the study may be described as follows:

(a) To understand the distorted-wave method and its application to single-nucleon transfer reactions. This required the understanding of the Optical Model and its potentials (including the method for choosing the parameters). In addition, ambiguities that surround the use of the distorted -wave method were investigated.

(b) To undertake a survey and to use the charged-particle spectrometer developed by W. R. McMurray and K. Bharuth-Ram[1][2], which was employed to amass data in the reaction studied in this research. An important aspect of this part of the study was to determine whether the efficiency and energy and angular resolution of the spectrometer allowed for a distorted-wave method analysis of the data.

(c) To perform a distorted-wave method analysis of the data obtained from the bombardment of a ^{90}Zr enriched foil with 21.6 MeV neutrons and then observing the resulting deuteron (and proton) spectra at various angles. The distorted-wave method analysis, which required the use of a high-speed mainframe computer is described in Chapter Four. A comparison between the calculated and experimentally obtained angular distributions of the cross-sections indicate that the dominant process in this interaction is the direct pick-up reaction.

(d) To understand the use of single-nucleon particle transfer reactions in spectroscopic studies. It is possible, from comparing the calculated and experimentally obtained angular distributions of the cross-sections, to extract information on the nuclear structure of the participating nuclei. The derived cross-section in the distorted-wave method is related to the distorted-wave scattering cross-section by the following relationship

$$\sigma_1(\theta) \propto S\ \sigma_\ell^{DW}(\theta)$$

where ℓ=orbital angular momentum transferred and $\sigma_\ell^{DW}(\theta)$ depends only on the reaction parameters such as the energies and scattering angles. S, the spectroscopic factor is a function of the nuclear structure of the target and residual nuclei. By determining the spectroscopic factor, very concrete information on nuclear structure has been obtained.

5.2 A summary of the application of the distorted-wave method to the reaction

The distorted-wave method has been resorted to in this analysis because the simpler plane-wave theory formulated by Butler[3], which is referred to very briefly in Chapter Two, produced cross-sections which were at least an order of magnitude greater than those experimentally observed[4]. However this theory did permit the determination of the orbital angular momentum transferred in these reactions. In the case of zero-spin target nuclei (such as ^{90}Zr is), it is then possible to assign ℓ values to the different excited states of the residual nucleus. The determination of spectroscopic factors depends heavily on obtaining the correct magnitude in the calculated cross-sections and so the distorted-wave method is employed which has greatly improved this aspect of the calculation.

The next step was to examine the intensities of the different deuteron groups in the spectrum (see figure (4.2)). This technique is profitable because the (n,d) reaction (as is true for all direct reactions) is highly selective in the final states that it populates. This selectivity is demonstrated by the one-to-one correspondence which exists between the energies of the deuteron groups and the excitation energies of the residual nucleus (which result from the pick-up of very specific ℓj-protons from the target nuclei). If in the comparison between the experimental and calculated cross-sections a spectroscopic factor of one is obtained then this implies that one proton was available for pick-up to lead to a specific final state. (See McFarlane and French[5].) Following this general approach, an analysis of the available data on the $^{90}Zr(n,d)^{89}Y$ reaction was carried out and was partially successful.

5.3 Problems with the analysis

5.3.1 Insufficient statistics in the data

The analysis allowed the extraction of details on the proton occupancy of the $2p_{1/2}$ proton subshell in ^{90}Zr, as shown in Chapter Four. However, an anlysis of the transition from the ground state of ^{90}Zr to the first excited state of ^{89}Y (which is $1g_{9/2}$ state) was impossible. The reason for this was the relatively insufficient statistics achieved for the transition, though the summed spectrum (figure (4.2)) shows a small but definite peak at $\approx$ 0.92 MeV excitation energy of ^{89}Y which is very nearly the exact position of the first excited state of ^{89}Y (.909 MeV). By performing this analysis it would have been possible to obtain a value for the proton occupancy of the $1g_{9/2}$ level, and together with the proton occupancy of the $2p_{1/2}$ level, a very indicative measure of the efficiency of the measuring system and analysis would have been available, since their sum has to be two.

The lack of statistics resulted in a second major problem in the analysis. The model limit for the transition from the ground state of ^{90}Zr to excited states of ^{89}Y with $J^{\pi} = 3/2^-$ is four; since the proton occupancy of the $2p_{3/2}$ proton subshell is four. The spectroscopic factor obtained in this study for the transition to the second excited state, which is a $3/2^-$ states at 1.51 MeV, is 1.7 ± 0.4. There is evidence in the summed deuteron spectrum that several other $3/2^-$ state were excited in this reaction but poor statistics denied an analysis of these peaks.

It must be noted that this spectroscopic factor of 1.7 for the transition to the second excited state is reasonable on two grounds:

(a) there are at least ten $3/2^-$ states in ^{89}Y below an excitation energy of 5 MeV.

(b) The $2p_{3/2}$ proton subshell is a closed one (since ^{88}Sr is a closed, inert core) and the probability of removing a proton from it must be less than one.

The statistics of the data may be improved in several ways:

(a) Increasing the run-time of the experiment is a possibility, though the run-times for the previous runs are already long, making the cost factor an important one.

(b) Doubling the thickness of the target foil will double the count rate and thus help to improve the statistics. It is possible that the energy resolution of the data may be affected but this will have to be investigated. As for the angular resolution, the thinness of the foil will permit the doubled foil to continue to be considered as a two-dimensional target and should therefore leave the angular resolution unaffected.

(c) Decreasing the value of d (= the distance between the tritium cell and the target) from 120 mm to 60 mm has the effect, as was seen in Chapter Three, of shifting the mean scattering angle further away from the nominal angle and of adversely changing the angular resolution. However, the loss in resolution is greatly outweighed by the gain in neutron flux on the target which is quadrupled if d is halved. This gain in statistics will help the analysis tremendously.

It will be shown later that the loss in resolution may not affect the analysis adversely.

5.3.2 The energy resolution of the deuteron spectrum

In reference (1), the authors state that the spectrometer has an energy resolution of approximately 0.8 MeV. In the run of the present experiment, it became evident that this value is really closer to 0.6 MeV. Even this value has an adverse affect on the efficiency of a distorted-wave method analysis. A typical instance of this was in the analysis of the "1.6 MeV" peak, which is an unresolved peak. As was mentioned in Chapter Four however, the spectroscopic factors obtained in that analysis were obtained with a method which was highly sensitive to the choice of spectroscopic factors. This lack of resolution produced problems with the analysis of the ground state peak as well, as it became necessary to consider some contribution of the 1st excited state peak to the ground state peak. This, as can be seen in Chapter Four, improves the fit of the calculated cross-section to the experimental cross-section.

A reasonable analysis of the data has been possible in the study of this particular reaction but that is only so because of the sufficient energy spacing between the excited states of the ^{89}Y nucleus. For instance, preliminary investigations show that an analysis of the $^{27}A\ell(n,d)^{26}Mg$ reaction may be much more complicated because of the decreased level-spacing between the excited states in the ^{26}Mg nucleus. The use of the spectrometer may therefore be limited unless its energy resolution can be improved.

As a comparison, the study of a similar reaction by Ball and Fulmer[6], in which they used a magnetic spectrograph, had an energy resolution of approximately 18 keV. They were able to accumulate accurate information on the nuclear structure of ^{90}Zr.

5.3.3 The angular resolution of the spectrometer

The angular resolution of the spectrometer depends largely on the geometry of the experimental set-up. As was seen in Chapter Three, it differs from $\pm 4.4°$ to $\pm 3.7°$ for the cases of d=60 mm and d=120 mm respectively. This change in angular resolution does not affect the distorted-wave method analysis to any great extent since the fitting of the calculated angular distribution of the cross-section to the experimentally obtained one is determined primarily by fitting the respective forward angle peaks. The calculated peaks in the forward direction for ℓ-transfers of 0,1,2, ... occur at progressively larger angles which make the peaks easily distinguishable. (see figure (5.1)).

Additional calculations have been performed to determine the effect of the choice of different angle limits (for example, $\pm 1°$, $\pm 2.5°$, and $\pm 5°$) on angular resolution. These calculations tend to show that the angular resolution is not grossly affected by this. Statistics requirements tend to force wider angle limits but the need for as many data points as possible (for the analysis) force smaller angle limits. An angle range of $\pm$ 2.5° seems a suitable compromise.

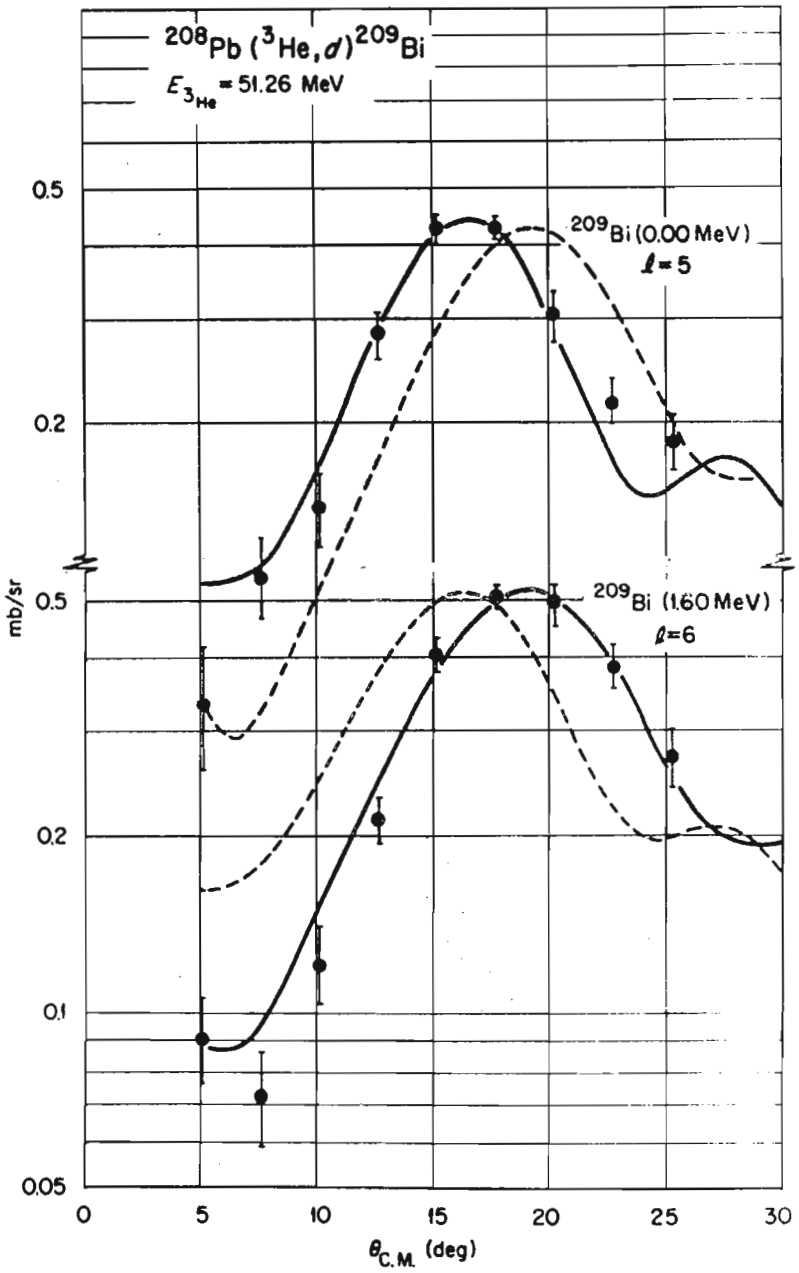

Fig. 5.1 Peak positions for ℓ = 5 and ℓ = 6 transition DW calculations. Reproduced from Wildenthal et al, Phys. Rev. Lett. 19 (1967) 965.

5.3.4 Improvements in the distorted-wave method calculations

To be able to obtain accurate information on nuclear structure using the distorted-wave method, and assuming that the angular and energy resolutions and statistics are improved, the following improvements may be necessary in the calculations.

(a) The adiabatic approximation of Johnson and Soper[7][8][9] must be employed. This technique deals with the (n,d) reaction as a three-body problem. The approximation is made in the optical potential of the deuteron. The technique has been applied successfully in several studies [10][11].

(b) The lack of elastic scattering data on ^{90}Zr and deuteron elastic scattering data on ^{89}Y resulted in the use of global optical potential parameters (which were fairly successful - see Chapter Four). However, to complete the analysis efficiently it would be necessary to perform these elastic scattering reactions to obtain authentic optical model potential parameters for the analysis.

(c) Even though the zero-range approximation produces good results for the single-nucleon transfer reactions, it is necessary to perform the calculations using one of the codes which deal exactly with finite-range effects. such as LOLA[12] or to resort to the theory of Charlton[13].

REFERENCES:

(1) W. R. McMurray and K. Bharuth-Ram, S.Afr. J. Phys. 8 (1985) 22.

(2) W. R. McMurray et al, SUNI Annual Research Report 55 (1978) 14.

(3) S. T. Butler and O. H. Hittmair, Nuclear stripping reactions (John Wiley and Sons Inc., New York 1959).

(4) L. L. Lee et al, Phys. Rev. 136 (1964) B971.

(5) M. H. Macfarlane and J. B. French, Rev. Mod. Phys. 32 (1960) 567.

(6) J. B. Ball and C. B. Fulmer, Phys. Rev. 172 (1968) 1199.

(7) R. C. Johnson and P. J. R. Soper, Phys. Rev. C1 (1970) 976.

(8) R. C. Johnson and P. C. Tandy, Nucl. Phys. A235 (1974) 56.

(9) G. L. Wales and R. C. Johnson, Nucl. Phys. A275 (1976) 168.

(10) P. B. Foot et al, Phys. Rev. C31 (1985) 1133.

(11) P. G. Roos et al, Nucl. Phys. A255 (1975) 187.

(12) R. M. deVries, unpublished.

(13) L. A. Charlton, Phys. Rev. C8 (1973) 146.